

REPORT DOCUMENTATION PAGE

Form Approved

OMB No. 0704-0188

AD-A253 907



tion is estimated to average 1 hour per response, including the time for reviewing instructions, searching existing data sources, completing and reviewing the collection of information. Send comments regarding this burden estimate or any other aspect of this reducing this burden to Washington Headquarters Services, Directorate for Information Operations and Reports, 1215 Jefferson 2 and to the Office of Management and Budget, Paperwork Reduction Project (0704-0188), Washington, DC 20503

2. REPORT DATE
June 19923. REPORT TYPE AND DATES COVERED
Reprint

5. FUNDING NUMBERS

2

RLE Progress Report No. 134

DAAL03-92-C-0001

6. AUTHOR(S)

Prof. J. Allen and RLE Principal Investigators

7. PERFORMING ORGANIZATION NAME(S) AND ADDRESS(ES)

Research Laboratory of Electronics
Massachusetts Institute of Technology
77 Massachusetts Avenue
Cambridge, MA 02139

8. PERFORMING ORGANIZATION
REPORT NUMBER

9. SPONSORING/MONITORING AGENCY NAME(S) AND ADDRESS(ES)

U. S. Army Research Office
P. O. Box 12211
Research Triangle Park, NC 27709-2211

10. SPONSORING/MONITORING
AGENCY REPORT NUMBER

ARO 28925.13-EL

11. SUPPLEMENTARY NOTES

The view, opinions and/or findings contained in this report are those of the author(s) and should not be construed as an official Department of the Army position, policy, or decision, unless so designated by other documentation.

12a. DISTRIBUTION/AVAILABILITY STATEMENT

Approved for public release; distribution unlimited.

12b. DISTRIBUTION CODE

13. ABSTRACT (Maximum 200 words)

Reprint Pages 7-9, 12, 14-15, 19-41, 55-68, 71-74, 76, 81-82, 85-97,
125-146, 167-176, 214-217

DTIC
ELECTE
AUG 04 1992
S A D

92-21033

92 8 105

14. SUBJECT TERMS

15. NUMBER OF PAGES

16. PRICE CODE

17. SECURITY CLASSIFICATION
OF REPORT

UNCLASSIFIED

18. SECURITY CLASSIFICATION
OF THIS PAGE

UNCLASSIFIED

19. SECURITY CLASSIFICATION
OF ABSTRACT

UNCLASSIFIED

20. LIMITATION OF ABSTRACT

UL

RLE Progress Report

No. 134

January 1 - December 31, 1991

Submitted by

**Professor Jonathan Allen
Professor Daniel Kleppner**

DTIC QUALITY INSPECTED 5



Accession For	
NTIS CRA&I	<input checked="checked" type="checkbox"/>
DTIC TAB	<input type="checkbox"/>
Unannounced	<input type="checkbox"/>
Justification	
By	
Distribution/	
Availability	
Dist	Avail and/or Special
A-1	20

**Research Laboratory of Electronics
Massachusetts Institute of Technology
Cambridge, Massachusetts**

Chapter 1. Heterostructures for High Performance Devices

Academic and Research Staff

Professor Clifton G. Fonstad, Jr.

Visiting Scientists and Research Affiliates

Anton Failla,¹ Sheila Prasad,² Jae-Jin Lee,³ Jong Tae Park⁴

Graduate Students

Rajni J. Aggarwal, Thomas P.E. Broekaert, Geoffrey F. Burns, Woo-Young Choi, Isako Hoshino, Paul S. Martin, Lung-Han Peng, Yakov Royter, Krishna V. Shenoy, Richard A. Singer, Jurgen H. Smet, James C. Vleck

Technical and Support Staff

Kelley S. Donovan, Angela R. Odoardi, Richard R. Perilli

1.1 Introduction

The broad objective of our research effort is to develop III-V quantum heterostructures for high performance electronic, optoelectronic, and photonic devices for applications in high speed optical communications and signal processing. To this end, we are developing: (1) new, higher performance materials systems including InP-based InGaAlAs heterostructures and <111> oriented strained layer superlattices; (2) novel approaches to integrate laser diodes on VLSI-level electronic integrated circuits; (3) a new family of quantum-well-base, tunnel-barrier n-n-n transistors and near- and far-infrared optoelectronic devices; and (4) new damage-free in situ processing techniques for fabricating advanced quantum structure and embedded heterostructures.

The following sections describe our progress during the past year in the above research areas. Our group works closely with Professors Hermann A. Haus, James G. Fujimoto, and Erich P. Ippen to develop the optical device application, characterization, and modeling aspects of this program, and with Professor Sylvia T. Ceyer to develop new in situ processing techniques.

1.2 Computer Controlled Growth of Lattice-Matched InGaAlAs Heterostructures on InP

Sponsors

Charles S. Draper Laboratories
Contract DL-H-418483

DARPA/NCIPT

Joint Services Electronics Program
Contract DAAL03-89-C-0001
Contract DAAL03-92-C-0001

Project Staff

James C. Vleck, Professor Clifton G. Fonstad, Jr.

In electronic and optical semiconductor devices, the need for both graded-composition and hyper-abrupt metallurgical junctions frequently arises. The use of graded-composition junctions allows for precise control of the confinement of charge carriers and optical fields through spatially varying bandgaps and refractive indices, respectively. On the other hand, hyper-abrupt junctions may be

¹ Centro Studi e Laboratori Telecomunicazioni, Torino, Italy.

² Northeastern University, Boston, Massachusetts.

³ Electronics and Telecommunications Research Institute (ETRI), Daejeon, Korea.

⁴ Incheon University of Korea, Incheon, Korea.

desired in some devices, most notably quantum effect devices, where a sharp interface is desired to reduce fluctuations in the confinement energy which might arise from graded interfaces due to shutter transients.

In this work, we have grown the quaternary $\text{In}_x\text{Ga}_y\text{Al}_{1-y}\text{As}_{1-x}$, lattice-matched to InP substrates. The need to lattice-match, such as to an InP substrate, further constrains the ratio of constituent fluxes.

We have implemented a computer-automated MBE control system whose aim is to provide precise control of the constituent and dopant fluxes such as is necessary to achieve graded-composition lattice-matched alloys and maintain uniform lattice-matched compositions in the presence of shutter events. Key to this system are accurate models of the characteristics of the effusion cells, including not only the static flux versus temperature relationship, but also the time-dependent behavior of the cell in the presence of changes in either setpoint and/or shutter status. These models approximate the temporal response of the effusion cells to a setpoint change with a single-pole system function, with the location of the pole being determined by a direct measurement of the flux profile generated by a step change in the cell setpoint temperature.

In the case of graded-composition layers, the thermal lag time of the cell requires modification of the time-dependent effusion cell setpoint temperature profile, most notably to eliminate the over- and undershoot effects at the endpoints of the graded layer which would result if the effects of cell response time were neglected. With such modifications, we have achieved linearly graded flux profiles whose deviation from the desired profile can be held within one percent.

To remove flux transients which arise from the operation of the cell shutters, we have structured the control system so that it seeks to maintain the flux in the effusion cell at a constant value, irrespective of the shutter status. In practice, this entails maintaining the setpoint temperature of the cell at a lower value with the shutter closed than with it open and performing an exponential ramp sequence upon change of shutter status. Using this technique, we have reduced cell shutter transients from as high as 30 percent to one percent or less.

1.3 Molecular Beam Epitaxy of InGaAlAs Strained-Layer Heterostructures on 111 GaAs and InP

Sponsors

DARPA/NCIPT

Joint Services Electronics Program

Contract DAAL03-89-C-0001

Contract DAAL03-92-C-0001

Project Staff

Richard A. Singer, Professor Clifton G. Fonstad, Jr.

The issues associated with the molecular beam epitaxial (MBE) deposition of $\text{In}_x(\text{Ga}_y\text{Al}_{1-y})_{1-x}\text{As}$ upon (111)B InP have been extensively explored. As a result, a reproducible growth algorithm has been developed whose execution has resulted in bulk n and p-type InGaAs and InGaAlAs of comparable crystallinity to simultaneously grown (100) oriented epilayers.

When epitaxial layers are pseudomorphically deposited upon a (111) zincblende substrate, a piezoelectric field is generated due to the ionic character of the chemical bond between the constituent elements and the lack of inversion symmetry in the (111) orientation. Recently, this strain-generated electric field has been demonstrated in a GaAs based p-i-n modulator whose absorption edge was in the vicinity of 0.9 μm .

Growth on (111) InP is especially difficult because of the volatility of the InP surface and the problems attendant to (111) surface chemistry. Not surprisingly, initial attempts to grow epitaxial layer of InGaAs on (111)B InP according to the proven methods of (100) orientations were unsuccessful. Moreover, reflection high-energy electron diffraction (RHEED) patterns, which usually provide essential in situ information about the condition of a growing surface, are unclear in this material system. As a result, the most critical step in the MBE growth process—the synchronization of the desorption of the substrate's native oxide layer with the initiation of growth—is performed "in the dark."

To address these issues, an alternative growth algorithm, called quasi-migration enhanced epitaxy, was developed and named for the unusually low intensity of As overpressure, low substrate temperature, and slow growth rate which comprise its parameter set. It was learned that an intense group III overpressure, expressed in a rapid rate of growth, is needed to stabilize the (111) growth front: a $\sqrt{19} \times \sqrt{19}$ surface reconstruction that is rich in group III atoms. This is quite different from

the case of (100) materials whose $c(2 \times 8)$ surface reconstructions are As stabilized. Another important modification was the elimination of the traditional 5: 1: 1 $\text{H}_2\text{SO}_4\text{H}_2\text{O}_2\text{-H}_2\text{O}$ etching step in the pre-growth substrate preparation procedure. As a result, the thickness of the residual oxide layer was reduced which, in turn, allowed growth to be successfully initiated without the need of a risky high temperature desorption cycle.

1.4 Monolithic Fabrication of Strain-free GaAlAs Laser Diodes on Silicon Substrates

Sponsors

DARPA/NCIPT
IBM Corporation Fellowship

Project Staff

Geoffrey F. Burns, Anton Failla, Professor Clifton G. Fonstad, Jr.

Prospects for monolithic integration of III-V electrical and optical devices with Si circuits have fueled vigorous research in direct heteroepitaxial growth of these compounds on Si substrates. Developing III-V optical sources useful for VLSI optical interconnects is one goal which has been pursued by several groups. Along these lines we have focused upon the laser diode due to its capacity for high speed modulation and efficient electrical to optical power conversion.

In this work molecular beam epitaxy of (Al,Ga)As heterostructures directly on silicon substrates has been investigated for use in fabricating semiconductor lasers for monolithic optoelectronic integration. A base laser process was developed and evaluated using homoepitaxy of (Al,Ga)As on GaAs substrates, incorporating a graded-index separate confinement heterostructure (GRINSCH) quantum well active region. Etched ridge waveguide lasers were fabricated from these layers, achieving continuous wave threshold currents of 19 mA and differential quantum efficiency of 66%. This same laser process was adopted to GaAs-on-Si growth initiation layers to produce monolithic (Al,Ga)As laser on silicon substrates. High dislocation density and residual thermal tension in the laser epitaxial layer degraded threshold currents and slightly degraded external quantum efficiency, with threshold currents as low

as 40 mA and differential efficiencies as high as 60 percent. In addition, the same problems precluded continuous wave operation for these devices.

To address residual thermal tension, a technique for monolithic epitaxial separation and reattachment was developed to produce strain-free GaAs-on-Si. Rapid thermal annealing of these layers was also investigated for alleviating defect density imposed by the heteroepitaxial growth process. Photoluminescence studies demonstrated that epitaxial separation, along with rapid thermal annealing 600°C , produced strain-free material. In addition, these layers could be annealed at temperatures up to 800°C without reintroducing thermal stress and demonstrated further material improvement as indicated by photoluminescence intensity. Epitaxial separation and annealing was also applied to (Al,Ga)As laser epitaxy layers to produce the first strain-free lasers fabricated monolithically on Si substrates, an important achievement for advancing heteroepitaxy as a viable optoelectronic integration strategy.

1.5 Integration of Vertical Cavity Surface Emitting Lasers on GaAs Integrated Circuits

Sponsors

DARPA/NCIPT
IBM Corporation Fellowship
National Science Foundation Fellowship
Vitesse Semiconductor

Project Staff

Krishna V. Shenoy, Geoffrey F. Burns, Professor Clifton G. Fonstad, Jr. in collaboration with J. Mikkelsen⁵

There exists a long history of interest in the integration of high performance optoelectronic devices, particularly lasers and detectors, on high density electronic integrated circuits, and considerable attention has been focused on GaAs-on-Si processes because silicon has traditionally been the only source of VLSI circuitry. However, with the recent availability of GaAs-based VLSI, realized using refractory-metal gate processes, we feel that this picture has changed significantly. It is the purpose of this program to demonstrate that the growth of optoelectronic heterostructures on partially processed GaAs-VLSI wafers is a viable alternative to GaAs-on-Si for applications requiring the

⁵ Vitesse Semiconductor, Camarillo, California.

Other applications for these devices include pure FM laser diodes with reduced AM noise, two wavelength integrated but independently controlled laser diodes and other non-laser devices like tunable narrow bandwidth filters and light modulators.

1.9 Design and Fabrication of Distributed Feedback (DFB) InGaAlAs Laser Diodes Grown by Molecular Beam Epitaxy

Sponsors

DARPA/NCIPT
Joint Services Electronics Program
Contract DAAL03-89-C-0001
Contract DAAL03-92-C-0001

Project Staff

Woo-Young Choi, Professor Clifton G. Fonstad, Jr.

It is essential that laser diodes for optical fiber communication applications operate with a single oscillation frequency. Typically, schemes of distributed feedback (DFB) or distributed Bragg reflector (DBR) are used in which gratings above or below the active layer (DFB) or outside the active layer (DBR) perform the act of frequency selection. To make such a device structure, either epitaxial growth is initiated on a corrugated substrate, or regrowth is performed on the epitaxial material onto which gratings have been formed.

In this project, we are in the pursuit of a DFB device structure in which gratings are formed entirely after the complete epitaxial growth. Our motivation for this approach stems from the fact that we are working on laser diodes grown by the conventional solid-source Molecular Beam Epitaxy technology and, due to its growth kinetics, successful MBE growth on the corrugated surface is very difficult to achieve.

We have proposed a ridge stripe structure in which gratings are made on the side walls of the ridge as well as on the bottom channels next to the ridge. According to our initial calculation, there is enough coupling between the optical wave and gratings to result in single mode selection.

To realize such a device structure, we are collaborating with Professor Henry I. Smith's group at MIT and utilizing their x-ray lithography technology. Currently, we are in the process of com-

bining x-ray lithography technology with the ridge-stripe laser diode fabrication technology.

1.10 Laser Diode Modeling and Design for Narrow Linewidth Operation

Sponsor

Charles S. Draper Laboratories

Project Staff

Yakov Royter, Professor Clifton G. Fonstad, Jr. in collaboration with J.H. Hopps⁷

Many of the current laser applications require narrow linewidth output characteristics. Unfortunately, semiconductor lasers, possessing such advantages as small size, direct modulation capability, and integrability with other optical and electronic devices, have broad linewidths in comparison to most other kinds of lasers. The relatively broad linewidths are due to the low Q of the cavity and to the intrinsic effects specific to the semiconductor gain medium. Since most of the linewidth reduction methods have involved the increase of the cavity Q, our goal is to investigate and to help in the reduction of the intrinsic linewidth broadening effects. Reduction of these effects, in conjunction with the increase of the cavity Q, would produce semiconductor lasers with narrowest possible linewidths.

The first step in our research is to investigate theoretically the intrinsic linewidth broadening effects. In particular, we concentrate on the linewidth broadening parameter, α , the largest intrinsic linewidth broadening factor, which describes the coupling of gain and refractive index fluctuations in the gain medium via carrier density fluctuations. Also, due to their apparent promise over conventional diode lasers, we consider only quantum-well semiconductor lasers. We begin the investigation of the α parameter by first calculating the carrier energy bands of the active region semiconductor material, using both parabolic band and $k \cdot p$ approximations. From the energy bands, we can obtain gain and refractive index profiles and the linewidth broadening parameter. Thus, the energy band calculations are the first major task in our investigation.

To test our models, we plan to compare the calculated laser characteristics, such as threshold current, gain, refractive index and linewidth, with

⁷ Charles S. Draper Laboratories, Cambridge, Massachusetts.

be the superior method for optimization because of its speed and convenience.

Small-signal S parameter measurements were made by on-wafer probing of the devices using the Hewlett-Packard 8510B automatic network analyzer and the Cascade Microtech microwave probe station for 39 different bias points. The bias dependence of elements of the small-signal equivalent circuit was determined and it was found that five of the elements of the circuit were highly bias dependent. These results are being used for the large-signal modeling of the HBT which is in progress. Measurements are also in progress to determine the third-order intermodulation product (IP3). The optimized model for high IP3 which is related to device linearity is to be determined.

1.13 Analysis of Three-Terminal n-n-n Quantum Well Base, Tunnel-Barrier Transistors

Sponsor

Joint Services Electronics Program
Contract DAAL03-89-C-0001
Contract DAAL03-92-C-0001

Project Staff

Thomas P.E. Broekaert, Professor Clifton G. Fonstad, Jr.

Three-terminal n-n-n quantum-well base, tunnel barrier transistors, consisting of a resonant tunneling structure with an ohmic contact to the quantum well have been fabricated. Although an ohmic contact to the quantum well was successfully achieved by heavily doping the quantum well, it was found that all such structures exhibit strong leakage currents from base to emitter.

The conductance of surface quantum wells in such transistor structures has been measured successfully, and the dependence of sheet carrier concentration, sheet conductance, and carrier mobility as a function of temperature has been measured. No transistor action was seen for the tested temperature range of 10 to 300 K. The lack of transistor action is tentatively attributed to fast hot carrier relaxation, resulting in large base currents and small collector currents. Possible mechanisms for the hot carrier relaxation are impurity scattering, polar optical phonon scattering, and electron-electron scattering.

Several non-idealities that hamper the active behavior of the resonant tunneling transistor have been analyzed. First, electron-polar optical phonon and electron-electron scattering from second to

first subband in the quantum well are believed to be the dominant mechanisms at low temperatures that limit the ultimate gain of the resonant tunneling transistor. Second, due to the fact that this device only has a single dipole layer, it follows that the emitter accumulation region is not completely shielded from the collector potential, which results in a low output impedance and a low voltage gain.

A novel device structure is introduced, in which the hot carrier relaxation, which is prevalent in InGaAlAs resonant tunneling structures, is reduced. This reduction in hot carrier relaxation rate is obtained by having a quantum well in which the quantum-well level for base potential modulation and the quantum-well level for emitter to collector tunneling are located at different points in the Brillouin zone, e.g., direct vs. indirect valley quantum well. A possible material system for this novel device structure would be GaAs/AlAs/Ge/AlAs/GaAs for emitter/barrier/base/barrier/collector respectively. This material system would also improve the performance of the bipolar quantum-well resonant tunneling transistor and the hot electron transistor.

1.14 Applications of AlAs Etch-Stop Layers in InGaAlAs/InP Heterostructure Electronics and Optoelectronics

Sponsor

Joint Services Electronics Program
Contract DAAL03-89-C-0001
Contract DAAL03-92-C-0001

Project Staff

Thomas P.E. Broekaert, Woo-Young Choi, Professor Clifton G. Fonstad, Jr.

We have used wet chemical etching solutions that allow the selective etching of InP lattice-matched InGaAlAs quaternary compounds using thin pseudomorphic AlAs layers as etch stops to explore new device concepts.

We developed the etchants used here last year, and they typically consist of succinic acid (or other dicarboxylic acids), ammonia, and hydrogen peroxide. The etchant is well buffered and can be used over a wide pH range including from 4.2 to 7.0 by varying the amount of ammonia added. In addition, the etchant is compatible with Cr/Au contact metallization and standard positive photoresists. Typically, the InGaAs etch rate is about 100 nm/min. At a pH of 4.2, the etch rate of InGaAs is found to be over 1000 times the etch

rate of AlAs, while the etch rate of InAlAs is over 500 times that of the AlAs. A typical AlAs stop layer is about 10 monolayers (m.l.) thick (2.73 nm). Buffered HF can be used to remove the AlAs stop layer without etching InGaAlAs to any significant degree.

These selective etchants have enabled us, for the first time, to measure the conductance and mobility of a directly contacted quantum well in a resonant tunneling structure, and they open up the possibility of fabricating a whole new set of novel quantum devices.

Also, we utilized the selective etchants in fabricating ridge-stripe InGaAlAs/InP GRIN-SCH MQW laser diodes. By inserting a thin pseudomorphic AlAs layer at a desired location during the epitaxial growth and then selectively etching away InGaAlAs materials up to the etch stop layer, we were able to fabricate laser devices with ridges whose heights are precisely and reliably controlled.

1.15 Electrical Transport Studies in Directly Contacted InGaAs Quantum Wells

Sponsors

Joint Services Electronics Program

Contract DAAL03-89-C-0001

Contract DAAL03-92-C-0001

National Science Foundation Fellowship

U.S. Army Research Office

Project Staff

Rajni J. Aggarwal, Thomas P.E. Broekaert, Professor Clifton G. Fonstad, Jr.

Using a recently developed selective etch, we have been able to demonstrate direct electrical contact to the quantum well of an AlAs/InAs/InGaAs resonant tunneling structure. This contact serves as the base contact in our three-terminal, unipolar resonant tunneling transistor (RTT). Our devices incorporate high indium content materials in the quantum well. In addition to their favorable transport properties, these compounds have low Schottky barrier heights, enhancing our ability to make ohmic contact to them. We are limited in the indium fraction that we can use by the lattice mismatch of such compounds with the InP based lattice constant of the device.

We believe that the performance of our device is limited by two factors: (1) doping within the quantum well and (2) depletion of the well due to surface exposure. Neither of these problems has

been overcome by the inclusion of high indium content materials alone. We feel that it is necessary to study the nature of the contact itself in order to engineer around the present limitations. Specifically, we are interested in elucidating the effect, if any, of quantization on Schottky barrier height. In addition, we would like to experimentally determine any potential barriers that may exist in electron transport from quasi-confined (contact) regions to confined (intrinsic base) regions within the device.

We are measuring the Schottky barrier height of a variety of quantum well contacts and comparing them to those obtained for comparable bulk materials. Among the experimental variables are quantum well and barrier thickness and well indium content. In addition, we are performing photoluminescence studies in hopes of experimentally observing the shift in energy of the $n=1$ quantum state within the well as one barrier is removed.

1.16 Investigation of Infrared Intersubband Emission from InGaAs/AlAs/InP Quantum Well Heterostructures

Sponsor

National Science Foundation Fellowship

Project Staff

Jurgen H. Smet, Professor Clifton G. Fonstad, Jr. in collaboration with Professor Qing Hu

Subbands in quasi-two-dimensional semiconductor structures exhibit a large electric dipole matrix element, making them attractive as the active medium in an infrared source. Triple quantum-well structures are proposed in which electrons are selectively injected into the second subband of a wide center quantum well. After relaxation to the first subband, electrons are selectively removed. Two important issues need to be addressed: the achievement of population inversion and the confinement of the emitted radiation.

To avoid fast relaxation through electron/LO-phonon scattering, it is desirable to design a structure for a lasing frequency smaller than the LO-phonon frequency. This requires a subband separation of less than 30 meV. This requirement fixes the center well width and the width of the side wells. The balancing of gain and losses determines the required population inversion. The threshold current density is then, in essence, this population inversion divided by the intersubband relaxation time, provided that popu-

Chapter 2. High-Frequency InAlAs/InGaAs Metal-Insulator-Doped Semiconductor Field-Effect Transistors (MIDFETs) for Telecommunications

Academic and Research Staff

Professor Jesús A. del Alamo

Visiting Scientists and Research Affiliates

Dr. Yuji Awano¹

Graduate Students

Sandeep R. Bahl, Brian R. Bennett

Undergraduate Students

Michael H. Leary, Akbar A. Moolji

Technical and Support Staff

Kelley S. Donovan, Angela R. Odoardi

2.1 Introduction

Sponsors

Charles S. Draper Laboratories, Inc.

Contract DL-H-418488

Fujitsu Laboratories

Joint Services Electronics Program

Contract DAAL03-89-C-0001

Contract DAAL03-92-C-0001

Texas Instruments

The goal of this project is to investigate InAlAs/n⁺-InGaAs Metal-Insulator Doped channel Field-Effect Transistors (MIDFETs) on InP. These devices are of great interest for applications in long-wavelength lightwave communication systems and ultra-high frequency high-power microwave telecommunications.

InAlAs/InGaAs Modulation-Doped Field-Effect Transistors (MODFETs) on InP have recently emerged as an optimum choice for a variety of microwave and photonics applications. This is

because the outstanding transport properties of InGaAs have yielded devices with very low-noise and high-frequency characteristics. Unfortunately, the low breakdown voltage of InAlAs/InGaAs MODFETs on InP (typically less than 5 V) severely restricts their use in high-power applications, such as large-signal microwave amplification and laser driving. It also forces the use of a separate high voltage supply to operate the Metal-Semiconductor-Metal (MSM) photodetectors in InP photonics receivers.

A device strategy with great potential for power handling is the InAlAs/n⁺-InGaAs MIDFET featuring an undoped insulator and a thin, heavily-doped channel. In this structure, the breakdown voltage, V_B , is large and can be engineered using pseudomorphic insulators² and channel quantization (shown below). Drain current, I_D , can also be considerably improved with InAs-rich channels.³ The attainment of high power, however, demands a large $I_D \times V_B$ product. InAs-rich channel devices unfortunately suffer from a low breakdown voltage due to: (1) the reduced channel bandgap, and (2)

¹ Fujitsu Laboratories, Atsugi, Japan.

² S.R. Bahl, W.J. Azzam, and J.A. del Alamo, "Strained-Insulator In_xAl_{1-x}As/n⁺-In_{0.53}Ga_{0.47}As Heterostructure Field-Effect Transistors," *IEEE Trans. Electron Dev.* 38(9): 1986-1992 (1991).

³ S.R. Bahl and J.A. del Alamo, "An In_{0.52}Al_{0.48}As/n⁺-In_xGa_{1-x}As Heterostructure Field-Effect Transistor with an In-Enriched Channel," *Proceedings of the Second International Conference on InP and Related Compounds*, Denver, Colorado, April 23-25, 1990, p. 100.

severe gate leakage at the sidewall of the mesa, where the gate comes in contact with the heavily-doped channel.⁴

Towards solving this severe problem in this period of performance, we have studied the effect of quantizing the InGaAs channel. This has resulted in a drastically improved breakdown voltage through a quantum mechanically engineered enlargement of the effective bandgap of the channel. We have also solved the isolation problem through a selective chemical recessing of the edge of the channel on the mesa sidewall. We have finally integrated all our understanding developed over the last three years into a device with a strained (InAs-rich) channel, strained (AlAs-rich) insulator, quantized channel, optimized channel doping, and edge isolated device which has displayed unprecedented power and frequency performance. A detailed description of these experiments is presented in this report.

2.2 Quantum-channel InAlAs/n⁺-InGaAs MIDFETs

In previous work, we have shown that enriching the InAs mole fraction of In_{0.53}Ga_{0.47}As channel results in MIDFETs with superior transport properties. However this comes at the cost of a severely reduced breakdown voltage, V_B , presumably through the decrease in the energy gap, E_g .³ A method of increasing the effective energy gap in the channel is to introduce energy quantization by reducing the channel thickness to dimensions comparable to the electron wavelength (figure 1). In fact, it has been shown that in In_{0.53}Ga_{0.47}As/In_{0.52}Al_{0.48}As quantum wells the photoluminescence emission wavelength decreases⁵ with a reduction in well thickness.

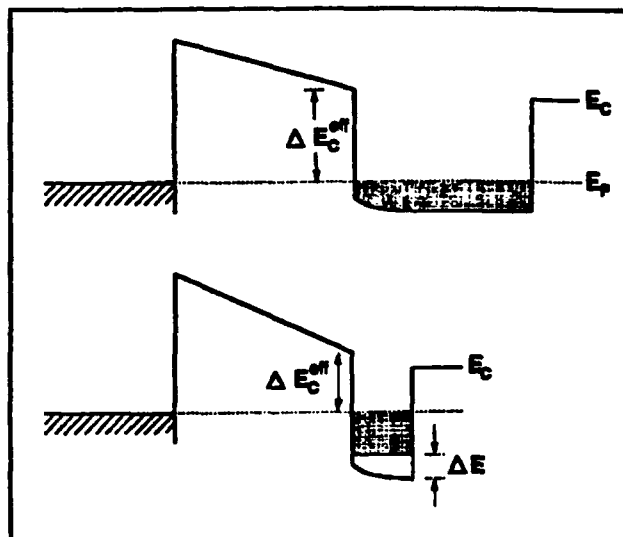


Figure 1. Schematic conduction band diagrams in equilibrium of InAlAs/n⁺-InGaAs HFETs for thick and thin channels, showing the increase in effective energy gap in the thinner channel.

In this work, we exploit this effect to enhance the breakdown voltage of In_{0.52}Al_{0.48}As/n⁺-In_{0.53}Ga_{0.47}As MIDFETs on InP. We have doubled V_B by shrinking the In_{0.53}Ga_{0.47}As channel thickness from 350Å to 100Å, keeping other physical parameters constant. The principle behind our work should allow one to better exploit the excellent transport properties of InAs-rich InGaAs and other promising narrow gap semiconductors like InAs⁶ and InSb.

A cross section of the device structure is shown in figure 2. The wafers were grown on Si-InP by MBE in MIT's Riber 2300 system. In an effort to keep the channel charge constant, the thickness of its undoped portion was varied while the thickness of its heavily doped portion was kept constant at 100Å. Four wafers were subsequently grown with subchannel thicknesses of 250Å, 100Å, 50Å, and 0Å, i.e., total channel thicknesses of 350Å, 200Å, 150Å, and 100Å. Devices were fabricated with nominal gate lengths of 1 μm and widths of 30

⁴ S.R. Bahl and J.A. del Alamo, "An In_{0.52}Al_{0.48}As/n⁺-In_{0.53}Ga_{0.47}As Heterostructure Field-Effect Transistor with an In-Enriched Channel," *Proceedings of the Second International Conference on InP and Related Compounds*, Denver, Colorado, April 23-25, 1990, p. 100.

⁵ D.F. Welch, G.W. Wicks, and L.F. Eastman, "Optical Properties of GaInAs/AlInAs Single Quantum Wells," *Appl. Phys. Lett.* 43(8): 762-764 (1983); W. Stolz, K. Fujiwara, L. Tapfer, H. Oppolzer, and K. Ploog, "Luminescence of In_{0.53}Ga_{0.47}As/In_{0.52}Al_{0.48}As Quantum Well Heterostructures Grown by Molecular Beam Epitaxy," *Inst. Phys. Conf. Ser.* 74(3): 139-144 (1985).

⁶ C.C. Eugster, T.P. Broekaert, J.A. del Alamo, and C.G. Fonstad, "An InAlAs/InAs MODFET," *IEEE Electron Dev. Lett.* 12(12): 707-709 (1992).

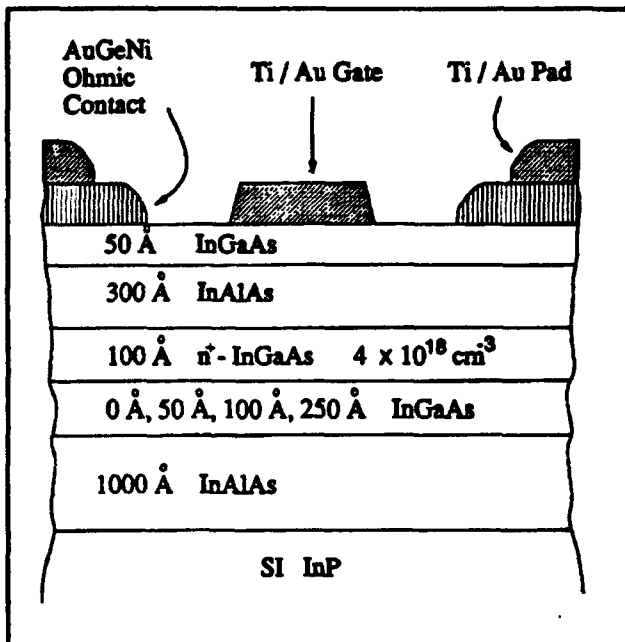


Figure 2. Cross-section of grown device structures in quantum-channel experiment.

μm . Fabrication is similar to that used in Bahl, Azzam, and del Alamo (1991).⁷

Our baseline device, 200Å channel thickness, had a peak transconductance, $g_{m(\text{peak})}$, of 202 mS/mm and a maximum drain current, $I_{d(\text{max})}$, of 312 mA/mm. The output conductance, g_d , was 5.73 mS/mm, resulting in a voltage gain, A_v , of 35. These are average values over five devices. $g_{m(\text{peak})}$ and $I_{d(\text{max})}$ were measured at $V_{ds} = 4$ V, and g_d at $V_{ds} = 4$ V and $V_{gs} = 0$ V. The contact and channel sheet resistances, measured by TLM, are 0.37 $\Omega \cdot \text{mm}$ and 625 Ω/\square , respectively.

The reverse gate breakdown voltage, V_B , was measured with the source and drain grounded, and was defined at a reverse gate current of 500 μA , corresponding to about 5% of the peak drain current of our baseline device.⁸ Here we focus on our main result: the increased breakdown voltage in devices with thinner channels and the exper-

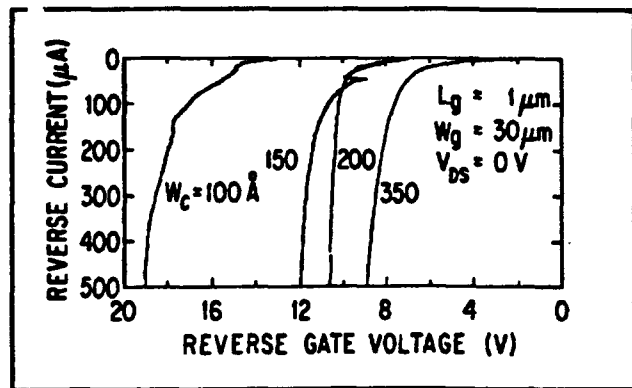


Figure 3. Breakdown voltage, V_B , for typical HFETs with channel thicknesses of 100Å, 150Å, 200Å, and 350Å.

imental confirmation of the energy quantization therein.

Figure 3 shows typical reverse gate I-V characteristics of HFETs as a function of channel thickness. As shown, V_B increases gradually from 9 V at a channel thickness of 350Å to 10.6 V at 200Å, 11.9 V at 150Å, and to 19.1 V at 100Å. Average V_B measurements over several devices are within 1 V of the typical values shown in figure 3. V_B for the 200Å channel is also similar to what we have previously measured in identical devices grown and processed separately.⁸ The drastic improvement in breakdown voltage of our quantized-channel HFETs is a significant merit for high-power applications. This is particularly so in this material system because typical InAlAs/InGaAs MODFET breakdown voltages are on the order of 5 V.⁹

In order to verify the bandgap enhancement in the channel as a result of carrier quantization, we have carried out photoluminescence (PL) measurements on unprocessed portions of the device samples at 77 K. The results are shown in figure 4. The energy of the peak PL intensity increases from 0.83 eV for the 350Å channel, to 0.86 for 200Å, to 0.88 for 150Å, and to 0.92 eV for the 100Å channel. The literature reports a temperature-independent PL energy shift of about 60 meV over

⁷ S.R. Bahl, W.J. Azzam, and J.A. del Alamo, "Strained-Insulator $\text{In}_x\text{Al}_{1-x}\text{As}/\text{n}^+-\text{In}_{0.53}\text{Ga}_{0.47}\text{As}$ Heterostructure Field-Effect Transistors," *IEEE Trans. Electron Dev.* 38(9): 1986-1992 (1991).

⁸ S.R. Bahl and J.A. del Alamo, "An $\text{In}_{0.52}\text{Al}_{0.48}\text{As}/\text{n}^+-\text{In}_x\text{Ga}_{1-x}\text{As}$ Heterostructure Field-Effect Transistor with an In-Enriched Channel," *Proceedings of the Second International Conference on InP and Related Compounds*, Denver, Colorado, April 23-25, 1990, p. 100.

⁹ P.C. Chao, A.J. Tessmer, K.-H.G. Duh, P. Ho, M.-Y. Kao, P.M. Smith, J.M. Ballingall, S.-M. Liu, and A.A. Jabra, "W-band Low-Noise InAlAs/InGaAs Lattice-Matched HEMT's," *IEEE Electron Dev. Lett.* 11(1): 59-62 (1990); Y.-C. Pao, C.K. Nishimoto, R. Majidi-Ahy, J. Archer, N.G. Bechtel, and J.S. Harris, Jr., "Characterization of Surface-Undoped $\text{In}_{0.52}\text{Al}_{0.48}\text{As}/\text{In}_{0.53}\text{Ga}_{0.47}\text{As}/\text{InP}$ High Electron Mobility Transistors," *IEEE Trans. Electron. Dev.* 37(10): 2165-2170 (1990).

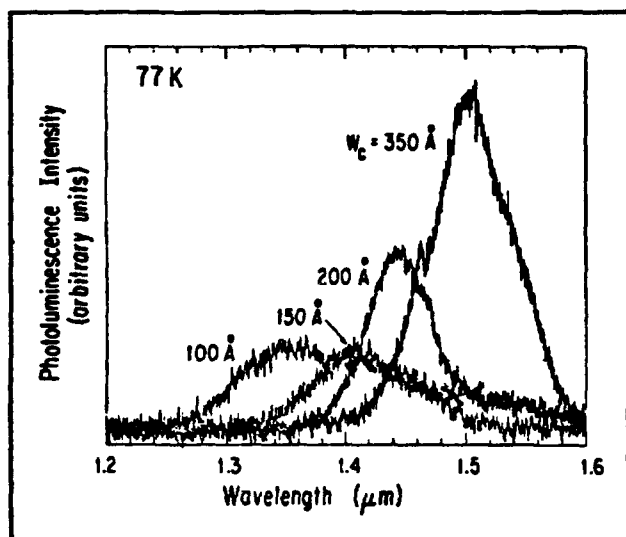


Figure 4. Photoluminescence spectra of the device heterostructures, showing an increase in photoluminescence energy with decreasing channel thickness.

the $\text{In}_{0.53}\text{Ga}_{0.47}\text{As}$ bulk value for 100 Å thick $\text{In}_{0.52}\text{Al}_{0.48}\text{As}/\text{In}_{0.53}\text{Ga}_{0.47}\text{As}$ quantum wells.¹⁰ This value of 60 meV is also consistent with simple calculations for a finite square well of thickness 100 Å. Our slightly larger shift of 90 meV in the 100 Å channel might be due to depletion at the top and possibly bottom interfaces, causing a reduced effective well thickness. Additionally, band bending in the insulator results in an effective stronger potential than a square well (figure 1). Both effects will tend to enhance the strength of carrier quantization over a simple quantum well.

Electron quantization, as schematically shown in figure 1, also implies a reduction of the effective

conduction band discontinuity between channel and metal gate. This, in return, is expected to result in enhanced forward gate leakage current. We have experimentally found this to be the case at 300 K and 77 K,¹¹ providing us in this manner with an independent confirmation of the presence of quantization in the channel.

Unfortunately, we have found that a reduction in the channel thickness results in the degradation of transconductance and peak drain current.¹¹ $g_{m(\text{peak})}$ decreases from 262 mS/mm to 138 mS/mm, and $I_{d(\text{max})}$ from 451 mA/mm to 208 mA/mm in going from a channel thickness of 350 Å to 100 Å. However, the output conductance g_d , improves due to the enhanced channel aspect ratio, decreasing from 10.8 mS/mm to 1.84 mS/mm. This results in an enhancement in the voltage gain, A_v , from 24 to 75. The degradation in $g_{m(\text{peak})}$ and $I_{d(\text{max})}$ results from an increased source resistance R_s , a reduced channel sheet charge concentration n_s , and degraded mobility, μ . From 350 Å to 100 Å, R_s increases from $1.4 \Omega \cdot \text{mm}$ to $2.7 \Omega \cdot \text{mm}$, n_s drops from $2.38 \times 10^{12} \text{ cm}^{-2}$ to $1.77 \times 10^{12} \text{ cm}^{-2}$, and μ decreases from $4318 \text{ cm}^2/\text{V}\cdot\text{s}$ to $3591 \text{ cm}^2/\text{V}\cdot\text{s}$. n_s and μ were measured by the Hall-effect. The acknowledged poor quality of the reverse $\text{InGaAs}/\text{InAlAs}$ interface at the back of the channel can be held responsible for the mobility reduction.¹² As the undoped sub-channel is thinned down, the reverse interface has a larger impact on carrier mobility since the channel electrons travel closer to the reverse $\text{InAlAs}/\text{InGaAs}$ interface. There are, however, techniques that could mitigate this degradation: superlattice buffers to improve mobility¹³ and the Migration-Enhanced Epitaxy (MEE) growth technique to reduce interface roughness.¹⁴

¹⁰ D.F. Welch, G.W. Wicks, and L.F. Eastman, "Optical Properties of $\text{GaInAs}/\text{AlInAs}$ Single Quantum Wells," *Appl. Phys. Lett.* 43(3): 762-764 (1983); W. Stolz, K. Fujiwara, L. Tapfer, H. Oppolzer, and K. Ploog, "Luminescence of $\text{In}_{0.53}\text{Ga}_{0.47}\text{As}/\text{In}_{0.52}\text{Al}_{0.48}\text{As}$ Quantum Well Heterostructures Grown by Molecular Beam Epitaxy," *Inst. Phys. Conf. Ser.* 74(3): 139-144 (1985).

¹¹ S.R. Bahl and J.A. del Alamo, "A Quantized-channel $\text{In}_{0.52}\text{Al}_{0.48}\text{As}/\text{n}^+-\text{In}_{0.53}\text{Ga}_{0.47}\text{As}$ HFET with High Breakdown Voltage," Extended Abstracts of the Materials Research Society 1990 Fall Meeting, Boston, Massachusetts, no. EA-21, p. 117.

¹² A.S. Brown, J.A. Henige, and M.J. Delaney, "Photoluminescence Broadening Mechanisms in High Quality $\text{GaInAs}/\text{AlInAs}$ Quantum Well Structures," *Appl. Phys. Lett.* 52(14): 1142-1143 (1988); T. Sajoto, M. Santos, J.J. Heremans, M. Shayegan, M. Heiblum, M.V. Weckwerth, and U. Meirav, "Use of Superlattices to Realize Inverted $\text{GaAs}/\text{AlGaAs}$ Heterojunctions with Low-temperature Mobility of $2 \times 10^6 \text{ cm}^2/\text{V}\cdot\text{s}$," *Appl. Phys. Lett.* 54(9): 840-842 (1989).

¹³ T. Sajoto, M. Santos, J.J. Heremans, M. Shayegan, M. Heiblum, M.V. Weckwerth, and U. Meirav, "Use of Superlattices to Realize Inverted $\text{GaAs}/\text{AlGaAs}$ Heterojunctions with Low-temperature Mobility of $2 \times 10^6 \text{ cm}^2/\text{V}\cdot\text{s}$," *Appl. Phys. Lett.* 54(9): 840-842 (1989).

¹⁴ Y.C. Chen, P. Bhattacharya, and J. Singh, "Strained Layer Epitaxy of InGaAs (on GaAs) by MBE and Migration Enhanced Epitaxy - Comparison of Growth Modes and Surface Quality," *J. Cryst. Growth* 111(1-4): 228-232 (1991).

Thinning down the subchannel reduces the sheet carrier concentration, possibly from backside depletion. A reduced channel doping can also result in an improvement of breakdown voltage. In a separate experiment on similar devices (with 200 Å channel thickness), we examined the impact of channel doping on V_B . This experiment indicated that a reduction in sheet charge concentration from $2.38 \times 10^{12} \text{ cm}^{-2}$ to $1.77 \times 10^{12} \text{ cm}^{-2}$ should result in an improvement of V_B by 5 V. Our experimental observation of a 10 V improvement in going from a 350 Å to 100 Å channel is evidence that quantization is instrumental in drastically enhancing the breakdown characteristics of our HFETs.

In conclusion, $\text{In}_{0.52}\text{Al}_{0.48}\text{As}/n^+-\text{In}_{0.53}\text{Ga}_{0.47}\text{As}$ HFETs have been fabricated with channel thicknesses of 100 Å, 150 Å, 200 Å, and 350 Å. For devices with channel thicknesses of 100 Å, the breakdown voltage improved twofold over the 350 Å devices. This is postulated to arise partially from an enlargement of the effective energy gap caused by energy quantization introduced from electron confinement, as observed by PL.

2.2.1 Elimination of Mesa-Sidewall Gate-Leakage Current by Selective Sidewall Recessing

We have shown in previous work¹⁵ that fabrication of $\text{InAlAs}/n^+-\text{InGaAs}$ MIDFETs by conventional mesa isolation results in sidewalls where the InGaAs channel is exposed and comes in contact with the gate metallization running up the mesa (figure 5). The low Schottky barrier height of metals on InGaAs ¹⁶ potentially results in a sidewall leakage path from the gate to the channel. Sidewall-leakage in $\text{InAlAs}/\text{InGaAs}$ HFETs results

in excessive gate-leakage current,¹⁵ reduced breakdown voltage,¹⁶ and increased sidgating.¹⁷ In HFETs, sidewall-leakage was also found, by the present authors, to worsen with high doping, an increased channel thickness, and increased x ($x > 0.53$) in the $\text{In}_x\text{Ga}_{1-x}\text{As}$ channel.¹⁸ This latest trend is particularly consequential, since HFETs with InAs enriched channels have shown excellent electron transport properties.¹⁹

Airbridging and ion implantation have been utilized in InGaAs HFET isolation. Airbridging is complex, and implantation demands capital-intensive tools. In this paper, we propose and demonstrate a new, simpler technique by which we selectively recess the exposed InGaAs channel into the sidewall. The subsequently e-beamed gate metallization does not enter this cavity and remains isolated from the channel edge. This one-step technique is self aligned to the mesa, requires no additional masks, gate-length insensitive, and works for mesas in all crystallographic directions on the (100) surface.

The MBE grown heterostructure, lattice-matched to S.I. InP , consists of (bottom to top) a 1000 Å undoped $\text{In}_{0.52}\text{Al}_{0.48}\text{As}$ buffer layer, an $\text{In}_{0.53}\text{Ga}_{0.47}\text{As}$ channel consisting of a 100 Å undoped subchannel and a 80 Å heavily Si doped ($N_D = 6 \times 10^{18} \text{ cm}^{-3}$) transport layer, a 300 Å undoped $\text{In}_{0.52}\text{Al}_{0.48}\text{As}$ gate insulator layer, and an undoped 50 Å $\text{In}_{0.53}\text{Ga}_{0.47}\text{As}$ cap. For clarity in SEM imaging, an additional heterostructure with a thicker $\text{In}_{0.53}\text{Ga}_{0.47}\text{As}$ channel (120 Å doped and 300 Å undoped) was processed along with the device sample.

Devices were fabricated by first chemically etching a mesa down to the InP substrate using a $\text{H}_2\text{SO}_4:\text{H}_2\text{O}_2:\text{H}_2\text{O}$ 1:10:220 etch. Then, before removing the mesa-level photoresist mask, the wafer was dipped for 45 seconds into a $\text{SA}:\text{H}_2\text{O}_2$

¹⁵ S.R. Bahl and J.A. del Alamo, "An $\text{In}_{0.52}\text{Al}_{0.48}\text{As}/n^+-\text{In}_x\text{Ga}_{1-x}\text{As}$ Heterostructure Field-Effect Transistor with an In-Enriched Channel," *Proceedings of the Second International Conference on InP and Related Compounds*, Denver, Colorado, April 23-25, 1990, p. 100.

¹⁶ H.H. Wieder, "Fermi Level and Surface Barrier of $\text{Ga}_x\text{In}_{1-x}\text{As}$ Alloys," *Appl. Phys. Lett.* 38(3): 170-171 (1981).

¹⁷ Y.-J. Chan, D. Pavlidis, and G.-I. Ng, "The Influence of Gate-Feeder/Mesa-Edge Contacting on Sidgating Effects in $\text{In}_{0.52}\text{Al}_{0.48}\text{As}/n^+-\text{In}_{0.53}\text{Ga}_{0.47}\text{As}$ Heterostructure FET's," *IEEE Electron Dev. Lett.* 12 (7): 360-362 (1991).

¹⁸ S.R. Bahl and J.A. del Alamo, "An $\text{In}_{0.52}\text{Al}_{0.48}\text{As}/n^+-\text{In}_x\text{Ga}_{1-x}\text{As}$ Heterostructure Field-Effect Transistor with an In-Enriched Channel," *Proceedings of the Second International Conference on InP and Related Compounds*, Denver, Colorado, April 23-25, 1990, p. 100; S.R. Bahl, M.H. Leary, and J.A. del Alamo, "Mesa-Sidewall Gate-Leakage in $\text{InAlAs}/\text{InGaAs}$ Heterostructure Field-Effect Transistors," submitted for publication.

¹⁹ S.R. Bahl and J.A. del Alamo, "An $\text{In}_{0.52}\text{Al}_{0.48}\text{As}/n^+-\text{In}_x\text{Ga}_{1-x}\text{As}$ Heterostructure Field-Effect Transistor with an In-Enriched Channel," *Proceedings of the Second International Conference on InP and Related Compounds*, Denver, Colorado, April 23-25, 1990, p. 100; U.K. Mishra, A.S. Brown, and S.E. Rosenbaum, "DC and RF Performance of 0.1 μm Gate Length $\text{Al}_{0.48}\text{In}_{0.52}\text{As}-\text{Ga}_{0.38}\text{In}_{0.62}\text{As}$ Pseudomorphic HEMT's," *Proceedings of the International Electron Device Meeting*, 1988, pp. 180-183.

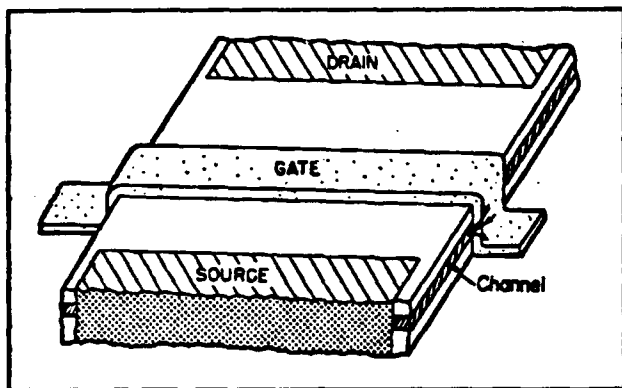


Figure 5. Three-dimensional perspective of an HFET showing the mesa-sidewall gate-leakage path.

6:1 solution²⁰ to selectively etch the exposed portion of the $\text{In}_{0.53}\text{Ga}_{0.47}\text{As}$ channel in a self-aligned manner. The SA solution was prepared by adding 1 liter H_2O to 200 g. succinic acid with the addition of ammonium hydroxide until the pH was 5.5. A planar selectivity of 23:1 was measured, with the $\text{In}_{0.52}\text{Al}_{0.48}\text{As}$ etching at $25\text{\AA}/\text{min}$. For reference, a portion of the wafer was masked during this etch by coating with photoresist using a

paintbrush. In this portion, mesa etching was performed, but no selective sidewall-recessing was carried out. For the ohmic contacts, 2000\AA of AuGe and 600\AA of Ni were evaporated, lifted off, and RTA alloyed at 360°C . For the gate and pad, 300\AA of Ti, 300\AA of Pt, and 2000\AA of Au were e-beam evaporated and lifted off. This process should be compatible with recessed-gate devices. If the same etchant is used for gate-recessing, then sidewall-recessing could be performed simultaneously.

To study sidewall-leakage, we fabricated special-purpose heterojunction diodes with an active Schottky area of $10,000\text{ }\mu\text{m}^2$. Gate-metal/mesa-sidewall overlaps were created by etching grooves through the active diode during mesa formation, and then depositing gate metal on top. The ohmic contact surrounds the gate region. Twelve diodes were fabricated in each die, with sidewall-overlap lengths, L_s , of 0, 200, 400, and $600\text{ }\mu\text{m}$, running in each of [011], [001] and [011] crystallographic directions. Figure 6 shows a photograph of the diode test structure with various sidewall-overlap lengths along one selected crystallographic direction.

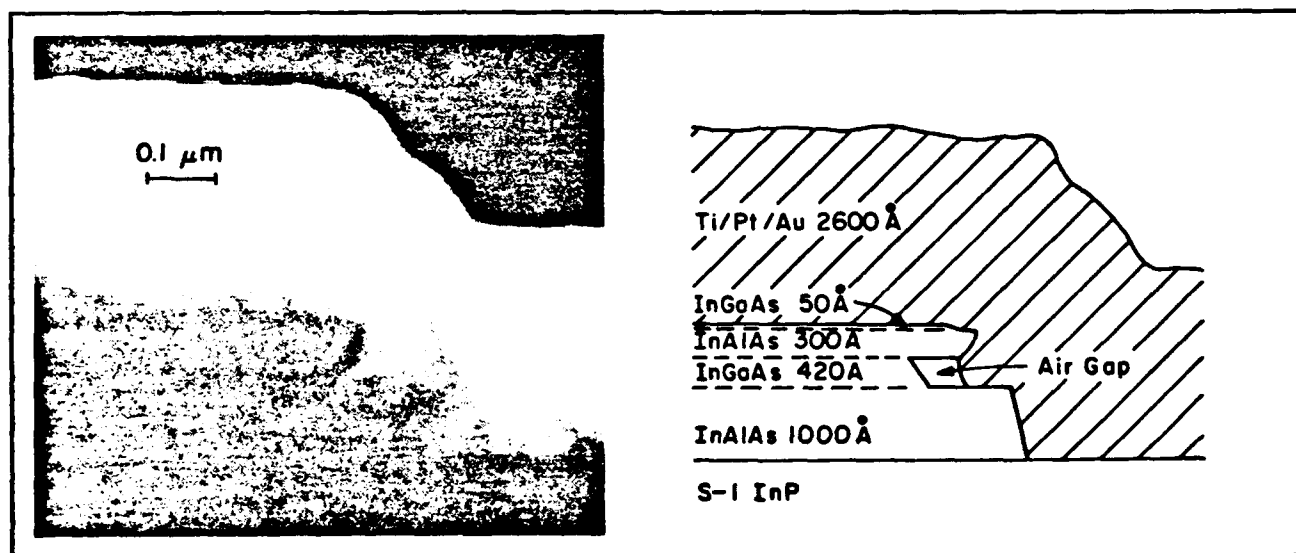


Figure 6. Photograph of sidewall-leakage test diodes with $10,000\text{ }\mu\text{m}^2$ area and sidewall overlap lengths of (left to right) 600, 400, 200, and $0\text{ }\mu\text{m}$.

²⁰ T.P.E. Broekaert and C.G. Fonstad, "AlAs Etch-Stop Layers for InGaAsAs/InP Heterostructure Devices and Circuits," *IEEE Trans. Electron Dev.*, forthcoming (1992).

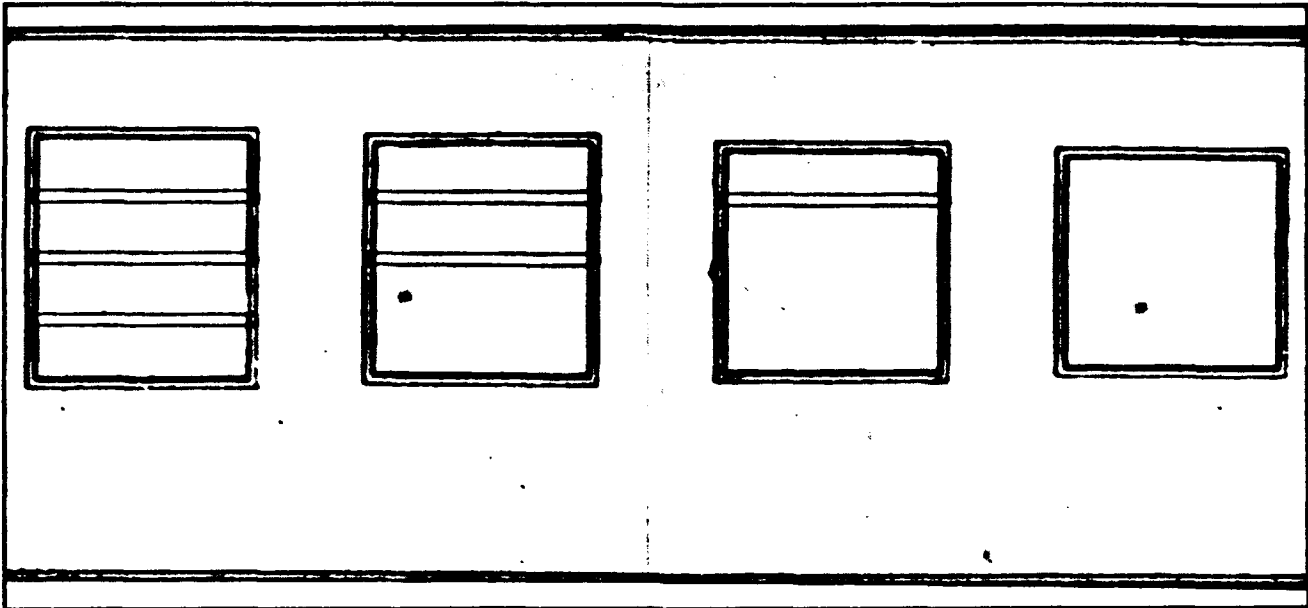


Figure 7. SEM photograph and explanatory sketch of the heterostructure sidewall, showing the isolation of the gate metal from the channel.

Figure 7 shows an SEM photograph and a sketch of the finished heterostructure with 420 Å $\text{In}_{0.53}\text{Ga}_{0.47}\text{As}$ channel processed with the other device samples. The presence of a sidewall cavity is clearly revealed. This confirms the successful action of the selective etchant. The overhang formed by the InAlAs insulator prevents the gate from contacting the channel edge.

Figure 8 shows the I-V characteristics of typical heterojunction diodes from the non-sidewall-recessed portion of the wafer with grooves along the $[0\bar{1}1]$ direction. Both forward and reverse diode currents increase with sidewall-overlap length, as expected from the increase in contact area. This unmistakably proves the existence of a significant sidewall-leakage path. The figure shows that sidewall-leakage plays a major role from forward-bias till threshold (-0.82 V), when the channel is depleted. We also find (not shown) that sidewall-leakage depends on crystallographic orientation as $I[0\bar{1}1] > I[001] > I[011]$. For typical diodes with $L_g = 200$ μm , I increases by 38% from $[011]$ to $[0\bar{1}1]$ at $V = -2$ V.

In the sidewall-recessed portion of the wafer, both sidewall-length and orientation dependence of the diode current have disappeared. This is shown in figure 9, a plot of the I-V characteristics of twelve

diodes (one of each stripe and orientation) from the sidewall isolated portion of the wafer. All reverse characteristics are tightly clustered and randomly distributed around the baseline area leakage characteristic observed for zero overlap length in figure 8. The absence of orientation and overlap length dependence confirms that sidewall-leakage has been completely eliminated for all crystallographic orientations.

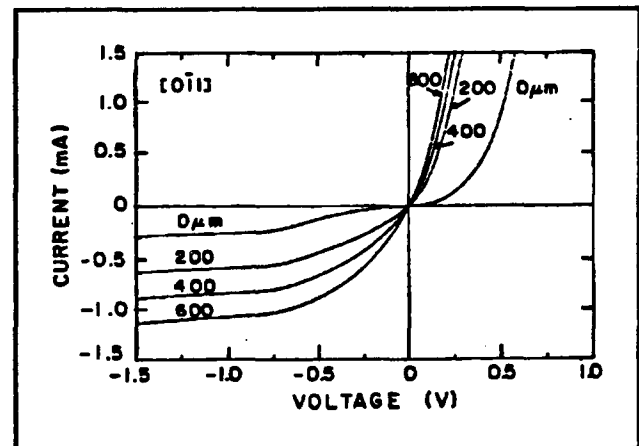


Figure 8. I-V characteristics of test diodes without sidewall recessing, as a function of sidewall overlap length along the $[011]$ direction on the wafer surface.

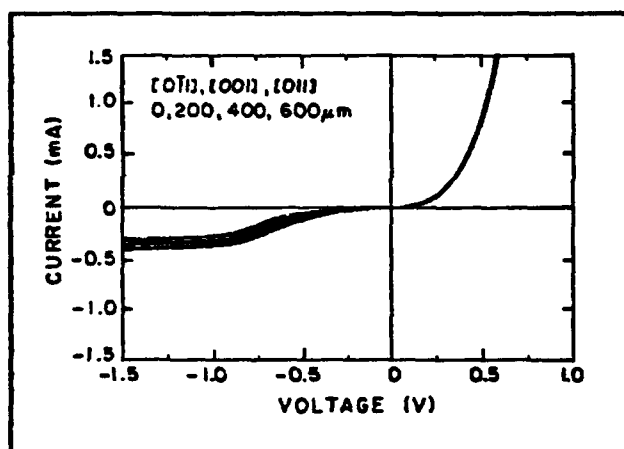


Figure 9. I-V characteristics of test diodes with sidewall recessing, for different orientations and sidewall overlap lengths.

On the same wafer, we have also fabricated HFETs with nominal gate length, L_g , and width, W_g , of 1 μm and 30 μm respectively. Figure 10 shows the impact of sidewall isolation on the gate characteristics. Sidewall isolation results in lower gate-leakage current, a larger gate turn-on voltage, and an increased breakdown voltage. The complete elimination of sidewall-leakage in HFETs was confirmed by the disappearance in orientation dependence of the subthreshold current (not shown) at several gate-lengths.

In conclusion, a simple self-aligned technique for eliminating mesa-sidewall gate-leakage has been developed. This technique uses selective etching to etch the exposed part of the InGaAs channel into the mesa-sidewall, creating a cavity to isolate the channel from the gate. Measurements on specially designed diodes have shown complete elimination of sidewall-leakage. This process should be useful for any kind of heterostructure in the InAlAs/InGaAs system.

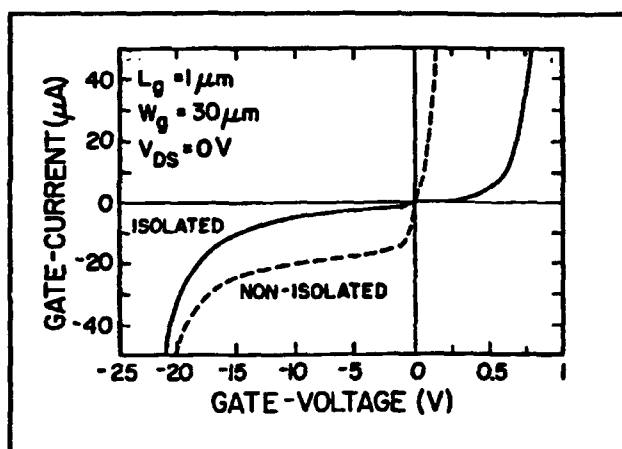


Figure 10. Gate-diode characteristics of HFETs, with and without sidewall isolation, for $L_g = 1 \mu\text{m}$ and mesa sidewall along [011].

2.2.2 Doubly Strained InAlAs/ n^+ -InGaAs HFET

In this section, we pull together all the knowledge developed over the last three years on InAlAs/ n^+ -InGaAs MIDFETs and present an original device design that features for the first time: (1) complete elimination of sidewall leakage, (2) an optimized channel doping level, and (3) high electron confinement by using a strained (AlAs-rich) insulator and a quantized and strained (InAs-rich) channel. The resulting device, though moderate in L_g , displays unprecedented power handling capabilities.

The MBE grown HFET (figure 11) on S.I. InP consists of (bottom to top), a 1000Å $\text{In}_{0.52}\text{Al}_{0.48}\text{As}$ buffer, a 75Å $\text{In}_{0.53}\text{Ga}_{0.47}\text{As}$ subchannel, a 100 Å n^+ - $\text{In}_x\text{Ga}_{1-x}\text{As}$ channel, a 300Å $\text{In}_{0.41}\text{Al}_{0.59}\text{As}$ strained insulator, and a 50Å $\text{In}_{0.53}\text{Ga}_{0.47}\text{As}$ cap. The insulator thickness and mole fraction were chosen to avoid misfit dislocations while providing maximum conduction band discontinuity. The subchannel thickness was chosen to introduce electron quantization and increase E_g in the channel without significantly degrading current driving capability. The impact of channel doping was examined by growing three wafers with lattice matched ($x = 0.53$) channels nominally doped to 4, 6, and 8 $\times 10^{18} \text{ cm}^{-3}$. From power considerations, as indicated below, an optimum doping level of 6 $\times 10^{18} \text{ cm}^{-3}$ was selected. This is the doping at which the InAs-rich channel ($x=0.65$) device was grown.

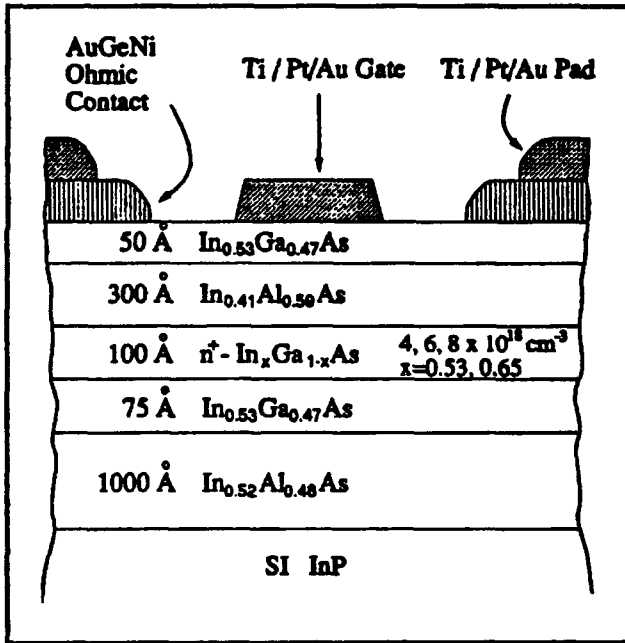


Figure 11. Cross-section of doubly-strained device structure.

Devices (see sketch in figure 11) were processed by mesa etching, sidewall isolation etching, RTA alloying of lifted-off Ge/Au/Ni ohmic contacts, and lifting-off Ti/Pt/Au gates and pads. Sidewall isolation was done by selectively etching the InGaAs channel edge into the sidewall to create a cavity. Gate-metal running up the mesa sidewall does not enter the cavity, and therefore does not contact the channel edge. Measurements are reported for 1.9 μm gate length (L_g) HFETs. All DC measurements are averaged over several devices.

In our $x=0.53$ channel devices, higher channel doping results in higher $I_{D(\text{max})}$, but lower V_B . $I_{D(\text{max})}$ for dopings of 4, 6, and $8 \times 10^{18} \text{ cm}^{-3}$ is respectively 117, 220, and 371 mA/mm. V_B is 21.1, 15.6, and 5.3 V, giving an $I_{D(\text{max})} \times V_B$ product of 2.5, 3.4, and 2.0 W/mm respectively. f_t and f_{max} also increase with doping. f_t is 9.2, 11.3, and 12.8 GHz, and f_{max} is 34, 42, and 68 GHz, respectively.

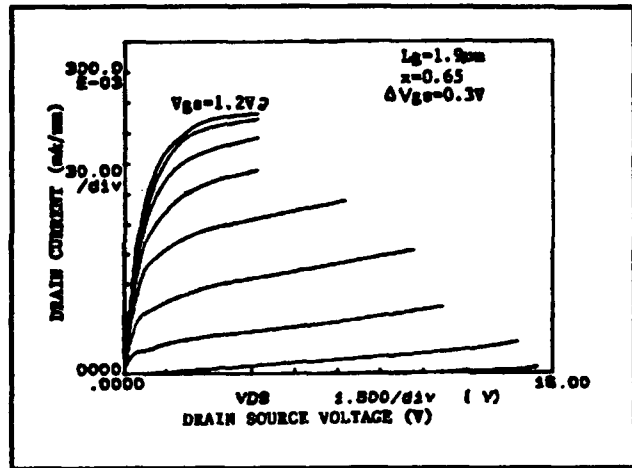


Figure 12. I-V characteristics of $x=0.65$ HFET.

For our doubly-strained InAs-rich ($x=0.65$) channel device, we found $g_{m(\text{peak})} = 201 \text{ mS/mm}$, and $I_{D(\text{max})} = 276 \text{ mA/mm}$ (figure 12). f_t was 14.9 GHz and f_{max} 101 GHz (figure 13). This gives an effective electron velocity of $1.8 \times 10^7 \text{ cm/sec}$ for our 1.9 μm L_g , comparable to values obtained in MODFETs of similar L_g 's. The high f_{max} is a consequence of low g_d (0.9 mS/mm at peak f_t) as this device is now able to enter accumulation at $V_{gs} \geq 0 \text{ V}$. The voltage gain at peak f_t is 150. The average V_B was 12.8 V (figure 14). This results in an average $I_D \times V_B$ product of 3.5 W/mm. Devices capable of handling as much as $I_D \times V_B = 4 \text{ W/mm}$ were obtained. These values represent an improvement over similar gate length MODFETs of 2 to 3 times. High electron confinement and reduced gate leakage in these HFETs are instrumental in obtaining these values.

In conclusion, in the pursuit of high-power InAlAs/InGaAs HFETs, we have combined for the first time in a single device, an optimized heavily-doped channel, an AlAs enriched insulator, an InAs enriched channel, channel quantization, and mesa-sidewall leakage elimination. We have thereby been able to fabricate a high-voltage, high-current device with excellent microwave characteristics. Scaled down versions of this device are very promising for high-power microwave and photonics applications.

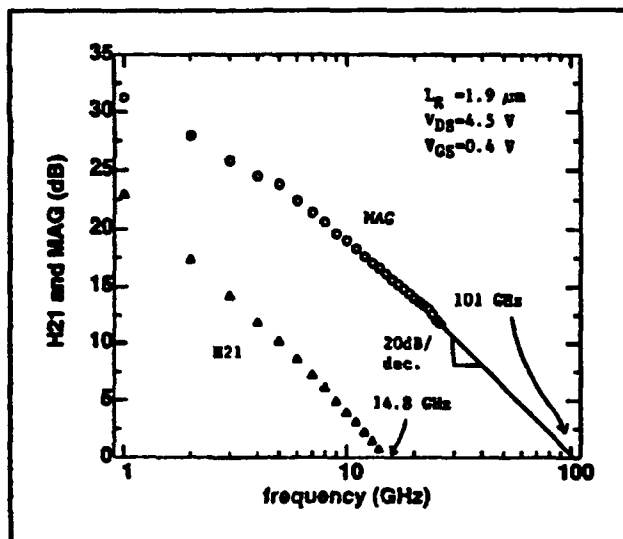


Figure 13. H_{21} and MAG vs. frequency for $x=0.65$.

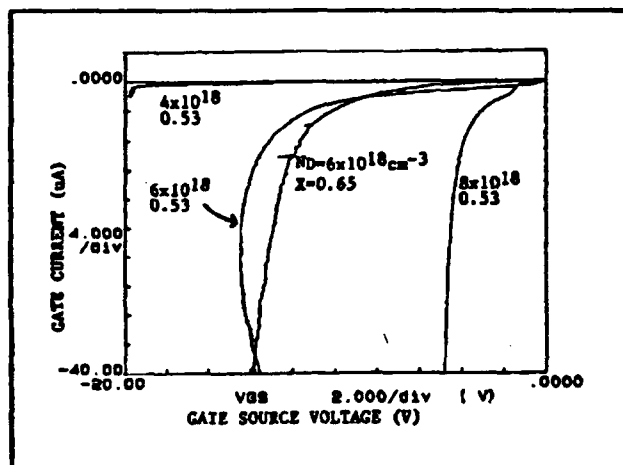


Figure 14. Reverse I_g vs. V_{gs} characteristics for typical HFETs showing that our improvements have mitigated the degradation in V_B for $x=0.65$ ($W_g = 30\mu m$).

2.2.3 Publications and Meeting Papers

Bahl, S.R., and J.A. del Alamo.

"InAlAs/ n^+ -InGaAs HFETs: Impact of Dislocations and Channel Quantization." Paper presented at the Workshop on Compound Semiconductors Materials and Devices (WOCSEMMAD), Ft. Lauderdale, Florida, February 18-20, 1991.

Bahl, S.R., W.J. Azzam, and J.A. del Alamo. "Orientation Dependence of Mismatched $In_xAl_{1-x}As/In_{0.53}Ga_{0.47}As$ HFETs." *J. Crystal Growth* 111(1-4): 479-483 (1991).

Bahl, S.R., W.J. Azzam, and J.A. del Alamo. "Strained-Insulator $In_xAl_{1-x}As/n^+-In_{0.53}Ga_{0.47}As$ Heterostructure Field-Effect Transistors." *IEEE Trans. Electron Dev.* 38(9): 1986-1992 (1991).

Bahl, S.R., and J.A. del Alamo. "Elimination of Mesa-Sidewall Gate Leakage in InAlAs/InGaAs HFETs by Selective Sidewall Recessing." *Proceedings of the 18th International Symposium on Gallium Arsenide and Related Compounds*, Seattle, Washington, September 9-12, 1991.

Chapter 3. Novel Superconducting Tunneling Structures

Academic and Research Staff

Professor John M. Graybeal, Professor Henry I. Smith

Visiting Scientists and Research Affiliates

Dr. Bernard S. Meyerson¹

Graduate Students

George E. Rittenhouse

3.1 Project Description

Sponsor

Joint Services Electronics Program

Contract DAAL03-89-C-0001

Contract DAAL03-92-C-0001

Project Staff

Professor John M. Graybeal, Professor Henry I. Smith, Dr. Bernard S. Meyerson, George E. Rittenhouse

In this program we seek to examine the superconducting Josephson behavior in short-channel electronic structures where interference effects can take place. Additionally, our hybrid superconducting-semiconducting structure represents the first attempt at Josephson coupling via resonant tunneling. A significant consequence of this approach is that the energy scale for modulating the Josephson coupling is set by the quantum confinement levels and not the intrinsic semiconducting gap voltage.

Our device uses a thin vertical Si membrane ($< 1000\text{\AA}$) as a degenerate semi-conducting weak link between the superconducting source and drain electrodes which lie on either side. This structure is in many ways an electrical analogue of a Fabry-Perot interferometer. The membrane defines a vertical quantum well in which the charge carriers can interfere with each other (either constructively or destructively), thus creating a resonant tunneling structure between the source

and drain for both the Cooper pairs (i.e., the Josephson channel) and the normal quasiparticle (i.e., electron) channel. A separately applied gate voltage biases the levels within the semiconducting well, and ideally will modulate the Josephson current by varying the wavelength of the tunneling particles. Previous efforts on such hybrid Josephson devices have not utilized either resonant tunneling or quantum confinement, and their lack of gain arises from the significant mismatch between the semiconducting and superconducting gap energy scales.² A key motivation for our devices is that the energy scale is set by quantum confinement, and can be tuned separately from either of the gap energies. For Si well widths in the range of 500-1000Å, the energy levels separation in the well can be more comparable to the superconducting gap energy, i.e., many times smaller than the semiconducting gap.

Recent progress has now validated our basic device geometry in uniformly doped low-mobility Si:P. We are now progressing to fabricate the devices on doped high-mobility epitaxial layers grown on Si wafers at IBM. Higher mobilities will increase the characteristic lengths for the carriers in the semiconducting well, thereby better enabling internal interferences.

A schematic of the device geometry is shown in figure 1. More details of the fabrication process and progress will be published elsewhere.³ The primary aspects of the fabrication are described here. The originating wafer is $< 110 >$ Si, phosphorous-doped via ion implantation to yield

¹ IBM Corporation, Thomas J. Watson Research Center, Yorktown Heights, New York.

² A.W. Kleinsasser, T.N. Jackson, G.D. Pettit, H. Schmid, J.M. Woodall, and D.P. Kern, *IEEE Trans. Mag.* MAG-25(2): 1274 (1989), and references within.

³ K. Early, G.E. Rittenhouse, J.M. Graybeal, and Henry I. Smith, "Sub-100 and sub 10-nm-thick Membranes Aniso-

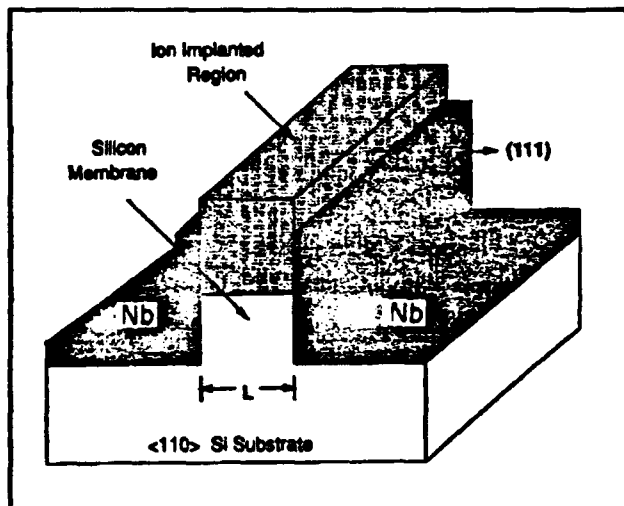


Figure 1. Schematic of the planar device structure. The vertical membrane consists of two etch pits separated by a length $L \leq 1000\text{\AA}$. The typical height for the vertical membrane is $\approx 3000\text{\AA}$.

$1 \times 10^{19} \text{ cm}^{-3}$ carriers at low temperature. A 300\AA Si_3N_4 layer is used as an etchant mask, with the membrane defined by aligning a mask stripe along either the $[1\bar{1}2]$ or $[11\bar{2}]$ crystalline axis. The membrane fabrication is done via wet etching, using a potassium hydroxide/isopropyl alcohol solution which is well known for its highly anisotropic etching of Si. Because of the wafers' crystallographic orientation, the resultant terminating (111) planes are perpendicular to the wafer surface and form the walls of the vertical membrane structure. Such processing yields atomically-smooth surfaces which possess a significantly higher degree of parallelism and a significantly lower surface defect density than could be obtained by reactive-ion-etching (RIE) or other energetic processes. The niobium counterelectrodes are subsequently deposited, and source-

drain isolation is obtained by planarization followed by a chlorine RIE etch.

The electrical results of such devices fall into two categories. Those with wall thicknesses (denoted L in figure 1) greater than roughly 1000\AA displayed no Josephson currents, and showed current-voltage (I - V) characteristics consistent with superconducting-insulator-normal (SIN) metal behavior. The thin "insulating" layer is presumably a Schottky barrier at the Nb/Si interface, whereas the lack of a Josephson current reflects the fact that the device thickness L is significantly greater than the proximity-induced superconducting coherence length ξ_N in the Si ($\xi_N \approx 65\text{-}100\text{\AA}$ at 4.2K for these low-mobility devices). However, devices with membrane thicknesses comparable to 600\AA displayed finite Josephson currents, and fine I - V behavior consistent with SNS behavior. The I - V s are shown as a function of temperature for one device in figure 2. The product of the critical current and the high-bias device resistance $I_c R_n$ was as high as 0.4 meV at low temperatures, consistent with the best previous results on Nb/Si/Nb devices. Careful examination of the device characteristics plus imaging with a high-resolution STEM ruled out the existence of any Nb shorts over the top of the membrane. Additionally, modulation of the critical current versus applied magnetic flux was entirely consistent with the device geometry.

The next step for this work is to fabricate these devices using high-mobility Si. Note that conventional uniformly doped Si cannot provide the necessary characteristic lengths as its mobility is too low. Therefore, we are turning to chemical-vapor deposited epitaxial layers of Si/Si:B grown on (110) oriented wafers which can have mobilities approaching $10^4 \text{ cm}^2/\text{V}\cdot\text{sec}$. This work is presently underway.

tropically Etched in (110) Silicon," submitted for publication; G.E. Rittenhouse, Henry I. Smith, and J.M. Graybeal, "A Silicon Weak-Link Josephson Junction Using a Vertical Membrane Structure," forthcoming.

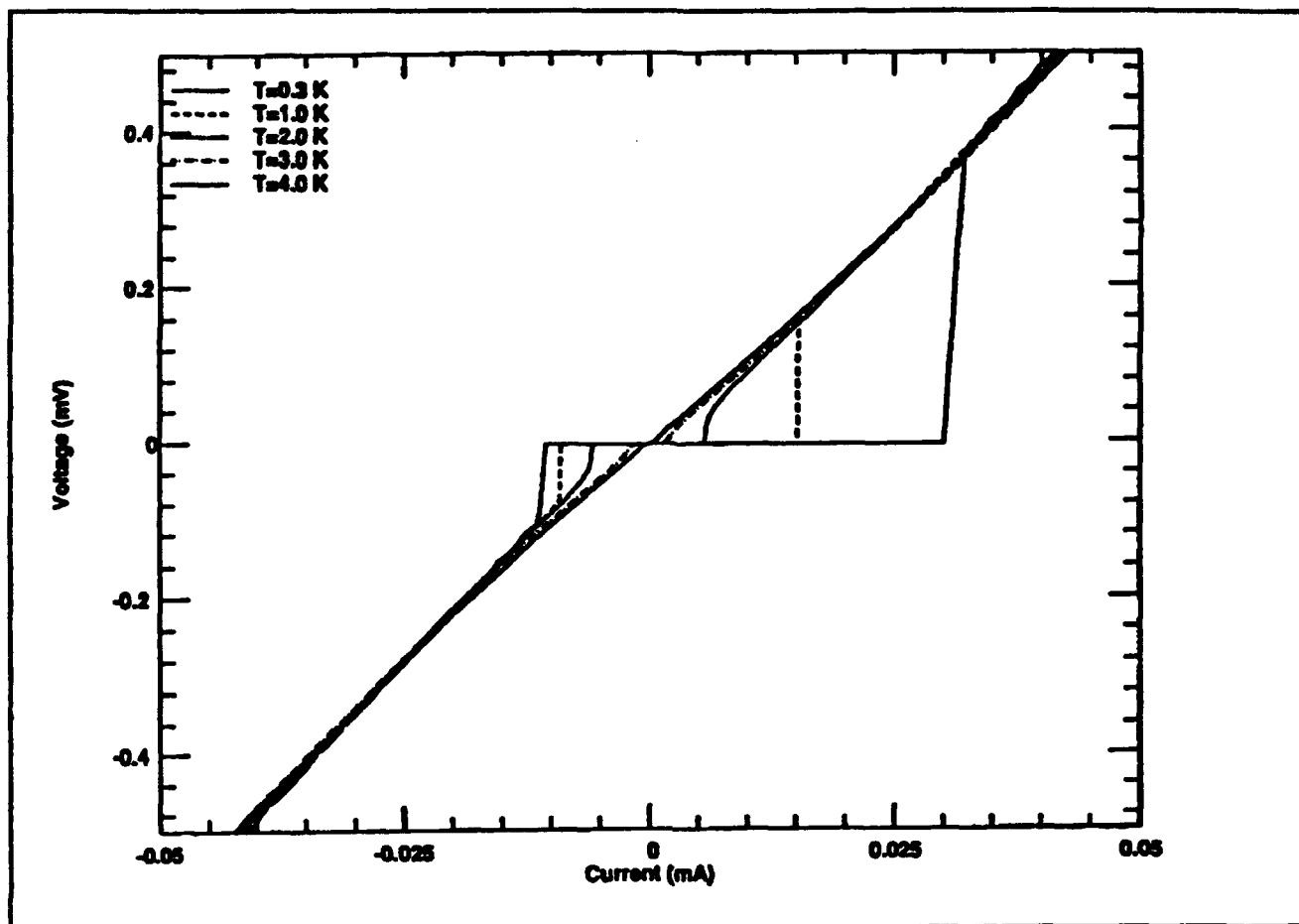


Figure 2. Current-voltage characteristics of one device versus temperature. Note presence of a finite Josephson current.



Professor Leslie A. Kolodziejski

Chapter 4. Chemical Beam Epitaxy of Compound Semiconductors

Academic and Research Staff

Professor Leslie A. Kolodziejski

Visiting Scientists and Research Affiliates

Dr. Carmen Huber¹

Graduate Students

Ziad Azzam, Christopher A. Coronado, Jay N. Damask, Easen Ho

Undergraduate Students

George C. Chen, Sang H. Park, Chung-Hao Shue, Ayca Yuksel

Technical and Support Staff

Kelley S. Donovan, David S. Lee, Angela R. Odoardi

4.1 Facility for the Gas Source Epitaxy of Compound Semiconductors

Sponsors

3M Company Faculty Development Grant
AT&T Research Foundation
Special Purpose Grant
Charles S. Draper Laboratories
Contract DL-H-418484
Defense Advanced Research Projects Agency
Subcontract 216-25013 and 542383
Joint Services Electronics Program
Contract DAAL03-89-C-0001
Contract DAAL03-92-C-0001
National Science Foundation
Grant ECS 88-46919
Grant ECS 89-05909

The new laboratory for the growth of both II-VI and III-V compound semiconductor heterostructures, using gas source epitaxy techniques, has received all hardware necessary to complete the multichamber system. The epitaxy system consists of six interconnected ultrahigh vacuum chambers: two introduction chambers, a transfer chamber, a II-VI-dedicated reactor, a III-V-dedicated reactor, and an analytical/metalization chamber. The analytical/metalization chamber is now attached to the transfer chamber; figure 1 shows a photograph

of the new chamber. In situ analytical tools which are available include Auger electron spectroscopy, reflection high energy electron diffraction (RHEED), additional ports for laser illumination of the sample, and a three-source electron beam evaporator for metals. The ultrahigh vacuum interconnection to both of the growth systems allows surface analysis of the many II-VI, III-V, and II-VI/III-V heterostructures which are envisioned, immediately following fabrication, without concern of contamination from atmospheric gases. The analysis chamber is expected to provide additional insight into the effect of both electron and photon beams on the surface of films grown using metalorganic molecular beam epitaxy. Metal evaporators will enable us to probe the initial stages of ohmic contact formation specifically with regard to the difficulties experienced in forming an ohmic contact to p-type ZnSe. The presence or absence of mixed interfacial layers in multilayered II-VI/III-V heterostructures may also be detected (in some instances) in the analytical chamber.

The final addition was the connection of a gas source molecular beam epitaxy (GSMBE) reactor to a small buffer chamber attached to the transfer chamber. The new reactor, shown in figure 2, was purchased from Instruments S.A., Riber Division, and is now in the final stages of installation. The gas source reactor has solid elemental sources of Ga, In, Al, Si, and Be, and gaseous hydride sources of arsenic and phosphorus. The purpose

¹ Physics Department, University of Puerto Rico, Rio Piedras, Puerto Rico.

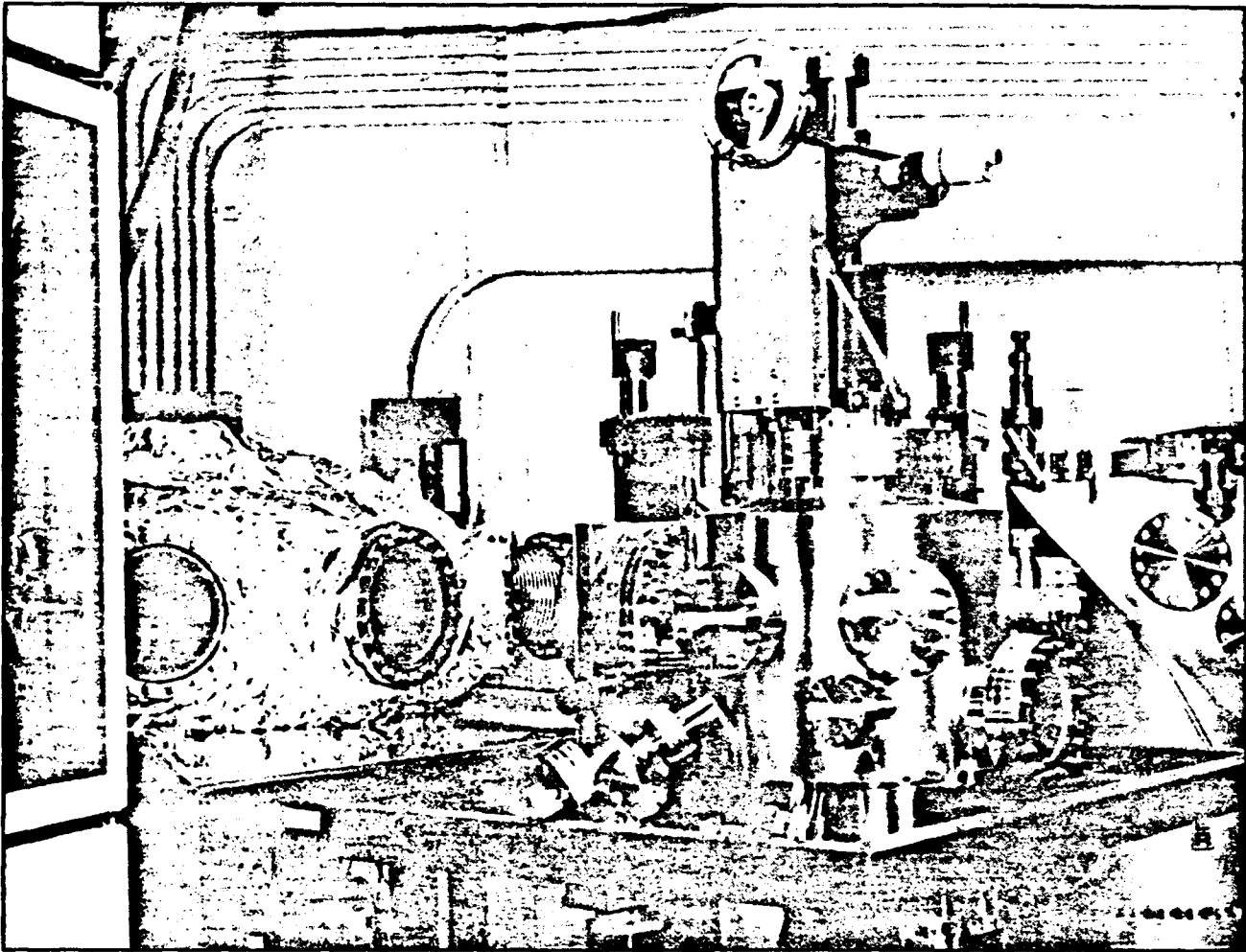


Figure 1. Photograph of the analytical/metalization chamber. Connection to the ultrahigh vacuum transfer chamber is yet to be completed.

of the III-V chamber is two-fold: (1) layers containing P and As will be crucial for utilizing lattice-matched buffer layers for the II-VI-based quantum well structures which are under investigation, and (2) III-V-based optical and electronic devices will be explored including quantum-effect electronic devices (in collaboration with Professors Dimitri A. Antoniadis and Henry I. Smith), and channel dropping filters and waveguide structures (in collaboration with Professor Hermann A. Haus). In addition, the III-V chamber will be employed for fabrication of II-VI/III-V multilayered heterostructures which contain III-V layers having substantial thickness. The II-VI reactor, which has gaseous sources for In, Ga, and As, will only be used for the growth of very thin III-V layers on the order of hundreds of angstroms or less.

4.2 Metalorganic Molecular Beam Epitaxy (MOMBE) of ZnSe

Sponsors

Charles S. Draper Laboratories
Contract DL-H-418484
Defense Advanced Research Projects Agency
Subcontract 542383 and 5300716-07
Joint Services Electronics Program
Contract DAAL03-89-C-0001
Contract DAAL03-92-C-0001
National Science Foundation
Grant ECS 88-46919
U.S. Navy - Office of Naval Research
Contract N00014-88-K-0564

Optical sources operating in the blue portion of the visible light spectrum have many potential commercial and military applications in, for example, optical information storage systems,

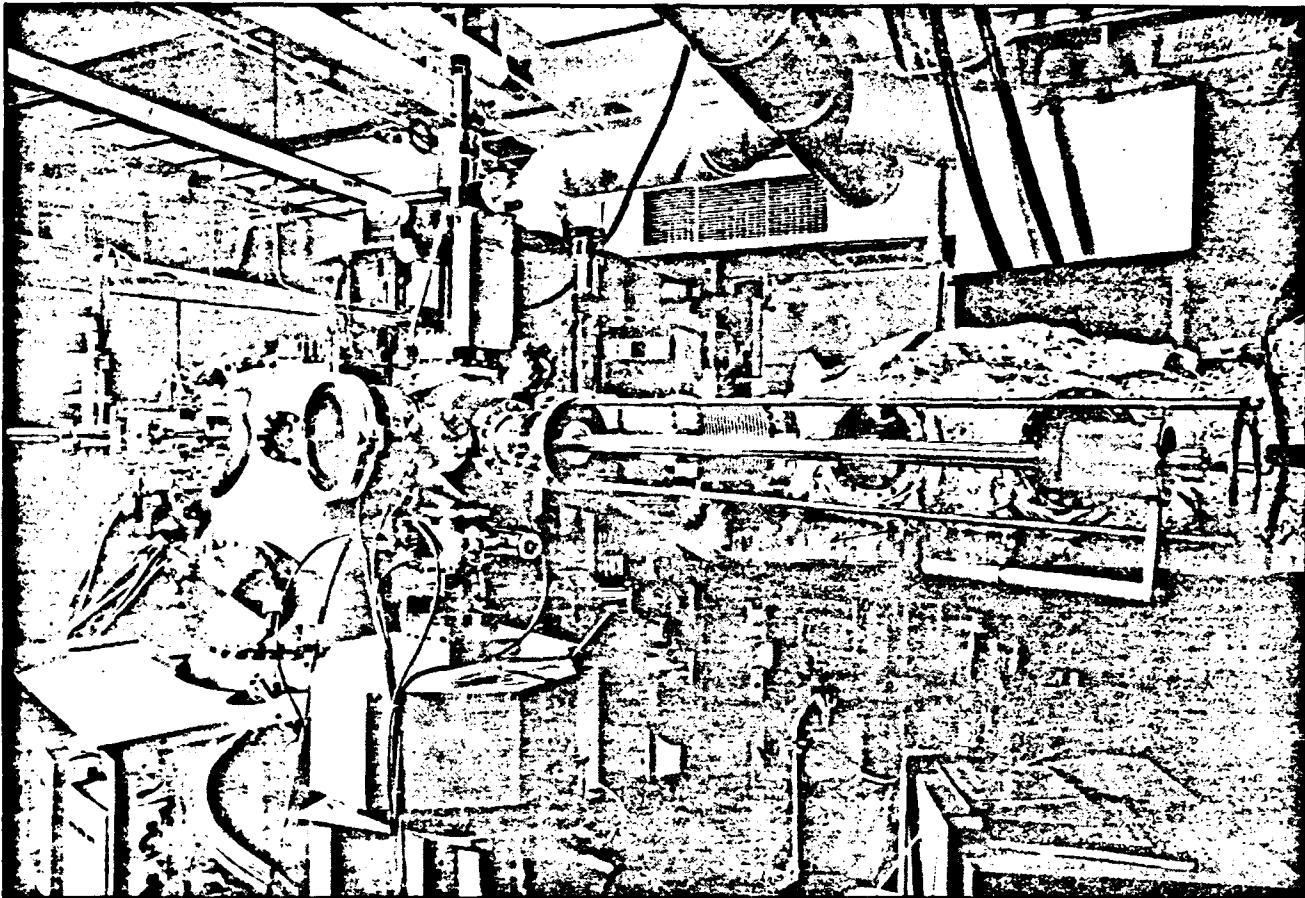


Figure 2. Photograph of the new III-V-dedicated GSMBE (which is attached to the small loadlock/buffer chamber). Final connection to the hemispherical ultrahigh vacuum transfer chamber can be seen.

medical imaging systems, electroluminescent flat panel displays, and color laser printers.

Although there are a variety of material systems, such as SiC, frequency doubled III-V-based lasers, and GaN, which can potentially offer a source of blue light, each of these systems has some limitations relative to integration and/or fabrication. The II-VI family of semiconductors (specifically the Zn chalcogenides) offers a solution to the problem of integration, and impressive recent gains have been achieved in fabrication technology. II-VI-based quantum well structures exhibiting excellent crystal quality are routinely fabricated on technologically important III-V substrates, suggesting that future integration needs will be straightforward. However, some substantial problems still remain to be solved.

In order to meet the requirements for room temperature, blue optical sources, the II-VI materials will require greater concentrations of sulfur to increase the bandgap. However, the alloying of ZnSe with sulfur results in a contraction of the lattice parameter and, therefore, an increase in the lattice mismatch with binary compounds such as GaAs. This problem is eliminated by utilizing lattice-matched

alloy buffer layers such as InGaP and GaAsP. The attached III-V gas source molecular beam epitaxy reactor will be the source of any III-V-based lattice-matched buffer layer. Although the lattice mismatch difficulty is circumvented here, we are also fabricating "epilayer-on-epilayer" structures. These epilayer-on-epilayer structures are necessary to provide the minimum possible number of defects created at the heterovalent interface and ultimately within the active region of the II-VI optical device. In addition, a key advantage offered by gas source epitaxy techniques is the ability to control, via mass flow controllers, the flux of species which exhibit very high vapor pressures as a function of temperature. Sulfur and phosphorus containing materials are excellent candidates for fabrication utilizing gas source epitaxy techniques with impressive successes reported.

The objectives of the research described here revolve around the growth of various II-VI-based heterostructures using gaseous source epitaxy including metalorganic molecular beam epitaxy (MOMBE), chemical beam epitaxy (CBE), and gas source molecular beam epitaxy (GSMBE). The various techniques utilize combinations of gaseous

sources such as metalorganics and hydrides, as well as solid elemental sources. Thus far we have explored the MOMBE of ZnSe using diethylzinc and diethylselenium.

A large number of films have been grown with the details of the growth parameters described below. ZnSe epilayers were normally grown on carbon-controlled semi-insulating (001) GaAs wafers, although n-type, p-type and 2°-off n-type GaAs were also used. Typical growth temperatures ranged from 250°C to 425°C, with the majority of the film growths performed near 320°C. The VI/II flow ratio was varied from 0.2 to 5.0, with diethylzinc (DEZn) and diethylselenium (DESe) gas flows ranging from 0.5 to 2.5 sccm. Reactor pressure during growth was typically 1×10^{-4} Torr. In nearly all cases the DEZn cracker was set at 50°C, and the DESe was thermally decomposed at 800°C. Cracking experiments with the quadrupole mass spectrometer (QMS) indicated that DESe decomposed at 800°C, while DEZn thermally dissociated at temperatures above 300°C.

Preliminary microstructural and optical characterization of the ZnSe suggests that the thin films are of good quality. A typical RHEED pattern observed following growth shows the presence of narrow streaks and readily apparent Kikuchi bands suggesting the existence of single crystalline films with smooth surface morphology. Secondary ion mass spectroscopy (SIMS) results indicate very low levels of carbon incorporation which is near the detectability limit of our instrument (VG-Fisons Instruments Model IX70S SIMSLAB). X-ray diffraction rocking curve analysis confirms the pseudomorphic nature of thin 1000Å films of ZnSe on GaAs. Typical full width at half maximum measurements for the (400) reflection is around 220 arc seconds. Optical characterization from photoluminescence measurements indicates the presence of bandedge excitonic features which are shifted to higher energy reflecting the presence of strain, in addition to features originating from deep level defects. We speculate that the presence of these particular deep level features is due to stoichiometry such as Zn vacancies, and we are therefore investigating growth with various flux ratios.

The growth rate using DEZn and DESe has continued to be very low. Although the actual species at the surface front are not known, we expect to find ethyl species of Zn and Se, in addition to dimers of Se from the thermal decomposition of the metalorganic. The growth temperatures inves-

tigated and the cracking data suggest that there is sufficient thermal energy to decompose the Zn molecules. (The RHEED patterns exhibit reconstructions of a Zn-stabilized surface.) In addition, the nearly constant growth rate observed for a wide variety of growth conditions (flow ratio and rate, substrate temperature, and with and without hydrogen) suggests that the growth is surface kinetics limited. Similar to metalorganic vapor phase epitaxy (MOVPE), although lacking the gas phase reactions, the MOMBE growth technique is expected to exhibit complex surface chemical reactions. We speculate that at the necessary low growth temperatures employed here, lattice sites for incorporation of Zn and Se are being blocked by alkyl radicals. The alkyl radicals are a copious byproduct of the surface pyrolysis of DEZn and thermal decomposition of the DESe. At higher growth temperatures ($\geq 425^\circ\text{C}$), where one might expect the alkyl radicals to desorb, competing desorption of Zn and Se limits the growth rate. Previous work² reported using these metalorganic sources show growth rates approximately an order of magnitude greater under similar growth conditions. Differences which may exist include (1) pressure during growth, (2) use of hydrogen carrier gas, or (3) the actual design of the gas crackers.

4.3 Photo-Assisted MOMBE of Wide Bandgap II-VI Compound Semiconductors

Sponsors

Defense Advanced Research Projects Agency
Subcontract 530-0716-07
Joint Services Electronics Program
Contract DAAL03-89-C-0001
Contract DAAL03-92-C-0001
National Science Foundation
Subcontract DMR 90-07890

Photo-assisted heteroepitaxial growth of ZnSe on GaAs by MOMBE is currently under intense investigation. MOMBE has several potential advantages when compared to other epitaxial growth techniques such as metalorganic vapor phase epitaxy (MOVPE) and molecular beam epitaxy (MBE). The advantages include: (1) The flux ratio of gaseous metalorganics can be precisely controlled using mass flow controllers; (2) in-situ analysis techniques such as reflection high-energy electron diffraction (RHEED) and quadrupole mass

² H. Ando, A. Taike, R. Kimura, M. Konagai, and K. Takahashi, "Metalorganic Molecular Beam Epitaxial Growth of ZnSe Using Diethylzinc and Diethylselenide," *Japanese J. Appl. Phys.* 25(4): L279-L281 (1986).

spectroscopy (QMS) are available; and (3) surface chemistry allows for fine tuning of the growth conditions. Photo-assisted MOMBE adds an extra degree of versatility because both selective deposition of material and modification of the surface chemistry are possible.

Photo-assisted growth was performed by selectively illuminating a portion of the wafer's surface. Radiation from a 5 Watt Ar ion laser (Spectra-Physics, Model 2025) was introduced at a 45° angle to the substrate normal. The laser spot on the wafer was typically an ellipse with major and minor axes of 1.4 and 1.0 cm. The effect of wavelength on growth has been studied by using laser radiation ranging from 780 nm to 350 nm. To produce the 780 nm line, a Ti:sapphire crystal was pumped with all lines of the argon ion laser. The power density was kept low at approximately 180 mW/cm², thus allowing thermal heating effects to be neglected.

As mentioned in Section 4.2, under the growth conditions described here, the growth rate during MOMBE of ZnSe has consistently remained very low. The growth rate without laser illumination is typically 250 to 375 Å/hour. As a function of calibrated growth temperature, the unilluminated growth rate shows a remarkable temperature insensitivity over the temperature range of 250-425°C. This is quite unexpected since MOMBE has typically demonstrated a strong temperature dependence.³ Laser illumination, however, has been found to ameliorate the low growth rate. For the portion of the film grown with photo-assistance, a significant temperature dependence is observed which is more typical of MOMBE growth.

Figure 3 shows the ratio of illuminated to unilluminated growth rates (enhancement ratio) as a function of laser wavelength. At a growth temperature of 320°C the bandgap energy of ZnSe corresponds to a photon energy of ~520 nm.⁴ The 780 nm radiation was found to produce no growth rate enhancement, while the higher energy photons produced significant growth rate enhancement. Furthermore, the growth rate enhancement was found to be directly proportional to the laser intensity (see insert of figure 3). When the TEM₀₀ mode of the argon ion laser was used, the

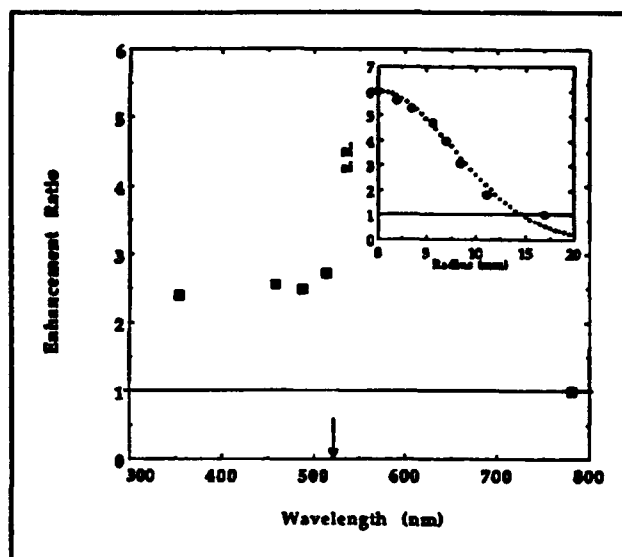


Figure 3. Growth rate enhancement ratio (ER) as a function of laser wavelength. The DESe and DEZn flow rates are both 0.5 sccm, and the substrate temperature is ~320°C (arrow indicates ZnSe bandgap). The insert shows the growth rate enhancement ratio of the illuminated region (457.9 nm laser line) as a function of spot radius (mm). The dotted curve is a Gaussian fit to the data suggesting a direct correlation between growth rate enhancement and power density.

enhancement ratio (solid circles) across the illuminated growth region was found to correlate well with the Gaussian intensity profile of the laser. The largest enhancement in the growth rate has been a factor of 9, although we have not yet attempted to optimize the various growth parameters to maximize the growth rate.

Thus far our data suggest that the creation of electron/hole pairs are required for the growth rate to be enhanced during photo-assisted growth. Photons having energies above the bandgap of ZnSe (at the growth temperature) resulted in growth rate enhancement, while photons with longer wavelengths do not increase the growth rate. Similar dependencies have been observed by Yoshikawa et al⁴ for growth of ZnSe by photo-assisted MOVPE. For the metalorganic molecules utilized here, gas phase absorption⁵ is expected to occur at wavelengths much shorter (248 nm for DEZn) than investigated here. Although a more

³ H. Ando, A. Taïke, R. Kimura, M. Konagai, and K. Takahashi, "Metalorganic Molecular Beam Epitaxial Growth of ZnSe Using Diethylzinc and Diethylselenide," *Japanese J. Appl. Phys.* 25(4): L279-L281 (1986).

⁴ A. Yoshikawa, T. Okamoto, T. Fujimoto, K. Onoue, S. Yamaga, and H. Kasai, "Ar-Ion Laser-Assisted MOVPE of ZnSe Using DMZn and DMS₂ as Reactants," *Japanese J. Appl. Phys.* 29(2): L225-L228 (1990).

⁵ H. Hou, Z. Zhang, U. Ray, and M. Vernon, "A Crossed-Laser Beam Study of the Photodissociation Dynamics of Zn(C₂H₅)₂ and (Zn(C₂H₅)₂)₂ at 248 nm and 193 nm," *J. Chem. Phys.* 92(3): 1728-1746 (1990).

detailed investigation is required, we speculate that a potential mechanism is that a photo-generated carrier (we suspect holes) eliminates an ethyl-metal bond at the surface leading to a higher growth rate. Preliminary data (not shown here) provide evidence that there is a dependence of the growth rate enhancement on the gas flow ratio; this suggests that the growth rate enhancement is not due to liberation of surface alkyls which are blocking lattice sites by photo-generated carriers. The photo-assisted growth experiments currently underway are expected to aid our understanding of the dominant surface chemistry and growth mechanisms. By adjusting conditions such that growth

will only occur in regions irradiated by the laser, selective area epitaxy of ZnSe will be possible.

4.4 Publications

Coronado, C.A., E. Ho, L.A. Kolodziejski, and C.A. Huber. "Photo-Assisted Molecular Beam Epitaxy of ZnSe." Submitted to *Appl. Phys. Lett.*

Kolodziejski, L.A. "Chemical Beam Epitaxy of II-VI Semiconductors." Invited paper presented at the American Vacuum Society Meeting, Seattle, Washington, November, 1991.

Chapter 5. Microstructural Evolution in Thin Films of Electronic Materials

Academic and Research Staff

Professor Carl V. Thompson, Dr. Craig Ballentine, Dr. Paul D. Bristowe, Dr. En Ma,¹ Dr. John Melngailis, Dr. Robert C. O'Handley

Visiting Scientists and Research Affiliates

Dr. Sergei Bogomolov,² Dr. Harold J. Frost,³ Hideo Miura,⁴ Takauki Uda,⁴ Dr. A. Wagner,⁵ Derek T. Walton⁶

Graduate Students

Roland Carel, Steven S. Cooperman, Anthony D. Della Ratta, Andrew D. Dubner, Jerrold A. Floro, Heather E. Inglefield, Young-Chang Joo, Harold Kahn, Brett D. Knowlton, Ya-Chin Liu, Hai P. Longworth, Jaesang Ro

Technical and Support Staff

Peter C. Heron

5.1 Electromigration and Microstructure

Electric-current-induced atomic self-diffusion, or electromigration, causes open and short circuit interconnect failures in integrated circuits. Electromigration occurs primarily by diffusion along grain boundaries, and interconnect failure initiates at grain boundaries, so that interconnect reliability is strongly dependent on the grain sizes and orientations in polycrystalline interconnects. The relationships between these microstructural characteristics and interconnect reliability have become more complex as interconnect dimensions (widths and thicknesses) have become comparable to grain sizes. We have studied the effects of microstructure on the reliability of submicron and larger interconnects as well as vias and contacts. We have done this by using a variety of techniques for controlling grain sizes and grain size distributions in thin films. We are also developing models for microstructural evolution in order to develop accu-

rate models for electromigration in submicron interconnects.

5.1.1 Control of Microstructures in Aluminum Films

Sponsor

Joint Services Electronics Program
Contract DAAL03-89-C-0001

Project Staff

Hai P. Longworth, Professor Carl V. Thompson

In previous years, we reported the use of precipitate-induced abnormal grain growth to produce grains as large as 1 mm in 1 μ m thick films. In the past year, we completed an extensive study in which we have established the requirements for precipitate-induced abnormal grain growth in thin films and have demonstrated similar

¹ Presently at the University of Michigan, Ann Arbor, Michigan.

² Ural Polytechnical Institute, Sverdlovsk, Russia.

³ Dartmouth College, Hanover, New Hampshire.

⁴ Hitachi Limited, Tokyo, Japan.

⁵ IBM Corporation, Yorktown Heights, New York.

⁶ Formerly of Dartmouth College, currently with Digital Equipment Corporation, Hudson, Massachusetts.

phenomena in Al-Cu-Cr, Al-Ag-Cr, Al-Mn-Cr, and Al-W alloys. We have found that to optimize the precipitate-induced abnormal grain growth process, the alloy additions should initially be present as pure layers in the middle of the Al film. In alloys containing Cr, the Cr serves to aid in the nucleation of precipitates, leading to localization of the precipitates in the middle of the film, and leading to a larger number of smaller, more closely spaced precipitates. Through controlled abnormal grain growth, the microstructure of thin films can be controllably varied over broad ranges.

5.1.2 Reliability of Vias

Sponsor

Semiconductor Research Corporation

Project Staff

Harold Kahn, Professor Carl V. Thompson

Over the past year, we have developed a via test structure that allows statistical characterization of via reliability by stressing multiple vias in *parallel*. We have used this process to characterize the reliability of vias with W plugs and have shown that under normal test conditions, joule heating of the plugs contributes to accelerated open failures of Al interconnects. We are developing simple thermal models to evaluate the effect of joule heating at service conditions. We have also demonstrated that the grain size in the Al interconnect greatly affects via reliabilities and also the statistics of failure. Large grains lead to bimodal failure distributions. We are developing tools for statistical analysis of via reliability.

5.1.3 Modeling of Microstructures in Interconnects

Sponsors

Semiconductor Research Corporation
National Science Foundation

Project Staff

Derek T. Walton, Dr. Harold J. Frost, Professor Carl V. Thompson

Over the years, we have developed and tested models for crystal nucleation and growth to form continuous polycrystalline films. We have also modeled grain growth in continuous polycrystalline films. In the past year we have modified these models to investigate the evolution of the microstructures of polycrystalline interconnects to "bamboo" structures, as illustrated in figure 1. We find that the approach to a fully bamboo structure is exponential in time and that the rate of transformation is inversely proportional to the square of the strip width. When the simulation is extended to model grain boundary pinning due to grooving at grain boundary-free surface intersections, we find that there exists a maximum strip width-to-thickness ratio (approximately 3) beyond which the transformation to the bamboo structure does not proceed to completion. In earlier work, we have shown that reliability of nearly-bamboo and fully-bamboo lines is greatly different. Our modeling work is now allowing us to identify the conditions under which it is reasonable to expect to obtain only fully-bamboo lines.

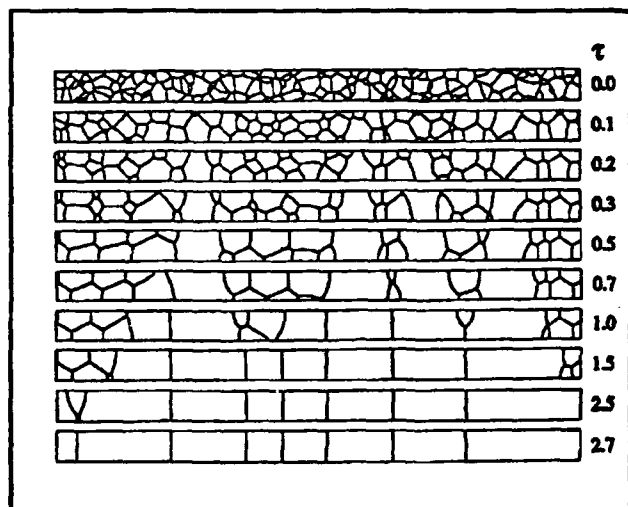


Figure 1. Evolution of the grain structure within a strip. The transformation to a "bamboo" structure is dominated by the growth of bamboo sections into regions of grain clusters. The rate of this transformation depends strongly on the strip width.

5.1.4 Electromigration in Bicrystals

Sponsors

Joint Services Electronics Program
Contract DAAL03-89-C-0001
Semiconductor Research Corporation

Project Staff

Hai P. Longworth, Young-Chang Joo, Brett D. Knowlton, Professor Carl V. Thompson

In previous work we have shown that individual grain boundaries greatly affect the reliability of an interconnect line. In order to understand the reliability of interconnects, it is therefore important to understand the reliability of individual grain boundaries. To do this we have developed a new technique that allows us to characterize the reliability of populations of lines with single, identical grain boundaries with controlled types, locations, and orientations. The technique is schematically shown in figure 2. We start by making NaCl bicrystals of the desired type, on which we grow epitaxial bicrystal Al films which are transferred and sintered to oxidized silicon wafers. We then use conventional lithographic techniques to pattern multiline test structures with the same controlled Al grain boundary running through all the lines. We can then investigate, as an example, the effect of the boundary orientation on the reliability of the line, as illustrated in figure 3.

We have shown that (1) failure times of lines containing single identical boundaries are lognormally distributed, (2) the medium time to failure depends more strongly on the boundary orientations than the types of grain boundaries, (3) the deviation in the time to failure has a large component not dependent on microstructure, and (4) both interfacial diffusion and grain boundary diffusion appear to contribute to failure in bicrystal lines and probably in bamboo and near-bamboo lines as well.

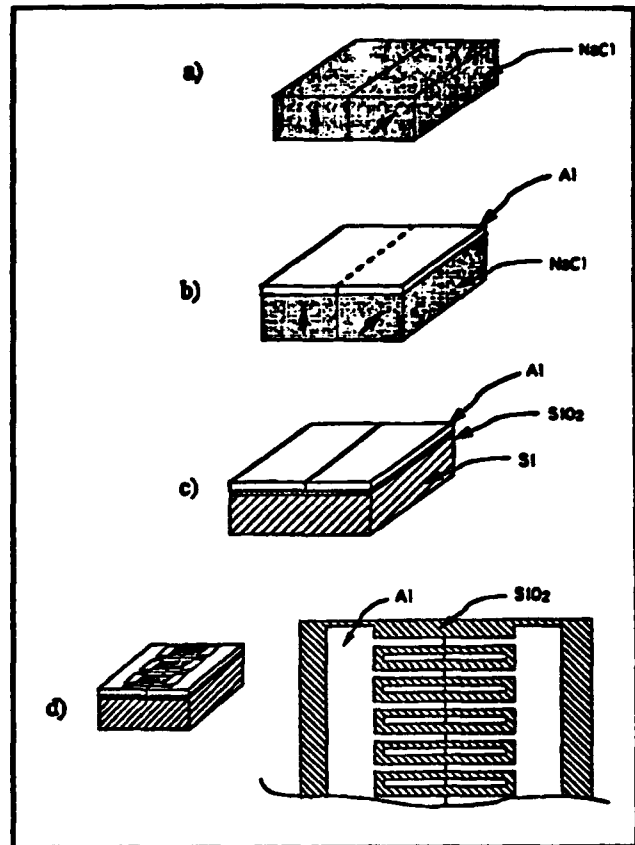


Figure 2. The fabrication process of bicrystal test patterns. (a) NaCl bicrystal substrate made from two NaCl single crystals; (b) Al bicrystal thin film epitaxially deposited on the NaCl substrate; (c) Al film transferred to an oxidized Si wafer; and (d) patterning.

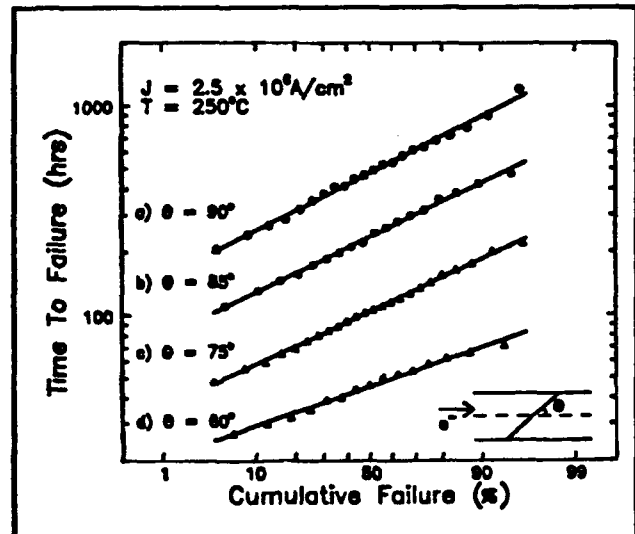


Figure 3. Failure distributions of $\Sigma 13[100]$ bicrystal lines as a function of θ , the angle between the current direction and the grain boundary plane.

Chapter 1. Statistical Mechanics of Quantum Dots

Academic and Research Staff

Professor Boris L. Altshuler, Dr. Richard Berkovits, Dr. Aaron Szafer

Graduate Students

Michael Faas

Technical and Support Staff

Imadiel Ariel

1.1 Project Description

Sponsor

Joint Services Electronics Program
Contract DAAL03-92-C-0001

We are investigating equilibrium properties of quantum dots (isolated metallic systems with sizes smaller than the typical length of an electron dephasing). Until recently, we concentrated on such properties of an individual dot as capacitance and electric and magnetic susceptibility. The most dramatic manifestation of the quantum nature of the magnetic polarizability takes place for a multiply connected geometry, e.g., for a ring, and is known as a persistent current. This current is a metallic system response to the magnetic flux through the hole. It can exist even when there is no field in the material, and it does not dissipate.

Due to the impurity or surface scattering of the conductivity electrons, there is certain dispersion of the properties in the ensemble of macroscopically equivalent samples. Therefore, we must consider the sample to sample (mesoscopic) fluctuations as well as ensemble averaged properties such as persistent current.

Earlier¹ we developed a theory on the persistent current neglecting the interaction between the electrons. This problem involves two energy scales: (1) the mean energy spacing between the exact one electron states in a random potential Δ , and (2) the inverse typical time of an electron diffusion around the sample $\hbar/t = E_c$, also known as the Thouless shift. The dimensionless ratio E_c/Δ is

the sample conductance in natural units e^2/h . We found that the mean root square of the mesoscopic fluctuations of the persistent current is of the order of $E_c e/h$, while the averaged persistent current, although nonzero, is much smaller and determined by Δ .

The persistent current was recently observed² and found to be orders of magnitude larger than the theoretical predictions *in the absence of the interaction between electrons*. Also, superconductive-like fluctuations cannot explain why the effect is so large. On the other hand, the magnitude of the observed persistent current is more or less consistent with the charging energy e^2/R , where R is the radius of a ring. This was one of the motivations for us to study dielectric properties of mesoscopic systems.

We have developed a technique to investigate the local charge fluctuations and local electric fields within a mesoscopic system. We have found that, due to quantum interference, there are long range correlations in these local fluctuations (similar to the well-known Friedel oscillations). These correlations determine the additional energy caused by the Coulomb interaction between the fluctuations, and, therefore, their contribution to the thermodynamics.

We have calculated the distribution of electric fields outside a disordered, neutral quantum dot as well as the quantum correction to its polarizability. Although both of the effects are small, they are very important ideologically from the point of view of the scaling theory of metal-insulator transition, which we believe are observable.

¹ B.L. Altshuler, Y. Gefen, and Y. Imry, *Phys. Rev. Lett.* 66: 88 (1991); B.L. Altshuler and B.Z. Spivak, *Zh. Eksp. Teor.* 92: 607 (1987).

² L.P. Levy, G. Doland, J. Dunsmuir, and H. Bouchiat, *Phys. Rev. Lett.* 64: 2074 (1990); V. Chandrasekhar, R.A. Webb, M.Y. Brady, M.D. Ketchen, W.J. Gallagher, and A. Kleinsasser, *Phys. Rev. Lett.* 67: 3578 (1991).

These small effects are caused by the screening of the Coulomb interaction. Due to this screening, additional energy is determined only by the charge distribution in a layer near the sample surface of a width of the screening length. As a result, interaction between the charge fluctuations is not sufficient to account for the persistent current. On the other hand, there is another magnetic flux dependent contribution to the Coulomb energy: the interaction between the charge fluctuations and the confining potential in a quantum dot (e.g., a finite work function of a metallic grain is determined by a dipole layer on the surface). The energy of the local charge fluctuations in the field

of this layer apparently depends on the magnetic field and explains the observed persistent current. This interaction can have a number of important and observable consequences such as substantial mesoscopic fluctuations of the work function and its dependence on the external parameters such as low magnetic field.

Publications

Altshuler, B.L. "Thermodynamics of Mesoscopic Systems." Paper presented at the International Symposium on Nanostructures and Mesoscopic Systems, Santa Fe, New Mexico, May, 1991.

Chapter 2. Single Electron Transistors

Academic and Research Staff

Professor Marc A. Kastner, Professor Dimitri A. Antoniadis, Professor Henry I. Smith, Paul L. McEuen

Visiting Scientists and Research Affiliates

Shalom Wind¹

Graduate Students

Paul A. Belk, Ethan B. Foxman

2.1 Project Description

Sponsors

Joint Services Electronics Program

Contract DAAL03-89-C-0001

Contract DAAL03-92-C-0001

National Science Foundation

Grant ECS 88-13250

Several years ago, we discovered, completely unexpectedly, new behavior in very small Si MOSFETs. Whereas conventional transistors turn from the off state to the on state only once as the gate voltage increases, these small transistors turn on and off periodically, in some cases as many as one hundred times. We have since learned how to control the period of these oscillations in GaAs field effect devices and have shown that a nm-size transistor turns on and off once for every electron added to it. Because of this, we call such a device a Single Electron Transistor.

Having established that each cycle corresponds to the addition of one electron, the period in gate voltage provides a very precise measure of the capacitance of our devices. Because it is very small, $\sim 10^{-16}$ F, such transistors may eventually find application in ultra-sensitive charge detection. Furthermore, capacitive coupling may make possible arrays of single-electron transistors with unique properties. Unfortunately, the single electron behavior has only been observed, so far, below about 1 K. Whether this behavior can be

observed at higher temperatures in the future depends on the details of the mechanism that causes it. Our objective is, therefore, to better understand that mechanism.

Our initial discovery was made² with inversion layers in Si which were about 30 nm wide and several mm long. These were dual gate MOSFETs with a narrow slot, ~ 600 nm wide, in the lower gate, fashioned with X-ray lithography. This lower gate was made of refractory metals allowing a high temperature anneal after all unconventional lithography was complete. In the end, these devices were the narrowest transistors ever made, but whereas most previous narrow devices had low mobility, these had mobilities comparable to wide devices. The successful fabrication of these ultra-narrow devices was the result of a close collaboration between Professor Henry I. Smith, Professor Dimitri A. Antoniadis, and Professor Marc A. Kastner and their students.

Soon after these devices were first fabricated, it was discovered that their conductance oscillated periodically as a function of the density of electrons in the conducting channel, proportional to the gate voltage, V_g . To prove that the period of the oscillations corresponded to the addition of a single electron, new devices had to be made.

The first step was to produce devices close in their operation to a MOSFET but in GaAs where the influence of interface charges is much weaker.³ This was accomplished through a remarkably suc-

¹ IBM Thomas J. Watson Research Center, Yorktown Heights, New York.

² J.H.F. Scott-Thomas, S.B. Field, M.A. Kastner, H.I. Smith, and D.A. Antoniadis, "Conductance Oscillations Periodic in the Density of a One-Dimensional Electron Gas," *Phys. Rev. Lett.* 62: 583 (1989); S.B. Field, M.A. Kastner, U. Meirav, J.H.F. Scott-Thomas, D.A. Antoniadis, H.I. Smith, and S.J. Wind, "Conductance Oscillations Periodic in the Density of One-Dimensional Electron Gases," *Phys. Rev. B* 42: 3523 (1990).

³ U. Meirav, M.A. Kastner, M. Heiblum, and S.J. Wind, "One-Dimensional Electron Gas in GaAs: Periodic Conductance Oscillations as a Function of Density," *Phys. Rev. B (Rapid Comm.)* 40: 5871 (1989).

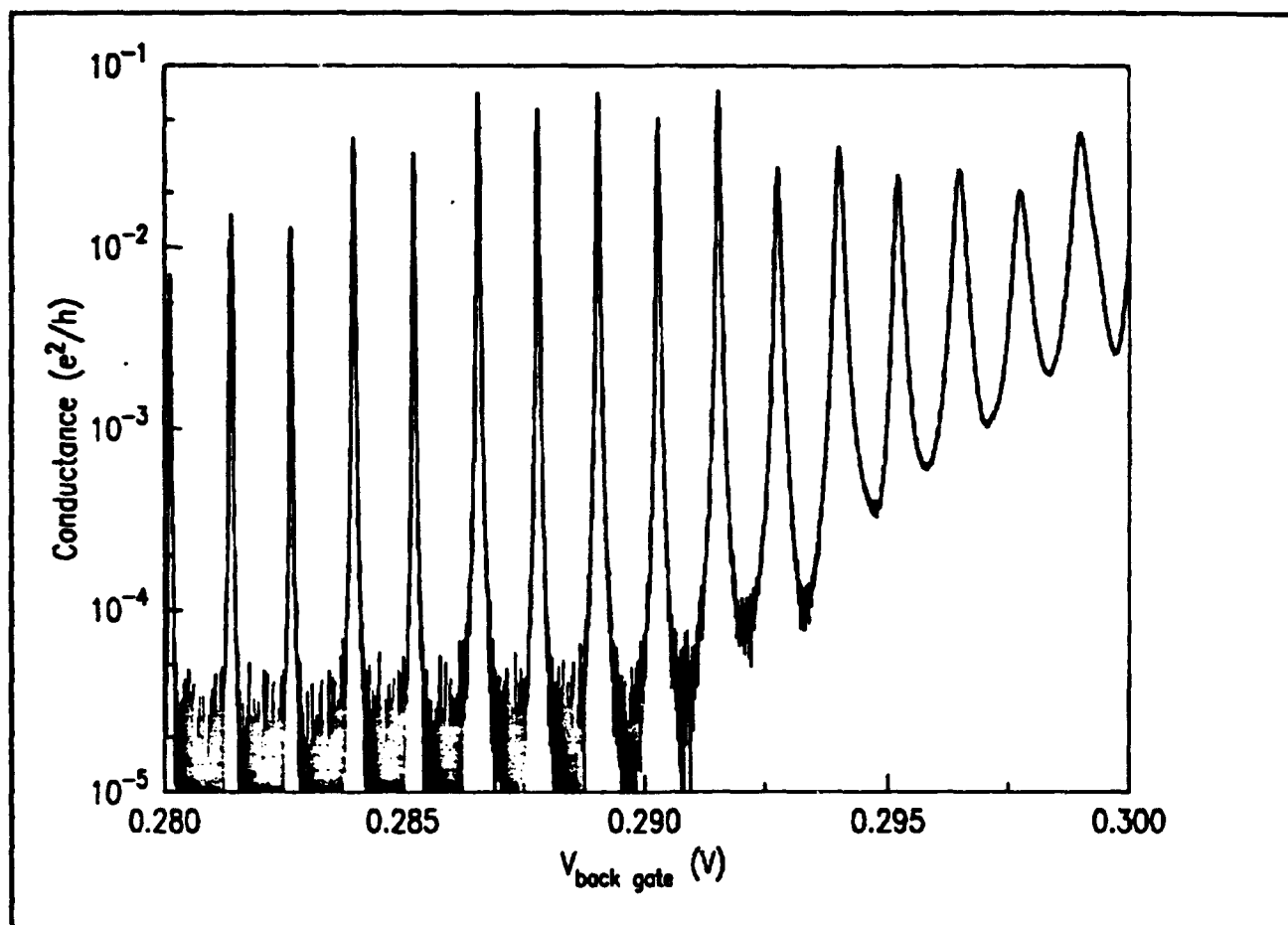


Figure 1. Conductance in units of the quantum of conductance e^2/h versus voltage on the n^+ GaAs substrate, the "back gate." On the logarithmic plot it is clear that the transistor has an on-to-off conductance ratio that exceeds 10^3 for the lowest gate voltages. The measurements were made at 30 mK with a source-drain voltage of only $2.5 \mu\text{V}$.

successful collaboration with M. Heiblum of IBM. The new structure was created by growing AlGaAs on a conductive substrate, followed by a layer of undoped GaAs. The electron density at the GaAs/AlGaAs interface, inverted from the usual configuration, was varied by applying a voltage to the substrate. Heiblum was able to grow such inverted heterojunctions with mobilities of $\sim 500,000 \text{ cm}^2/\text{V}\cdot\text{s}$.

Next, the conducting channel is defined by depositing a metal gate on top of the GaAs, and a gap is patterned in the gate by electron beam lithography. Because a depletion region is created under the gate, the electrons accumulate only under the gap. In order to emulate the effect of two charged impurities, two constrictions are patterned in the gap. The electron beam lithography was done at IBM with the help of Shalom Wind.

Devices of this kind worked exactly as we hoped they would.⁴ Periodic oscillations of the conductance were seen again, but now they were controlled: The period was the same for different devices with the same spacing between constrictions and was larger when the spacing was shorter, consistent with the idea that the same number of electrons is added for one period in all devices. Calculations of the capacitance of such devices are only consistent with each period corresponding to one electron added per oscillation.

This is an amazing result: Figure 1 shows that the conductance consists of periodic, narrow, well-separated resonances. The conductance rises and falls by a factor ~ 1000 with a variation of gate voltage that corresponds to only $\sim 1/3$ of an electron.

⁴ U. Meirav, M.A. Kastner, and S.J. Wind, "Single Electron Charging and Periodic Conductance Resonances in GaAs Nanostructures," *Phys. Rev. Lett.* 65: 771 (1990).

We now understand quite well why the Single Electron Transistor works the way it does. The conductance results from resonant tunneling, and Professor Patrick Lee and his collaborators have shown that the states arise from single particle quantum states (the Fabry-Perot states induced by the two barriers, the same as expected for any "quantum dot"), but that the energies of the levels are dominated by the Coulomb interaction between the electrons in the isolated segment.

Experiments in the quantum Hall regime⁵ at first seemed to indicate that the nature of the quantum states was very simple. By measuring the position in gate voltage of a series of conductance resonances, we were able to measure the energies for adding a series of electrons as a function of magnetic field. Figure 2 shows (top panel) how the peak positions oscillated with magnetic field. Subtracting a constant V_0 difference from each pair of curves we emulated the effect of subtracting a constant Coulomb energy. We thereby obtained the level spectrum shown in the lower panel.

The level spectrum looks remarkably similar to that for non-interacting electrons in a magnetic field and a confining electrostatic potential. We thought, therefore, that the simple Coulomb blockade model, with a constant Coulomb interaction between any two electrons in the isolated region, was adequate. However, more careful analysis of data like that in figure 2 shows that this simple picture is inadequate. In particular, the difference in energies for electron spin parallel and antiparallel to the magnetic field are much too large in the experiment.

Recently, a density functional model for the isolated region has been developed in collaboration with Professor Lee's group. The good agreement between the model and the experimental results shows that electrons in different spatial and even spin states have very different Coulomb interactions. This is a major step in deepening our understanding of the physics of single electron transistors.

Publications

McEuen, P.L., E.B. Foxman, U. Meirav, M.A. Kastner, Y. Meir, N.S. Wingreen, and S.J. Wind. "Transport Spectroscopy of a Coulomb Island in the Quantum Hall Regime." *Phys. Rev. Lett.* 66: 1926 (1991).

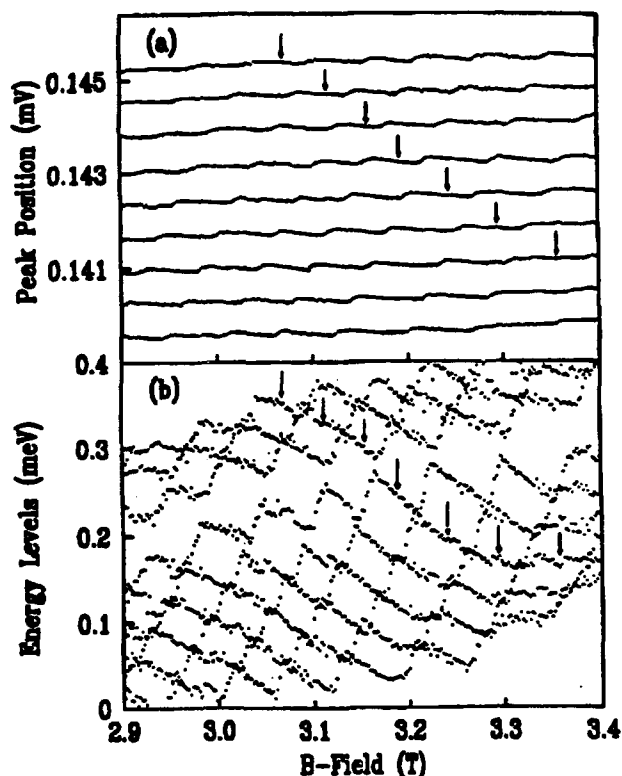
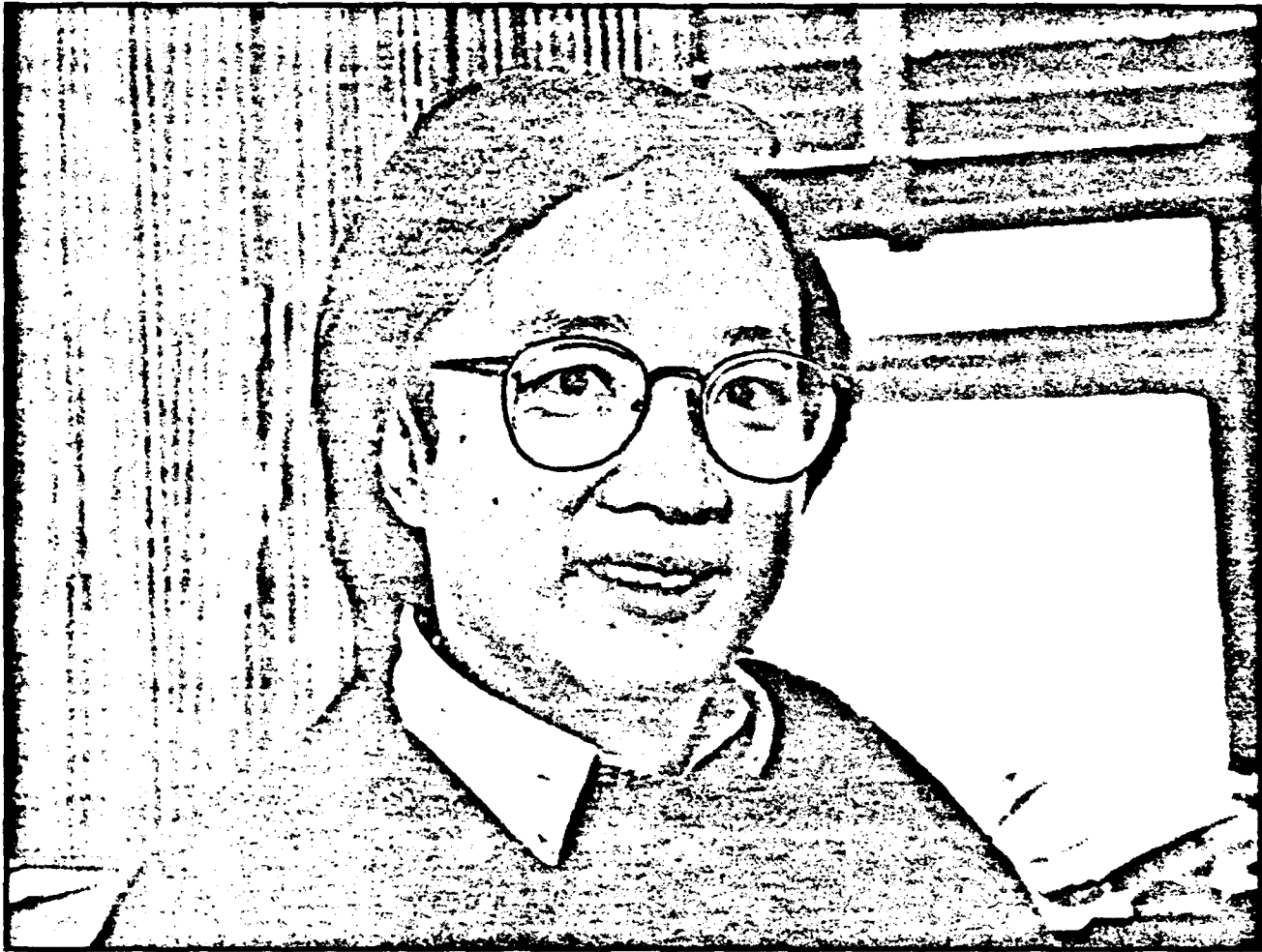


Figure 2. (a) The gate voltages corresponding to a series of consecutive conductance peaks like those in figure 1, as a function of magnetic field. (b) Result of subtracting a constant voltage from each successive peak in (a). This gives the energy for adding the next electron as a function of field with the average Coulomb interaction subtracted. The arrows follow a particular level as it moves through successive peaks.

⁵ P.L. McEuen, E.B. Foxman, U. Meirav, M.A. Kastner, Y. Meir, N.S. Wingreen and S.J. Wind, "Transport Spectroscopy of a Coulomb Island in the Quantum Hall Regime," *Phys. Rev. Lett.* 66: 1926 (1991).



Professor Patrick A. Lee

Chapter 3. Transport Through a Quantum Dot

Academic and Research Staff

Professor Patrick A. Lee, Dr. Yigal Meir, Dr. Ned S. Wingreen

Graduate Students

Jari M. Kinaret

Technical and Support Staff

Imadiel Ariel

3.1 Project Description

Sponsor

Joint Services Electronics Program

Contract DAAL03-89-C-0001

Contract DAAL03-92-C-0001

We continue the study of electron transport through a quantum dot. It is now well established both experimentally¹ and theoretically² that Coulomb blockade plays a key role in this problem and is responsible for the conductance peaks which have been observed to be periodic as a function of gate voltage. Each of these conductance peaks occurs at a gate voltage where the energy of N and $N+1$ electron state are degenerate and each peak corresponds to the addition of a single electron to the quantum dot. In the past year, the general formalism developed by Meir et al.² has been extended and applied to the case where a strong magnetic field is applied to the system. The field is strong enough so that only the lowest two Landau levels are occupied, i.e., the system would be in the integer quantum Hall regime in the bulk. The advantage of this system is that the single particle states are well known to be edge states, and the energy of these states are well understood as a function of magnetic field. Thus, the successful application of the theory to explain the experimental data³ provides strong support for the general theory² of Coulomb blockade in resonant tunneling.

Experimentally it was found that in the presence of a strong magnetic field, the location in gate

voltage of each conductance peak exhibits small periodic fluctuation. At the same time, the magnitude of each conductance peak goes through deep minima. This can be explained based on a model where the low lying states are the edge states of the first and second Landau levels. For a given conductance peak, the number of electrons on the quantum fluctuates between N and $N+1$. However, as the magnetic field is increased, the N electrons are distributed between the two Landau levels in a different way, and electrons are transferred from the second Landau level to the first. The transfer occurs when the edge state of the first Landau level crosses the edge state of the second Landau level. Thus, as a function of a magnetic field, we are watching the transfer of electrons from the second to the first Landau level, one electron at a time. Furthermore, since the dependence of the energy of the edge state on magnetic field is understood, the periodic fluctuation of the resonant energy with magnetic field can be understood. The dips in the magnitude of the conductance peak can also be explained as being due to the fact that the edge state of the second Landau level is more tightly bound, and its coupling to the leads is much smaller so that a dip occurs every time the second Landau level moves through the chemical potential of the leads. Based on this picture, quantitative calculation of the temperature dependence of the peak position was made and successfully compared with the experiment. Indeed, we now have sufficient confidence in the model that the problem can be turned around, and we can use the experiment as a spectroscopy of the single particle level, i.e., we can

¹ U. Meirav, M.A. Kastner, and S.J. Wind, *Phys. Rev. Lett.* 65: 771 (1990).

² Y. Meir, N.S. Wingreen, and P.A. Lee, "Transport through a Strongly Interacting Electron System: Theory of Periodic Conductance Oscillations," *Phys. Rev. Lett.* 66: 3048 (1991).

³ P.L. McEuen, E.B. Foxman, U. Meirav, M.A. Kastner, Y. Meir, N.S. Wingreen, and S.J. Wind, "Transport Spectroscopy of a Coulomb Island in the Quantum Hall Regime," *Phys. Rev. Lett.* 66: 1926 (1991).

extract the dependence of the edge state energy level as a function of magnetic field.

Publications

Feng, S., and P.A. Lee. "Mesoscopic Conductors and Correlations in Laser Speckle Patterns." *Sci.* 251: 633 (1991).

Kinaret, J., and P.A. Lee. "Conductance of a Disordered Narrow Wire in a Strong Magnetic Field." *Phys. Rev. B*. Forthcoming.

Lee, P.A. "Small Structures: A Laboratory for Studying Strongly Interacting Systems," *Pro-*

ceedings of the Taniguchi Symposium on Mesoscopic Physics 1991. Shima, Japan. Forthcoming.

McEuen, P.L., E.B. Foxman, U. Meirav, M.A. Kastner, Y. Meir, N.S. Wingreen, and S.J. Wind. "Transport Spectroscopy of a Coulomb Island in the Quantum Hall Regime." *Phys. Rev. Lett.* 66: 1926 (1991).

Meir, Y., N. Wingreen, and P.A. Lee. "Transport Through a Strongly Interacting Electron System: Theory of Periodic Conductance Oscillations." *Phys. Rev. Lett.* 66: 3048 (1991).

Chapter 4. Submicron and Nanometer Structures Technology and Research

Academic and Research Staff

Professor Henry I. Smith, Professor Dimitri A. Antoniadis, James M. Carter, Robert C. Fleming Jr., Dr. Mark L. Schattenburg

Visiting Scientists and Research Affiliates

Dr. Khalid Ismail,¹ Seppo Nenonen,² Yang Zhao³

Graduate Students

Martin Burkhardt, Mike T. Chou, William Chu, Steven S. Cooperman, Kathleen R. Early, Cristopher C. Eugster, Jerrold A. Floro, Reza A. Ghanbari, Scott D. Hector, Hang Hu, Harold Kahn, Yao-Ching Ku, Arvind Kumar, Ady Levy, Ya-Chin Liu, Hai P. Longworth, Alberto M. Moel, George E. Rittenhouse, Lisa T-F. Su, Vincent V. Wong, Kenneth Yee, Anthony Yen

Undergraduate Students

Juan Ferrera, Michael H.Y. Lim, Euclid E. Moon, Pablo Munguia, Lee-Peng Ng, Daniel B. Olster, Flora S. Tsai, Sabah Yunus

Technical and Support Staff

Donna R. Martinez, Mark K. Mondol, Jeanne M. Porter

4.1 Submicron Structures Laboratory

The Submicron Structures Laboratory at MIT develops techniques for fabricating surface structures with feature sizes in the range from nanometers to micrometers and uses these structures in a variety of research projects. These projects, which are described briefly below, fall into four major categories: (1) development of submicron and nanometer fabrication technology; (2) nanometer and quantum-effect electronics; (3) crystalline films on non-lattice-matching substrates; and (4) periodic structures for x-ray optics, spectroscopy and atomic interferometry.

4.2 Microfabrication at Linewidths of 100 nm and Below

Sponsors

Joint Services Electronics Program
Contract DAAL03-89-C-0001
Contract DAAL03-92-C-0001
National Science Foundation
Grant ECS 90-16437

Project Staff

Martin Burkhardt, James M. Carter, William Chu, Kathleen R. Early, Reza A. Ghanbari, Scott D. Hector, Yao-Ching Ku, Alberto M. Moel, George E. Rittenhouse, Dr. Mark L. Schattenburg, Professor Henry I. Smith, Vincent V. Wong, Anthony Yen

A variety of techniques for fabricating structures with characteristic dimensions of 100 nm (0.1 μm)

¹ University of Cairo, Giza, Egypt, and IBM Corporation, Thomas J. Watson Research Center, Yorktown Heights, New York.

² Outokumpu Electronics, Espoo, Finland.

³ Princeton University, Princeton, New Jersey.

and below are investigated. These include: x-ray nanolithography, holographic lithography, achromatic holographic lithography, electron-beam lithography, focused-ion-beam lithography, reactive-ion etching, electroplating, and liftoff. Development of such techniques is essential if we are to explore the rich field of research applications in the deep-submicron and nanometer domains. X-ray nanolithography is of special interest because it can provide high throughput and broad process latitude at linewidths of 100 nm and below. As discussed in section 4.3, we have established a reliable mask technology, based on 1 μm -thick SiN_x membranes, as shown schematically in figure 1. Mask blanks are patterned by several techniques including electron-beam lithography, focused-ion-beam lithography, holographic lithography, and transfer from other x-ray masks.

For high-quality x-ray lithography, the mask-to-sample gap, G , must be precisely controlled. The mesa-rim architecture of figure 1 yields optically flat membranes enabling us to control gap down to about 2 microns by means of spacer studs. For 100 nm features a gap of 10 microns is suitable. However, for 50 nm features a gap of 2.5 microns is required. Figure 2 shows the replication of a planar-resonant-tunneling field-effect transistor pattern having 50 nm minimum features. The gap in this case was 2.7 microns. This gap is significantly larger than predicted by simple Fresnel diffraction formulae which neglect diffraction inside the mask absorber. Taking this into account, using vector electromagnetic calculations and

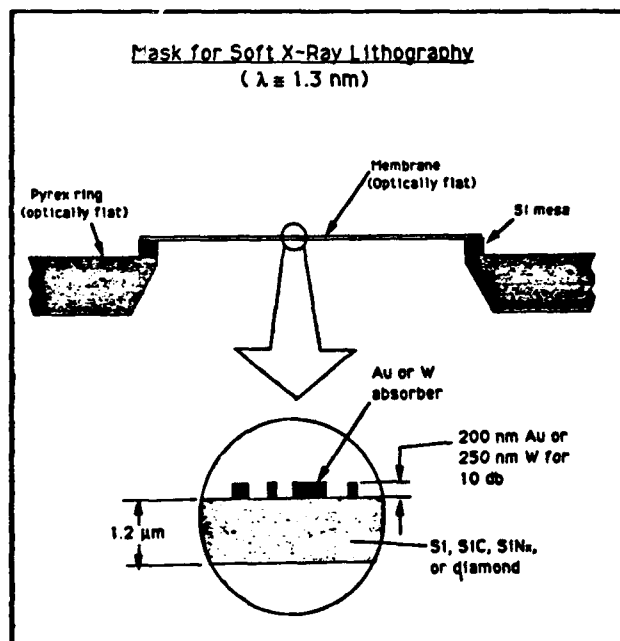
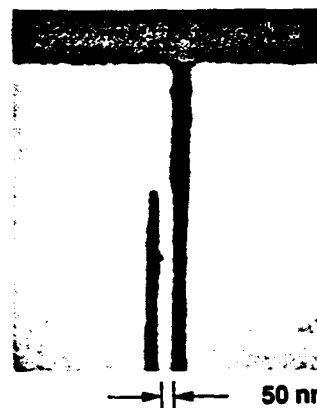


Figure 1. Structure of the new standard, 31 mm diameter, mesa-rim, x-ray mask suitable for lithography from 1000 to 20 nm feature sizes. Membranes are flat to $< 0.25 \mu\text{m}$.

Proximity X-ray Nanolithography



• 50 nm lines and spaces

• $\lambda = 1.32 \text{ nm}$ $G = 2.72 \mu\text{m}$

$$G = \alpha W^2 / \lambda$$

$$\alpha = 1.44$$

• Implication: If $W = 0.1 \mu\text{m}$, $\lambda = 1 \text{ nm}$

$$G = 10 \text{ to } 15 \mu\text{m}!$$

* PRESTFET \rightarrow Planar Resonant-Tunneling Field-Effect Transistor

Figure 2. Replication, using the Cu_L x-ray (1.3 nm) and a mask-substrate gap of 2.7 microns, of 50 nm line and space pattern.

accounting for the finite source size, we have developed a simulation that predicts image contrast as a function of feature size and gap. In order to increase the allowable gap for features of 70 nm and below, we are investigating the feasibility of near-field in-line x-ray holography.

Using the figure 1 mask architecture, patterns are readily transferred onto standard Si wafers. However, in research on GaAs or other III-V devices, substrates are often much smaller than the 31 mm-diameter mask membrane. We have developed an apparatus that allows us to bring the membrane into contact with such substrates during exposure, without risk of mask damage. Resolution down to 10-20 nm is feasible under such exposure conditions.

Alignment of x-ray masks to patterns pre-existing on a substrate is currently done with an optical imaging system equipped with a video camera. We are investigating electronically enhanced moiré imaging methods in order to achieve sub-10 nm alignment precision. In this approach the gap is

set at ~ 4 microns and the mask translated piezoelectrically.

The achromatic holographic lithography system in conjunction with an anti-reflection coating (ARC) specially formulated for the 193 nm wavelength is now producing high quality images, as shown in figure 3. The ARC consists of PMMA and a bis-azide, 4, 4'-diazidodiphenyl sulfone.

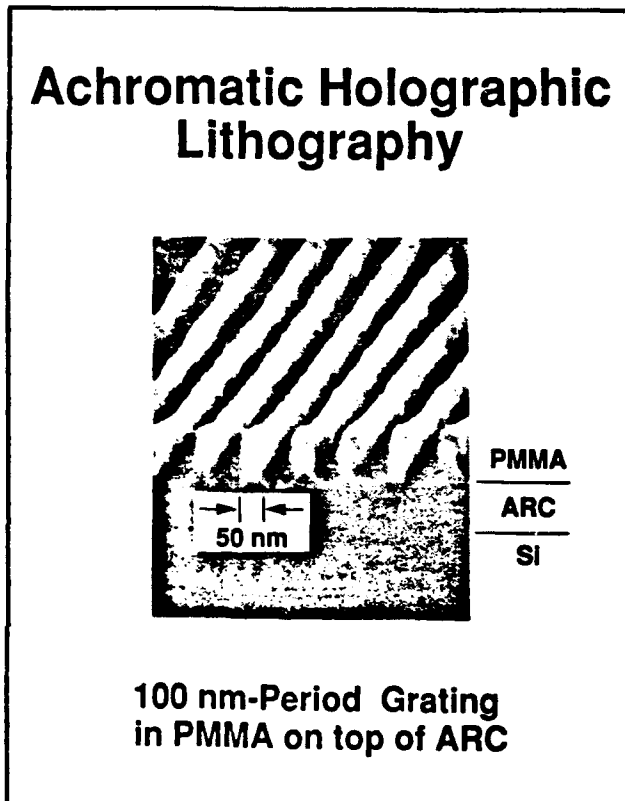


Figure 3. A 100 nm-period grating exposed in PMMA on top of an anti-reflection coating (ARC) by achromatic holographic lithography using the ArF laser at 193 nm.

4.3 Improved Mask Technology for X-Ray Lithography

Sponsors

National Science Foundation
Grant ECS 90-16437
Semiconductor Research Corporation
Contract 90-SP-080
U.S. Navy - Naval Research Laboratory
Contract N00014-90-K-2018

Project Staff

Juan Ferrera, Yao-Ching Ku, Mark K. Mondol, Lee-Peng Ng, Dr. Mark L. Schattenburg, Professor Henry I. Smith, Flora S. Tsai, Sabah Yunus

The x-ray mask architecture shown in figure 1 is compatible with both our research in the sub-100 nm domain and the commercial fabrication of submicron integrated electronics. For the latter application especially, distortion in the mask must be eliminated. Distortion can arise from stress in the absorber, which is usually gold (Au) or tungsten (W). We have developed means of sputtering W so that the stress is below 5×10^7 dynes/cm², and the distortion induced by stress is below the level of detectability in a Linnik interferometer. The corresponding in-plane pattern distortion is calculated to be less than 1 nm. We are currently developing an interferometer to directly measure in-plane distortion.

Membranes of SiN_x are preferred at the present time because they can be made by conventional LPCVD methods and are extremely rugged and resistant to breakage. (SiN_x membranes only 1 micron thick can even be used as vacuum windows, 20 mm in diameter.) Membranes are characterized by their optical transmission, resonant frequency and bulge under pressure. From these measurements we extract index of refraction, optical attenuation, thickness, stress, and Young's modulus. We have also made radiation hardness measurements on membranes by subjecting them to the equivalent of one million exposures on the University of Wisconsin synchrotron. Effects of x radiation on membrane stress are extremely small, and we believe this can be eliminated by reducing the oxygen content of the SiN_x. To this end a special purpose LPCVD reactor for low-stress SiN_x will be set up within the Integrated Circuit Laboratory at MIT.

We are collaborating with the Naval Research Laboratory (NRL) in using their JEOL JBX5D11 e-beam lithography system to pattern x-ray masks. The patterns are generated using the CAD tools at MIT, converted to an acceptable binary intermediate format, transferred to NRL via ARPA Internet, converted there to the JEOL format, and written onto mask blanks that we send in advance to NRL (by express mail). Once the masks are written, they are shipped back to MIT for further processing. This collaboration has been fruitful for a number of projects including short-channel MOSFETs (section 4.4), multiple-parallel one-dimensional conductors (section 4.6), and the electron waveguide device (section 4.7).

4.4 Study of Electron Transport in Si MOSFETs with Deep-Submicron Channel Lengths

Sponsors

IBM Corporation
Joint Services Electronics Program
Contract DAAL03-89-C-0001
Contract DAAL03-92-C-0001
Semiconductor Research Corporation
Contract 90-SP-080

Project Staff

Professor Dimitri A. Antoniadis, Professor James Chung, Dr. Hao Fang, Hang Hu, Professor Henry I. Smith, Lisa T-F. Su

We have continued using x-ray lithography to fabricate both N and P channel MOSFET devices with effective channel length down to 80 nm. As channel lengths decrease below about 150 nm, electron velocity overshoot, and thus an increase of device transconductance has been observed both at room temperature and liquid nitrogen temperature. It appears that the necessary conditions for this phenomenon are high carrier mobility close to the Si/SiO₂ interface, and low parasitic resistance. The former is achieved in both our NMOSFET and PMOSFET devices by utilizing a super steep retrograde doping of the channel. In the NMOSFET case, indium, by virtue of its heavier mass and desirable doping profile in silicon, has been used to give retrograde threshold control doping with low surface concentration and yet high peak concentration. In the PMOSFET case, arsenic has been used to achieve the same goals.

Record saturation transconductance of over 1S/mm in deep submicron NMOSFET with channel length down to 100 nm was obtained with the indium doping technique. This underscores the achievement of increased surface mobility with the steeper retrograde channel doping. A transconductance of 0.23 S/mm was achieved in deep-submicron PMOSFET.

As shown in figure 4 we have developed a technology for self-aligned silicide N/PMOSFET device fabrication for the purpose of significantly reducing parasitic resistance. We have used cobalt deposition on the exposed silicon of source/drain and the exposed polysilicon of the gate electrode with a subsequent two-step rapid thermal annealing to form cobalt silicide (CoSi₂). Thin oxide spacers around the gate electrode have been used to prevent shorts between gate and source/drain. These process improvements were

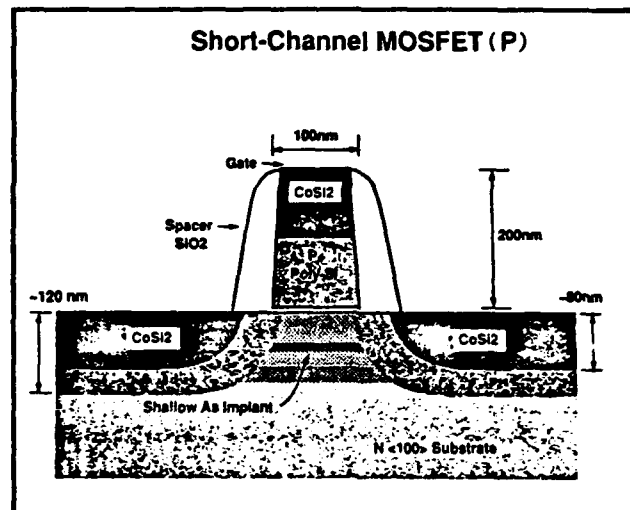


Figure 4. Configuration of self-aligned, 100 nm-channel-length, P-MOSFET.

tested first with conventional lithography where the submicron gate was achieved by resist erosion in an O₂ plasma after resist exposure and development. The first ultrashort channel self-aligned silicide MOSFET devices with channel length down to 0.12 μm for PMOS and 0.15 μm for NMOS and parasitic resistance down to 400 ohms per micron width have been successfully fabricated.

More recently, SiN_x-membrane x-ray mask technology has allowed us to use x-ray lithography for the definition of the gates. X-ray masks were patterned by electron-beam lithography at the Naval Research Laboratory, as shown in figure 5. Fabrication of both NMOSFET and PMOSFET devices with the new lithography technology and new cobalt silicide shallow junction source/drain technology should give us 100 nm channel length CMOS circuits compatible with commercial mass production.

4.5 Studies of Coulomb Charging in Ultrasmall Semiconductor Devices

Sponsor

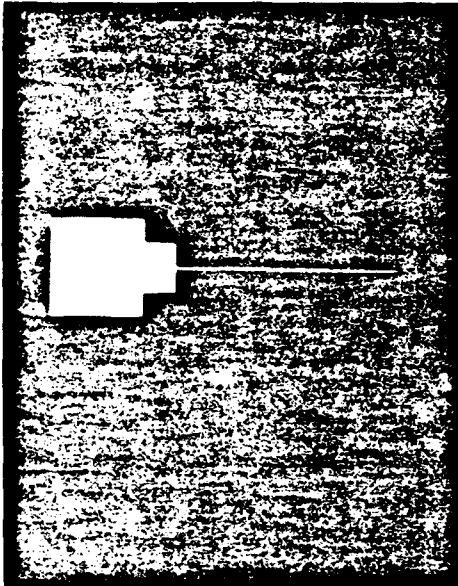
Joint Services Electronics Program
Contract DAAL03-89-C-0001
Contract DAAL03-92-C-0001
U.S. Air Force - Office of Scientific Research
Grant F49620-92-J-0064

Project Staff

Professor Dimitri A. Antoniadis, Professor Marc A. Kastner, Arvind Kumar, Professor Terry P. Orlando, Professor Henry I. Smith

X-ray Mask for 0.1 μ m MOSFET [Written by E-Beam Lithography at NRL]

Gate Pattern



Gate Length = 0.2 μ m

Gate Width = 25 μ m

Figure 5. Scanning electron micrograph of x-ray mask for the 100 nm channel-length MOSFET. The e-beam patterning was done at the Naval Research Laboratory, the plating and x-ray lithography was done at MIT.

In previous studies on very narrow silicon MOSFETs fabricated using x-ray lithography a fundamentally different mechanism to modulate the low-temperature electrical conduction was found. When the devices were cooled to the milli-Kelvin range, the electrical conductance exhibited a series of sharp oscillations which were almost perfectly periodic in the voltage of the gate used to control the electron density. This periodic modulation of the conductance was thought to be caused by presence of two dominant impurities in the electron channel which resulted in an isolated segment of the electron gas. In order to test the two-impurity hypothesis, the structure illustrated in figure 6(a) was fabricated using electron beam lithography and liftoff. The structure, fabricated on an inverted GaAs/AlGaAs heterostructure, consists of two Schottky gates used to squeeze the electron gas laterally, while the n+ substrate serves as a bottom gate to independently modulate the channel electron density. The two sets of constrictions were intended to emulate the potential due to the two impurities in the MOSFET device,

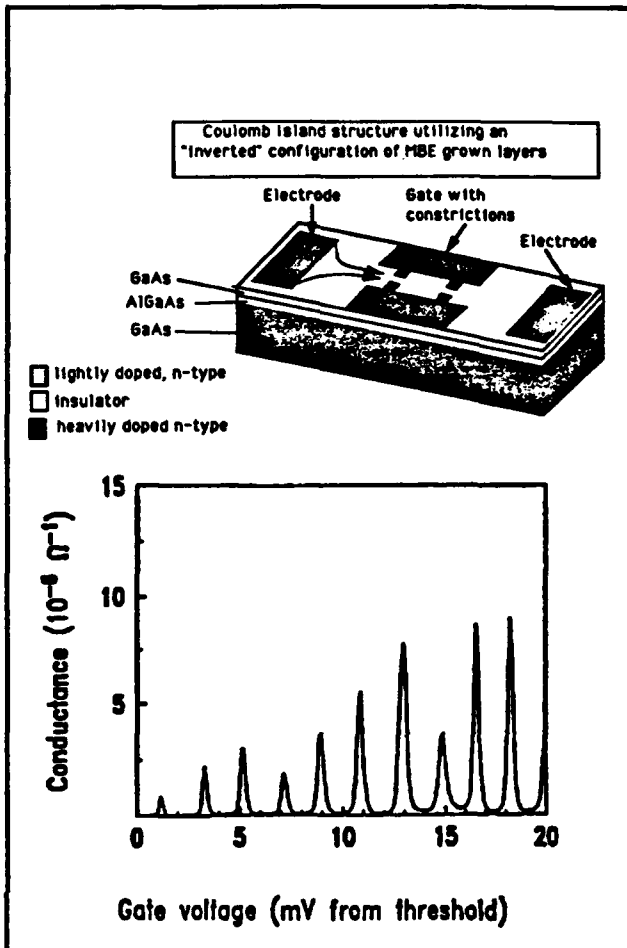


Figure 6. (a) Device structure used to study Coulomb blockade effects. A negative voltage on the two Schottky gates on the top depletes the electron gas at the lower GaAs/AlGaAs interface below, forming a narrow electron channel interrupted by two potential barriers at the constrictions. The n+ GaAs substrate serves as a bottom gate to modulate the channel electron density. (b) Periodic oscillations in the conductance as a function of bottom gate voltage for the device shown in (a).

while the mobility was sufficiently high to reduce the probability of unwanted accidental impurities.

When cooled to milli-Kelvin temperatures, conductance oscillations periodic in the bottom gate voltage were again observed, as shown in figure 6(b). Moreover, the voltage separation between successive conductance peaks was found to depend on the separation between the two potential barriers. To better understand these structures, we performed semi-classical calculations of potential profiles and electron densities for the structure in figure 6(a). Equipotential contours near the AlGaAs/GaAs interface are shown in figure 7 for a typical bias point with the shaded regions indicating areas occupied by inversion electrons.

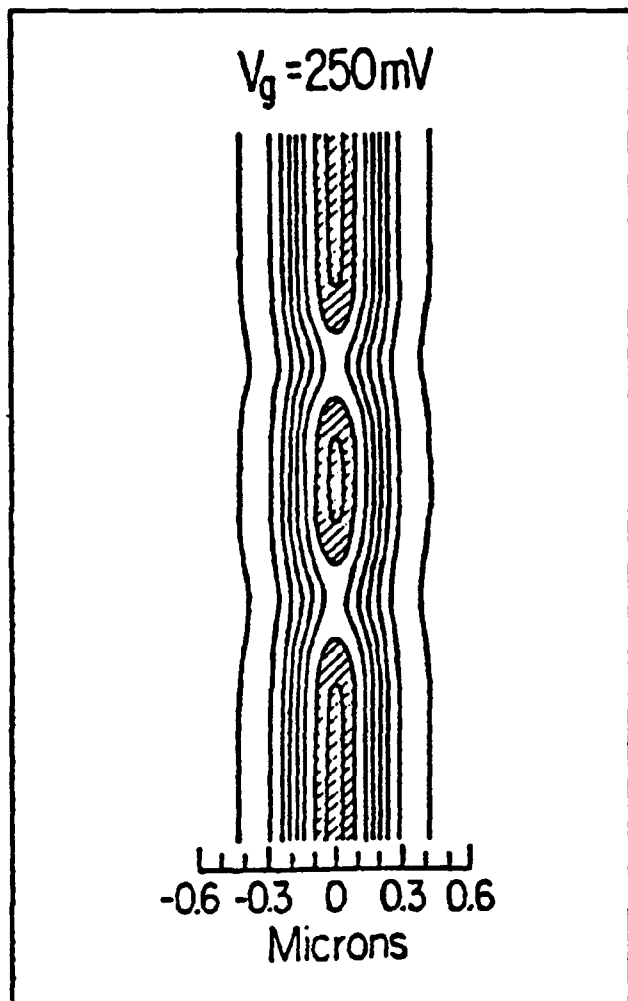


Figure 7. Equipotential contours for the device in figure 6(a) near the lower GaAs/AlGaAs interface at a typical bias point. The shaded regions indicate areas occupied by electrons. The two sets of constrictions result in an isolated electron segment, or "island," through which transport can be thermally activated.

We calculated the integrated electron charge in the isolated electron segment, or "island," between the sets of constrictions as a function of bottom gate voltage and found that it is approximately linear in bottom gate voltage, and that the voltage required to add one electron to the island is very nearly the spacing between successive conductance peaks. Thus, each conductance peak corresponds to the addition of a single electron to the island. This modulation of the conductance by changing the charge by a single electron can be understood in terms of a theory known as Coulomb blockade. According to the Coulomb blockade theory, a conductance valley corresponds to the electrostatic energy of the island being minimized by an integer number of electrons, so that addition of another electron costs some finite charging energy and transport is thermally activated. A conductance peak, on the other hand, corresponds to a state of

the island where the electrostatic energy is minimized by a half-integer number of electrons, so that there is no energy barrier to adding another electron. These two states repeat cyclically in bottom gate voltage, resulting in the observed periodic modulation of the conductance.

We are presently enhancing our understanding of Coulomb blockade effects both experimentally and theoretically. We first plan to reproduce the effect in a conventional modulation-doped GaAs/AlGaAs heterostructure, which is much more widely available than the inverted heterostructure. Secondly, we are working to understand all the capacitance components to the island in addition to the bottom gate capacitance described above. This is important because the observability temperature for Coulomb effects depends inversely on the total capacitance of the island, so that reducing the island capacitance is key to observing these effects at temperatures above the milli-Kelvin regime. Finally, we plan to study experimentally transport through more than one dot as well as the coupling of dots in parallel.

Because the modulation of the conductance is so strong, Coulomb blockade is among the most promising of novel effects in ultrasmall structures for long-term applications.

4.6 Study of Quasi-One-Dimensional Wires and Superlattice Formation in GaAs/AlGaAs Modulation Doped Field-Effect Transistors

Sponsor

U.S. Air Force - Office of Scientific Research
Grant F49620-92-J-0064

Project Staff

Professor Dimitri A. Antoniadis, Martin Burkhardt, William Chu, Professor Jesús A. del Alamo, Reza A. Ghanbari, Professor Terry P. Orlando, Professor Henry I. Smith

We have continued to use the modulation-doped field-effect transistor (MODFET) to explore electron back diffraction effects and reduced dimensionality effects in the GaAs/AlGaAs system. Because such devices have critical dimensions on the order of 100 nm, the use of x-ray lithography for fine feature definition has been central to our strategy. Recent results in our laboratory indicate that there may be a significant advantage in using x-ray lithography over direct-write e-beam lithography to fabricate quantum-effect electronic

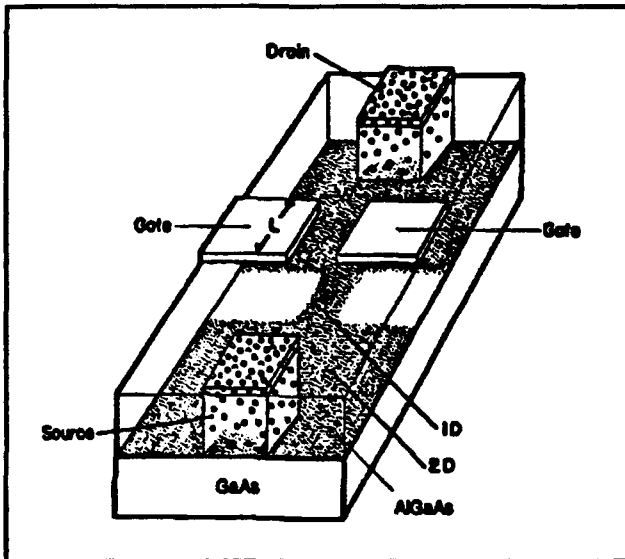


Figure 11. Schematic of an electron waveguide device defined by the split-gate configuration. The shaded region represents the electron concentration at the AlGaAs/GaAs interface.

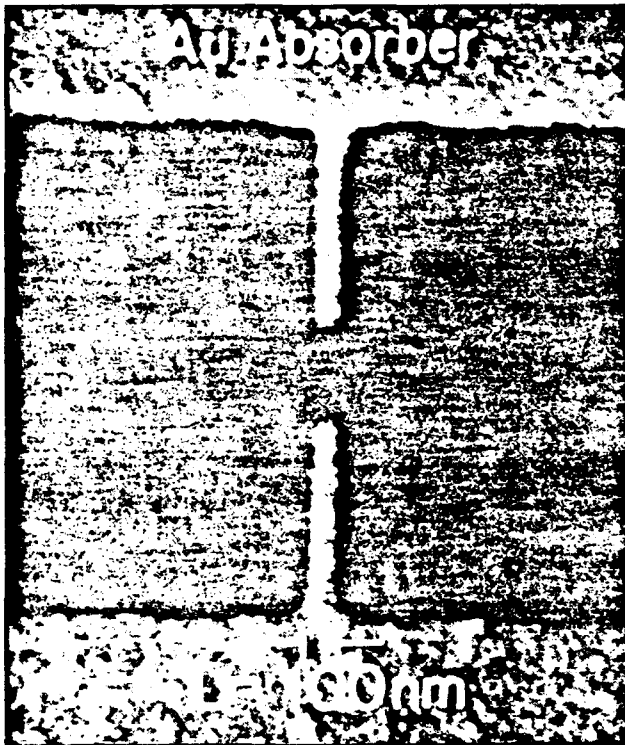


Figure 12. Top view of a parent x-ray mask showing the pattern for a 0.1 μm -long waveguide device.

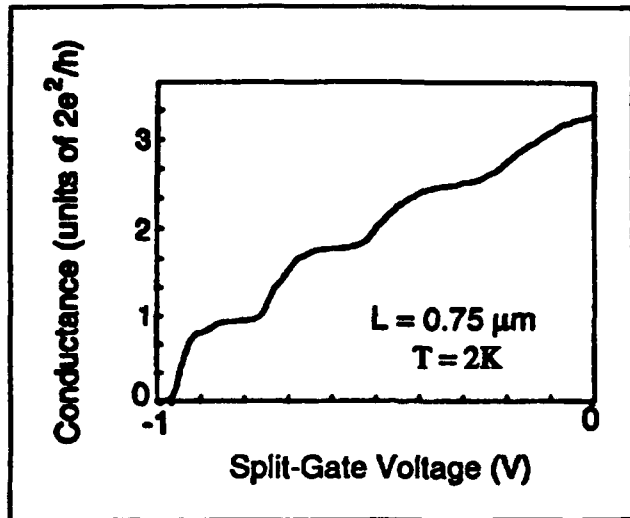


Figure 13. Conductance of a $L = 0.75 \mu\text{m}$ electron waveguide device as a function of split-gate voltage.

4.8 Arrays of Field-Effect-Induced Quantum Dots

Sponsors

Joint Services Electronics Program

Contract DAAL03-89-C-001

Contract DAAL03-92-C-001

U.S. Air Force - Office of Scientific Research

Grant F49620-92-J-0064

Project Staff

Professor Dimitri A. Antoniadis, Martin Burkhardt, Reza A. Ghanbari, Professor Terry P. Orlando, Professor Henry I. Smith, Professor M. Shayegan,⁴ Professor Daniel Tsui,⁴ Yang Zhao⁴

A metal grid on a modulation-doped AlGaAs/GaAs substrate (depicted in figure 14a) produces a two-dimensional periodic potential modulation at the AlGaAs/GaAs interface via the Schottky effect. If a gate electrode is attached to the grid, the potential can be further modified with an external voltage source. By changing the gate voltage from positive to negative values, the potential seen by the electrons located at the AlGaAs/GaAs interface can be varied from uniform (in which case the electrons behave as a 2-D electron gas), to weakly coupled zero-D quantum wells (figure 14b), to isolated zero-D quantum dots (figure 14c). We have made such structures with spatial periods of 200 nm in both orthogonal directions and covering

⁴ Princeton University, Princeton, New Jersey.

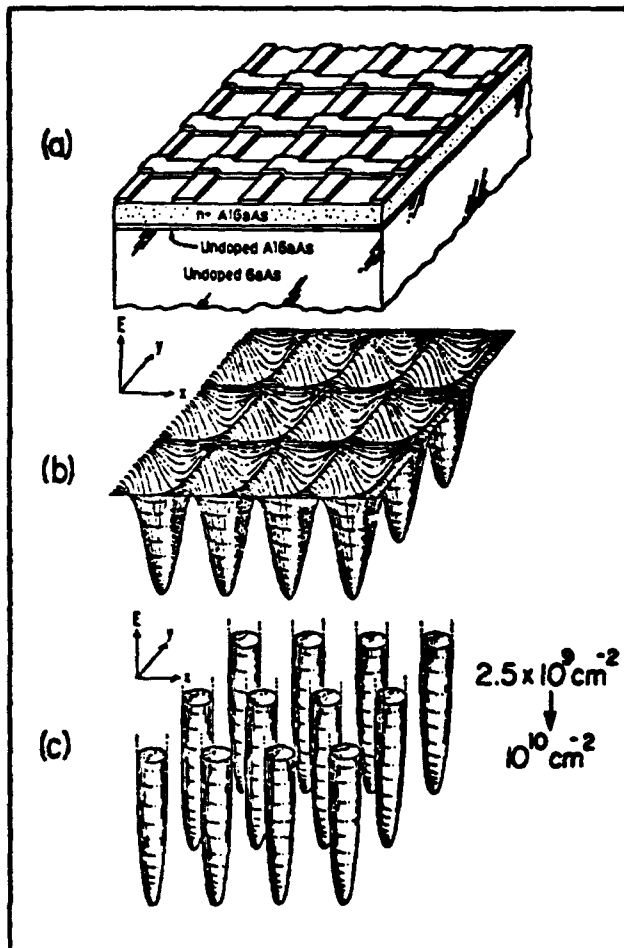


Figure 14. (a) Metal grid gate on a modulation-doped AlGaAs/GaAs substrate; (b) Depiction of potential seen by electrons at the AlGaAs/GaAs interface for weakly coupled quantum dots; (c) Potential for the case of isolated quantum dots.

areas of several square millimeters. The isolated quantum dots and the attendant zero-dimensional electronic sub-bands were examined in collaboration with D. Tsui at Princeton University using far-infrared (FIR) cyclotron resonance. Transitions between the discrete energy levels in the quantum dots were observed as a function of magnetic field. Results were in agreement with a theoretical model.

Currently, we are continuing our study using extremely high quality samples prepared by M. Shayegan's group at Princeton. With mobilities typically greater than 10^6 cm²/Vsec, the resolution of the experiments should improve dramatically.

4.9 Planar-Resonant-Tunneling Field-Effect Transistors (PRESTFET)

Sponsor

U.S. Air Force - Office of Scientific Research
Grant F49620-92-J-0064

Project Staff

Professor Dimitri A. Antoniadis, Mike T. Chou, William Chu, Professor Henry I. Smith

Previously, we reported on the performance of a planar-resonant-tunneling field-effect transistor (PRESTFET) depicted in figure 15, in which the gate electrodes were 60 nm long and separated by 60 nm. Clear evidence of resonant tunneling through the bound states in the well between electrodes was observed, as shown in figure 15(b).

In order to reduce the electrode separation while retaining a large process latitude, we have chosen to pursue a new technology for making the PRESTFET. In collaboration with S. Rishton of IBM, a high-performance e-beam nanolithography system was used to write PRESTFET patterns on SiN_x x-ray mask membranes, 1 μm thick. Reduced backscattering from the thin membrane has permitted us to achieve 50 nm lines and spaces. We hope to get even finer features in the future. The written masks are processed at MIT, replicated using the Cu_x x-ray (1.3 nm), and Schottky electrodes formed by liftoff. Masks are aligned to GaAs substrate using a specially built alignment and exposure station.

4.10 Fabrication of Distributed-Feedback Lasers and Channel-Dropping Filters

Sponsor

Joint Services Electronics Program
Contract DAAL03-89-C-0001
Contract DAAL03-92-C-0001

Project Staff

James M. Carter, Woo-Young Choi, Jay N. Damask, Professor Clifton G. Fonstad, Jr., Professor Herman Haus, Professor Leslie A. Kolodziejski, Professor Henry I. Smith, Vincent V. Wong

We are developing techniques to fabricate large area, spatially-coherent gratings for both quarter-wave-shifted distributed-feedback (DFB) lasers

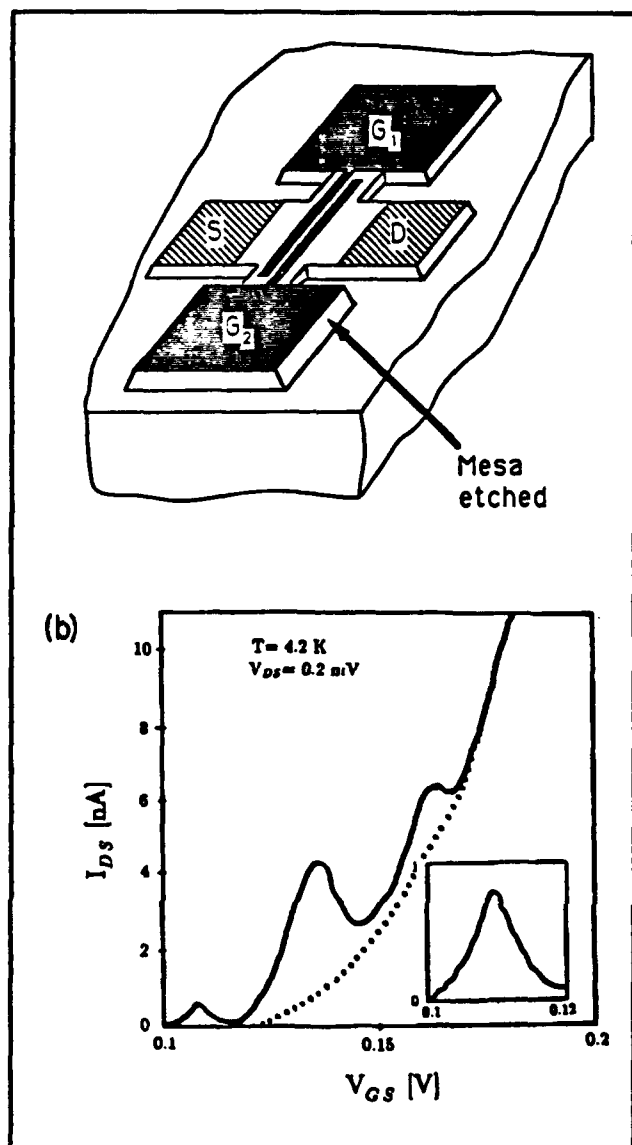


Figure 15. (a) Layout of a 4-terminal double-barrier planar-resonant-tunneling field-effect transistor (PRESTFET). (b) Plot of source-drain current versus gate voltage for a PRESTFET with 60 nm well width.

and channel-dropping filters (CDFs) on InP-based materials. The quality of these gratings is the most important factor determining the performance of these devices. Typical grating periods will be ~ 200 nm, and grating lengths will range from ~ 500 μm to several millimeters. Much of the nanofabrication technology developed in our lab over the years is directly applicable to the fabrication of these devices. SiN_x x-ray masks will be patterned using both holographic lithography and e-beam lithography, as described below. X-ray

lithography will then be used to define the device patterns on the InP-based material.

Through the use of holographic lithography, large-area, spatially-coherent grating patterns can be defined. Fine control of the grating period is also possible. However, the incorporation of the quarter-wave shift into the grating structure is not easily accomplished by holographic means. We are pursuing a technique that takes advantage of a unique aspect of x-ray lithography: the phase of a segment of a grating can be shifted by pi-radians by transferring it onto the back surface of the mask membrane. Grating structures containing single and multiple quarter-wave shifts, which are necessary for both DFB lasers and CDFs, will be fabricated using this technique.

The incorporation of quarter-wave shifts into a grating structure is straightforward with e-beam lithography. However, precise control of the grating period, and large-area, spatially-coherent grating patterns are not easily obtained with e-beam lithography. For precise control of the grating period, a continuously-variable field size is necessary. To achieve spatial coherence in the written gratings one must eliminate the stitching errors, which occur when writing adjacent fields. We are pursuing a technique based on a global-fiducial grid scheme which potentially can solve both of these problems. Once developed, this technique will be incorporated into the e-beam lithography process to define the appropriate DFB laser and CDF grating patterns onto a SiN_x x-ray mask.

4.11 Novel Superconducting Tunneling Structures

Sponsor

Joint Services Electronics Program
Contract DAAL03-89-C-0001
Contract DAAL03-92-C-0001

Project Staff

Professor John M. Graybeal, Dr. Bernard S. Meyerson,⁵ George E. Rittenhouse, Professor Henry I. Smith

In this program we seek to examine the behavior of short-channel hybrid Josephson devices, whose geometry is designed to display quantum electronic interference behavior. These devices represent the first attempt to observe Josephson

⁵ IBM Corporation.

coupling via resonant tunneling. The characteristic energy scale for such a device would be set by quantum confinement, and consequently may provide a new avenue for obtaining finite gains in Josephson three-terminal devices.

These novel structures consist of an ultrathin vertical Si membrane (the quantum well) sandwiched between two superconducting Nb counterelectrodes. These structures are fabricated using a combination of x-ray and optical lithography, anisotropic wet chemical etching, planarization and reactive dry etching techniques. The basic geometry of these new structures has now been fully validated using low-mobility uniformly doped Si wafers, where we find Josephson behavior consistent with the best published work on "conventional" Nb/Si/Nb junctions. However, no resonant tunneling effects were expected or observed in these devices due to their low mobility. Present work now centers on the fabrication of similar structures in high-mobility modulation-doped epitaxial layers grown on Si, where we expect resonant tunneling effects to appear.

4.12 Submicrometer-Period Transmission Gratings for X-Ray and Atom-Beam Spectroscopy and Interferometry

Sponsor

Joint Services Electronics Program
Contract DAAL03-89-C-0001
Contract DAAL03-92-C-0001

Project Staff

James M. Carter, Daniel B. Olster, Dr. Mark L. Schattenburg, Professor Henry I. Smith

Transmission gratings with periods of 100-1000 nm are finding increasing utility in applications such as x-ray, vacuum-ultraviolet, and atom-beam spectroscopy and interferometry. Over 20 laboratories around the world depend on MIT-supplied gratings in their work. For x-ray and UV spectroscopy, gratings are made of gold and have periods of 100-1000 nm, and thicknesses ranging from 100-1000 nm. They are most commonly used for spectroscopy of the x-ray emission from high-temperature plasmas. Transmission gratings are supported on thin (1 μ m) polyimide membranes or made self supporting ("free standing") by the addition of crossing struts (mesh). (For short x-ray wavelengths membrane support is desired, while for the long wavelengths a mesh support is preferred in order to increase efficiency.) Fabri-

cation is generally performed by holographic lithography, x-ray lithography and electroplating. Progress in this area tends to focus on improving the yield and flexibility of the fabrication procedures.

Another application is the diffraction of neutral sodium beams (de Broglie-wavelength ~ 17 pm) by mesh-supported gratings. Professor Pritchard's group at MIT has clearly demonstrated atomic diffraction and interference. Because good spatial coherence (low distortion) of the grating is critical to ensure measurable interference of the beams, efforts are concentrated on the use of holographic lithography and the reactive-ion etching of free-standing gratings in low stress and high stiffness materials such as silicon nitride. Results are shown in figure 16.

4.13 High-Dispersion, High Efficiency Transmission Gratings for Astrophysical X-Ray Spectroscopy

Sponsor

National Aeronautics and Space Administration
Contract NAS8-36748

Project Staff

Professor Claude R. Canizares, Robert C. Fleming, Dr. Mark L. Schattenburg, Professor Henry I. Smith

This work involves a collaboration between the Center for Space Research and the Submicron Structures Laboratory (SSL), providing transmission gratings for the Advanced X-ray Astrophysics Facility (AXAF) x-ray telescope, currently scheduled for launch in 1998. Many hundreds of low-distortion, large area transmission gratings of 200 nm period (gold) and 600 nm period (silver) are required. These will provide high resolution x-ray spectroscopy of astrophysical sources in the 100 eV to 10 keV band.

Because of the requirements of low distortion, high yield, and manufacturability, a fabrication procedure involving the replication of x-ray masks has been selected. Masks are made of high-stiffness silicon nitride membranes to eliminate distortion, and patterned using a process involving holographic lithography, reactive-ion etching, and electroplating. The masks are then replicated using soft x-rays (1-1.5 nm) and the resulting patterns electroplated with gold or silver. An etching step then yields membrane-supported gratings suitable for space use. Flight prototype gratings have been fabricated and continue to undergo space-worthiness tests. Progress in this area tends

Extensive numerical analysis of EGG using mean field coarsening theory has been performed. We have examined model interface energy functions (interface energy versus orientation) and shown which of the specific aspects of the interface energy function are important in promoting bimodal secondary or epitaxial grain growth, i.e., grain growth which is strongly orientation selective.

4.16 GaAs Epitaxy on Sawtooth-patterned Si

Sponsor

Joint Services Electronics Program
Contract DAAL03-89-C-0001
Contract DAAL03-92-C-0001
Spire Corporation

Project Staff

Professor Henry I. Smith, Kenneth Yee, Dr. Khalid Ismail, Nasser Karam⁶

The growth of GaAs on Si offers the possibility of combining high-speed and optoelectronic GaAs devices with Si integrated-circuit technology. Oriented gratings of 200 nm period are fabricated in Si_3N_4 on (100) Si substrates. Anisotropic etching in KOH is then used to produce sawtooth-profile gratings in the Si. These then serve as substrates for GaAs growth by MOCVD. The dislocation density in the grown GaAs films is orders of magnitude lower than the density in films formed on planar Si substrates.

4.17 Publications

4.17.1 Journal Articles

Anderson, E.H., V. Boegli, M.L. Schattenburg, D.P. Kern, and H.I. Smith. "Metrology of Electron Beam Lithography Systems Using Holographically Produced Reference Samples." *J. Vac. Sci. Technol.* B9: 3606-3611 (1991).

Bagwell, P.F., A. Yen, S.L. Park, D.A. Antoniadis, H.I. Smith, T.P. Orlando, and M.A. Kastner. "Magnetotransport in Multiple Narrow Silicon Inversion Channels Opened Electrostatically into a Two-Dimensional Electron Gas." *Phys. Rev. B* 45: April 1992.

Bagwell, P.F., and A. Kumar. "Comment on Effects of Channel Opening and Disorder on the Conductance of Narrow Wires." Submitted to *Phys. Rev. B*.

Chu, W., H.I. Smith, and M.L. Schattenburg. "Replication of 50nm Linewidth Device Patterns using Proximity X-ray Lithography at Large Gaps." *Appl. Phys. Lett.* 59: 1641-1643 (1991).

Chu, W., S.A. Rishton, M.L. Schattenburg, D.P. Kern, and H.I. Smith. "Fabrication of 50 nm Line-and-Space X-ray Masks in Thick Au Using a 50 keV Electron Beam System." *J. Vac. Sci. Technol. B* 10: 118-121 (1992).

Early, K., G.E. Rittenhouse, J.M. Graybeal, and H.I. Smith. "Sub-100- and Sub-10-nm-thick Membranes Anisotropically Etched in (110) Silicon." Submitted to *Appl. Phys. Lett.*

Geis, M.W., H.I. Smith, A. Argoitia, J. Angus, G.H.M. Ma, J.T. Glass, J. Butler, C.J. Robinson, and R. Pryor. "Large-Area Mosaic Diamond Films Approaching Single-Crystal Quality." *Appl. Phys. Lett.* 58: 2485 (1991).

Ismail, K., M. Burkhardt, H.I. Smith, N.H. Karam, and P.A. Sekula-Moise. "Patterning and Characterization of Large-Area Quantum-Wire Arrays." *Appl. Phys. Lett.* 58: 1539-1541 (1991).

Ismail, K., P.F. Bagwell, T.P. Orlando, D.A. Antoniadis, and H.I. Smith. "Quantum Phenomena in Field-Effect-Controlled Semiconductor Nanostructures." *Proc. IEEE* 79: 1106-1116 (1991).

Ismail, K., F. Legoues, N.H. Karam, J. Carter, and H.I. Smith. "High Quality GaAs on Sawtooth-Patterned Si Substrates." *Appl. Phys. Lett.* 59: 2418-2420 (1991).

Karam, N.H., A. Mastrovita, V. Haven, K. Ismail, S. Pennycok, and H.I. Smith. "Patterning and Overgrowth of Nanostructure Quantum Well Wire Arrays by LP-MOVPE." *J. Crystal Growth* 107: 591-597, (1991)

Ku, Y.C., Lee-Peng Ng, R. Carpenter, K. Lu, H.I. Smith, L.E. Haas, and I. Plotnik. "In-Situ Stress Monitoring and Deposition of Zero Stress W for

⁶ Spire Corporation.

Chapter 1. Optics and Quantum Electronics

Academic and Research Staff

Professor Hermann A. Haus, Professor Erich P. Ippen, Professor James G. Fujimoto, Professor Peter L. Hagelstein, Dr. Santanu Basu, Dr. Joseph A. Izatt

Visiting Scientists and Research Affiliates

Dr. Lucio H. Acioli, Dr. Guiseppe Gabetta, Dr. Yuzo Hirayama, Dr. Franz X. Kärtner, Dr. Charles P. Lin, Dr. Antonio Mecozzi, Dr. Kazunori Naganuma, Dr. Masataka Shirasaki

Graduate Students

Keren Bergman, John Paul Braud, Jerry C. Chen, Isaac L. Chuang, Jay N. Damask, Christopher R. Doerr, David J. Dougherty, James G. Goodberlet, Katherine L. Hall, Michael R. Hee, David Huang, Charles T. Hultgren, Janice M. Huxley, Sumanth Kaushik, Farzana I. Khatri, Joseph M. Jacobson, Yinchieh Lai, Gadi Lenz, John D. Moores, Ann W. Morgenthaler, Martin H. Muendel, Lynn E. Nelson, Janet L. Pan, Malini Ramaswamy, Kohichi R. Tamura, Morrison Ulman

Undergraduate Students

Michele M. Bierbaum, Irfan U. Chaudhary, Stephen Y. Hon

Technical and Support Staff

Mary C. Aldridge, Donna L. Gale, Cynthia Y. Kopf, Lisbeth N. Lauritzen

1.1 Additive Pulse Modelocking

Sponsors

Joint Services Electronics Program
Contract DAAL03-89-C-0001
Contract DAAL03-92-C-0001
U.S. Air Force - Office of Scientific Research
Contract F49620-91-C-0091

Project Staff

Professor Hermann A. Haus, Professor Erich P. Ippen, Dr. Antonio Mecozzi, Jerry C. Chen, Farzana I. Khatri, John D. Moores, Stephen Y. Hon

Additive Pulse Modelocking (APM) is a technique of mode locking that simulates a fast saturable absorber via nonlinear interferometric action using a Kerr medium. Often this medium is a fiber placed in an auxiliary cavity, but the Kerr effect may be produced in the components internal to the main cavity of the laser. The Kerr Lens Mode-

locking pioneered by Coherent, produces equivalent saturable absorber action by self focusing. A general theory has been developed for both kinds of systems.¹ Its main results are:

1. An analytic treatment of the modelocking process in the presence of self-phase modulation and group velocity dispersion;
2. Criteria for the stability of the modelocked pulses;
3. The condition for self starting of the pulses and the explanation of a power threshold for mode locking.²

The theory is helpful in pointing the way to the generation of shorter pulses with lower fluctuations.

In conjunction with this theory, an analysis of noise in modelocked systems has been carried out.³ This analysis provides an explanation of the observed spectra of the detector current illumi-

¹ H.A. Haus, J.G. Fujimoto, and E.P. Ippen, "Structures for Additive Pulse Modelocking," *J. Opt. Soc. Am. B* 8: 2068-2076 (1991).

² H.A. Haus and E.P. Ippen, "Self Starting of Passively Modelocked Lasers," *Opt. Lett.* 16: 1331-1333 (1991).

³ S. Hon, K. Bergman, A. Mecozzi, and H.A. Haus, "Noise Spectra of Modelocked Laser Pulses," submitted for presentation at CLEO '92, Anaheim, CA (1992).

nated by modelocked pulses observed by many researchers. Stephen Hon has performed extensive measurements of three different laser systems (actively modelocked Nd:YAG, soliton laser, APM Ti:Sapphire laser). We have shown theoretically that the current spectrum reveals not only the amplitude and timing jitter, as heretofore assumed, but also gives information on the correlation between the two. These experiments have been an important guide to the theory. Conversely, the newly developed theory is now being applied to extract full information from the detector current spectra. The fluctuations that are not observable from the current spectrum of direct detection are the phase fluctuations (that give rise to the well-known Schawlow-Townes linewidth) and the carrier frequency fluctuations.

The analysis has also been extended to allow for the inclusion of slow, as well as fast, absorber effects. Such a combination may be used to advantage in lasers where pulse initiation is a problem. There is a trade-off in the range of gain and dispersion over which steady-state stability can be achieved.

1.2 Ultrashort Pulse Fiber Laser

Sponsors

Charles S. Draper Laboratories
Contract DL-H-441629

Joint Services Electronics Program
Contract DAAL03-89-C-0001
Contract DAAL03-92-C-0001

U.S. Air Force - Office of Scientific Research
Contract F49620-91-C-0091

Project Staff

Professor Hermann A. Haus, Professor Erich P. Ippen, Janice M. Huxley, Lynn E. Nelson, Kohichi R. Tamura

High bit-rate optical communication networks and ultrafast optical signal processing systems will require compact, chirp-free picosecond pulse sources. Erbium-doped fiber lasers are prime candidates because of their compatibility with transmission fibers, their operation at 1.5 μm , and their amenability to diode pumping. The nonlinear refractive index effects in these fibers also make them attractive lasers for additive pulse mode-locking (APM). We have therefore constructed an erbium fiber laser with intent to study how APM

may be implemented in an all-fiber device and to optimize ultrashort pulse generation.

In a fiber, the nonlinear interferometric action necessary for APM is most easily achieved through intensity dependent polarization rotation. Thus our laser uses fiber polarizers and polarization controllers in a fiber ring with an erbium amplifying section. Fiber couplers to the ring facilitate pumping (with a Ti:sapphire laser for the time being) and output coupling. Short pulse operation has already been obtained and studied under several operating conditions. Pulse spectra indicate durations as short as 300 fs. Autocorrelation measurements and variations with pumping level indicate that the output consists of strings of pulses quantized by soliton effects. A computer model has been developed that extends our APM theory to cases like this in which pulse shaping effects per round trip are large and cannot be treated perturbationally. This model is now being used to map regions of stability and single pulse operation.

1.3 Long Distance Fiber Communications

Sponsor

MIT Lincoln Laboratory

Project Staff

Professor Hermann A. Haus, Dr. Antonio Mecozzi, Yinchieh Lai, John D. Moores

In 1986, J.P. Gordon and Professor Hermann A. Haus published a paper⁴ pointing out that transatlantic transmission using solitons would suffer from timing jitter of the pulses caused by frequency jitter induced by the spontaneous emission of the amplifier stages. This effect, now called the Gordon-Haus effect, has had an important influence on the planning of the next transatlantic cable of AT&T which will be laid in 1995. This cable will not use solitons, but will operate at (or near) the zero dispersion wavelength of the fiber. It is designed for 5 Gbit transmission and so that future Wavelength Division Multiplexing will not be permitted, at least not when using similar channels shifted in frequency. The reason for this design is that the dynamic range of the input pulse stream of the soliton version of the system is limited by two effects. On one hand, the pulses have to be energetic enough

⁴ J.P. Gordon and H.A. Haus, "Random Walk of Coherently Amplified Solitons in Optical Fiber Transmission," *Opt. Lett.* 11: 665-667 (1986).

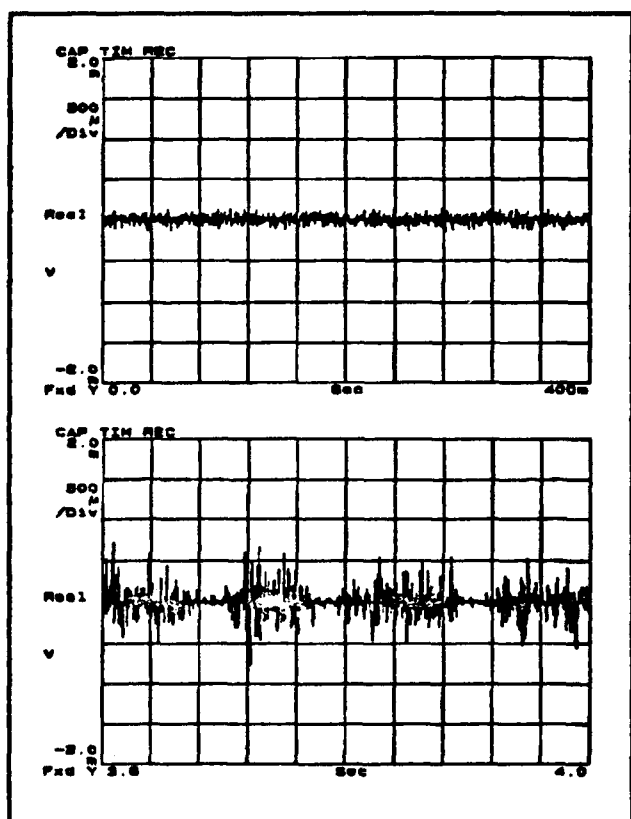


Figure 2.

by keeping its injection current relatively constant. Such structures have achieved wide tuning ranges, but not in a continuous manner.

We are pursuing an alternate approach that relies on the ability of controlling the injection currents into two quantum wells, one on top of the other, by contacts properly fabricated by ion implantation. The two quantum wells are different and have transitions at different frequencies. The respective gain peaks are displaced in frequency, and, along with them, the index characteristics. By controlling the currents injected into the two quantum wells separately, one can control the gain and index independently. Such structures would be ideal for tuning of monolithic resonators at constant gain.

1.7 Gain Dynamics in Semiconductor Amplifiers

Sponsors

Joint Services Electronics Program
Contract DAAL03-89-C-0001
Contract DAAL03-92-C-0001
National Science Foundation
Grant EET 88-15834
U.S. Air Force - Office of Scientific Research
Contract F49620-91-C-0091

Project Staff

Professor Erich P. Ippen, Katherine L. Hall, Gadi Lenz, Dr. Kazunori Naganuma

The potential application of semiconductor amplifiers to wideband communication networks and integrated photonic circuits motivates our studies of these devices. We use femtosecond optical pulses to probe propagation effects in amplifier structures, characterize optical nonlinearities in the gain, and observe fundamental ultrafast carrier dynamics in the semiconductor active layers.

During the past year we have performed the first femtosecond time-domain measurements of group velocity dispersion (GVD) in diode lasers at $1.5 \mu\text{m}$.⁹ The effects of GVD are two-fold: (1) it can distort pulses being transmitted and amplified, and (2) it limits the temporal resolution, or frequency bandwidth, of nonlinear optical interactions. Our measurements, in both bulk and multiple-quantum-well (MQW) samples yield values for $\lambda d^2 n_{\text{eff}} / d\lambda^2$ in the range -0.63 to $0.95 \mu\text{m}^{-1}$ and indicate that intrinsic material dispersion is the dominant factor. In addition, we discovered differences in group velocity between TE and TM modes on the order of 200 fs/mm . These must be accounted for in studies of anisotropic nonlinearities.

We have also demonstrated a new technique for femtosecond pump-probe measurement that makes it possible to use parallel-polarized pump and probe beams even in strictly collinear geometries.¹⁰ The method makes use of acousto-optic frequency shifting and relies on heterodyne detection to distinguish between pump and probe pulses. In experiments with bulk (V-groove) diode amplifiers, we have demonstrated the obser-

⁹ K.L. Hall, G. Lenz, and E.P. Ippen, "Femtosecond Time Domain Measurements of Group Velocity Dispersion in Diode Lasers at $1.5 \mu\text{m}$," *J. Lightwave Tech.*, forthcoming, May 1992.

¹⁰ K.L. Hall, G. Lenz, E.P. Ippen, and G. Raybon, "Heterodyne Pump-Probe Technique for Time-Domain Studies of Optical Nonlinearities in Waveguides," submitted to *Opt. Lett.*

variation of differences due to nonlinear as well as linear anisotropy. Preliminary results have been obtained on strained-layer quantum-well devices which have highly anisotropic gain.

1.8 Ultrafast Optical Kerr Effect in Active Waveguides

Sponsors

National Center for Integrated Photonics
National Science Foundation
Grant EET 88-15834
U.S. Air Force - Office of Scientific Research
Contract F49620-91-C-0091

Project Staff

Professor Erich P. Ippen, David J. Dougherty,
Charles T. Hultgren

Active optical waveguides offer interesting possibilities for performing nonlinear functions in photonic circuits. By varying the injected carrier density one can change not only the linear components of gain and index of refraction but also the nonlinear ones. A particularly interesting regime of operation is that near the point of nonlinear transparency. At that point, an optical pulse traveling through the waveguide neither creates carriers by absorption nor removes carriers by stimulated emission. There is no long-lived change. Yet the optical wavelength is above bandgap and the density of carriers in the medium is high.

In previous studies of gain dynamics in AlGaAs lasers near this point, we discovered a large transient gain nonlinearity which we identified with nonequilibrium carrier heating. The initial purpose of the work described here was to investigate the index of refraction dynamic associated with this gain nonlinearity. We have done so,¹¹ using a time-division interferometric technique originally demonstrated by Professor Fujimoto's group in passive guides. With this technique we have observed the predicted index dynamic in channeled-substrate planar (CSP) AlGaAs diode lasers (Hitachi HLP 1400) biased just below threshold. The dynamic is identified by its approx-

imately 1.7 ps recovery time and positive sign that is consistent with a theoretical calculation for nonequilibrium heating. To our surprise, however, these experiments have also uncovered a faster and even larger index change. We attribute this new component to an above-band optical Stark shift.¹²

Our experiments were performed with orthogonally polarized pump and probe, so that what we measure is n_{21} . The ultrafast Stark-like component has a negative sign, as do below-bandgap values, but an enhanced value of about $-5 \times 10^{-12} \text{cm}^2/\text{W}$. We believe that the resonant enhancement in the active region has contributions from filled states below the laser photon energy as well as from filled states above. A theoretical description of this possibility has now been put forward by Sheik-Bahai.¹³ Such an effect may have application to ultrafast optical switching. It can also provide a new means for studying femtosecond carrier relaxation phenomena in semiconductors.

1.9 Coherent Phonons in Electronic Materials

Sponsors

Joint Services Electronics Program
Contract DAAL03-89-C-0001
Contract DAAL03-92-C-0001
U.S. Air Force - Office of Scientific Research
Contract F49620-91-C-0091

Project Staff

Professor Erich P. Ippen, Tak K. Cheng, Siegfried B. Fleischer

With optical pulses shorter than 100 fs it has become possible to excite and observe in the time domain the coherent oscillation of optical phonons with frequencies up to 10 THz (333cm^{-1}). In collaboration with Professor Dresselhaus' group we have been investigating the application of this possibility to electronic materials. Recently, we have reported that excitation of such phonons is

¹¹ C.T. Hultgren and E.P. Ippen, "Ultrafast Refractive Index Dynamics in AlGaAs Diode Laser Amplifiers," *Appl. Phys. Lett.* 59: 635 (1991).

¹² C.T. Hultgren and E.P. Ippen, "Ultrafast Optical Kerr Effect in Active Semiconductor Waveguides," *Proceedings of the O.S.A. Topical Meeting on Nonlinear Guided-Wave Phenomena*, paper TuB2, Cambridge, England, September 1991.

¹³ M. Sheik-Bahai and E.W. Van Stryland, "Theory of Ultrafast Nonlinear Refraction in Semiconductor Lasers," *Proceedings of the O.S.A. Annual Meeting*, San Jose, California, November 1991, paper TuB4, post-deadline paper.

particularly efficient in certain semimetals and semiconductors (e.g., Bi, Sb, Te and Ti_2O_3).¹⁴

For our experiments we used pulses from a dispersion-balanced colliding-pulse-modelocked (CPM) dye laser, focused to a 2 μm spot. Reflectivity oscillations were observed in these materials with amplitudes of several percent. That is several orders of magnitude larger than can be expected from impulsive stimulated Raman scattering. In each material only one oscillation frequency was observed, the one corresponding to the A_{1g} mode; and the phase of the amplitude was cosinusoidal with respect to excitation at $t=0$. All of these facts are inconsistent with a stimulated Raman mechanism. To explain them, we have proposed a new theory, dubbed displacive excitation of coherent phonons (DECP).¹⁵ It attributes behavior to a rapid displacement of the ion equilibrium coordinates by the electronic excitation.

The temperature dependence of this effect in Ti_2O_3 is particularly interesting. In the range 300 K-570 K dramatic changes take place in Ti_2O_3 with respect to both its lattice and electronic properties, turning it from a semiconductor to a metal. In our femtosecond experiments, we have observed temperature dependent changes in the optical phonon frequency and electronic relaxation rate that are consistent with this transition. On a dynamic basis this may mean that the bandgap and conductivity of the material are being modulated at the 6 THz phonon frequency. Work in progress will test this hypothesis. Higher excitation levels may also make it possible to observe anharmonic lattice dynamics. In recent preliminary experiments with an amplified CPM system we have measured refractive index modulations at the phonon frequency of as much as 15 percent.

1.10 Femtosecond Studies of Superconductivity

Sponsors

Joint Services Electronics Program
Contract DAAL03-89-C-0001
Contract DAAL03-92-C-0001
U.S. Air Force - Office of Scientific Research
Contract F49620-91-C-0091

Project Staff

Professor Erich P. Ippen, Tak K. Cheng, Siegfried B. Fleischer

Femtosecond optical experiments that monitor the rate of hot electron cooling in materials provide an estimate of the strength of the electron-phonon interaction. If one is dealing with BCS-like superconductors, and one knows the electron-phonon spectral density, femtosecond data on the cooling rate can be related directly to T_c . We have been successful in making such determinations in a range of metallic superconductors and in some high- T_c materials.¹⁶ Recently, we have performed the first femtosecond pump-probe experiments on C_{60} and two of its intercalants.

Most of the properties of C_{60} and its intercalants can be explained by treating them as rolled up sheets of graphite. For this reason it is surprising that K_3C_{60} has a superconducting transition temperature (18 K) more than an order of magnitude higher than that of the other graphite intercalation compounds. Determining the reason for this difference may help develop a better understanding of the mechanisms leading to high- T_c .

For our experiments, thin films (1000Å) of C_{60} , K_3C_{60} , and K_6C_{60} were deposited on quartz substrates and encapsulated to prevent contamination. Femtosecond dynamics were induced and observed, in reflectivity and transmission at $\lambda = 630$ nm, using pulses from a colliding-pulse-modelocked (CPM) dye laser. We believe we are monitoring carrier cooling rates and have deduced time constants of 9 ps, 0.2 ps and 0.7 ps for the

¹⁴ T.K. Cheng, J. Vidal, H.J. Zeiger, G. Dresselhaus, M.S. Dresselhaus, and E.P. Ippen, "Mechanism for Displacive Excitation of Coherent Phonons in Sb, Bi, Te, and Ti_2O_3 ," *Appl. Phys. Lett.* 59: 1923 (1991).

¹⁵ H.J. Zeiger, J. Vidal, T.K. Cheng, E.P. Ippen, G. Dresselhaus, and M.S. Dresselhaus, "Theory for Displacive Excitation of Coherent Phonons," *Phys. Rev. B* 45: 768 (1992).

¹⁶ S.D. Brorson, A. Kazeroonian, J.S. Moodera, D.W. Face, T.K. Cheng, E.P. Ippen, M.S. Dresselhaus, and G. Dresselhaus, "Femtosecond Room-temperature Measurement of the Electron-phonon Coupling Constant λ in Metallic Superconductors," *Phys. Rev. Lett.* 64: 2172 (1990); S.D. Brorson, A. Kazeroonian, D.W. Face, G.L. Doll, T.K. Cheng, M.S. Dresselhaus, G. Dresselhaus, E.P. Ippen, T. Venkatesan, X.D. Wu, and A. Inam, "Femtosecond Thermomodulation Study of high- T_c ," *Solid. State Commun.* 74: 1305 (1990).

three samples, respectively. As might be expected, the superconducting sample has the shortest time constant. But the absolute value of the rate, in the context of the material's phonon spectral density, is surprisingly low for a T_c of 18 K. One possible explanation is that electron-phonon coupling is specific to certain types of phonons. This will be investigated by experiments with different material compositions as well as by more detailed studies of these particular intercalants.

1.11 Femtosecond Pulse Generation in Solid State Lasers

Sponsors

Joint Services Electronics Program

Contract DAAL03-89-C-0001

Contract DAAL03-92-C-0001

National Science Foundation

Grant ECS 85-52701

U.S. Air Force - Office of Scientific Research

Contract F49620-88-C-0089

U.S. Navy - Office of Naval Research

Contract N00014-91-C-0084

Project Staff

Dr. Giuseppe Gabetta, Joseph M. Jacobson, David Huang, Malini Ramaswamy, Professor Hermann A. Haus, Professor Erich P. Ippen, Professor James G. Fujimoto

1.11.1 Introduction

Ultrashort pulse laser technology is of primary importance for the development of high speed optical communication and measurement techniques and for studies of ultrafast phenomena. The principle objectives of our research program are the investigation and development of new ultrashort laser pulse generation and measurement techniques. Special emphasis is placed on studies

of solid state ultrashort pulse laser technology. Solid state lasers represent a third generation technology that has several advantages over existing dye-laser technology. Solid state lasers feature lower cost, greater compactness, higher power, and broader tunability. The large gain bandwidths of solid state laser media can support pulse durations in the femtosecond range with wavelength tunability. These features make solid state laser technology a versatile tool for engineering and research applications in ultrafast phenomena.

One of the most promising solid state laser materials that has emerged to date is $\text{Ti:Al}_2\text{O}_3$.¹⁷ The $\text{Ti:Al}_2\text{O}_3$ laser operates at room temperature, has a high energy storage suitable for high power operation, and a broad gain bandwidth with an extremely wide tuning range from 670 to 1000 nm. These features make it an ideal system for femtosecond pulse generation and spectroscopy.

Recently, we have developed and demonstrated a new ultrashort pulse generation technique known as Additive Pulse Modelocking (APM).¹⁸ Self starting, passive modelocking was demonstrated in $\text{Ti:Al}_2\text{O}_3$ and pulse durations of 200 fs were achieved.¹⁹ An APM laser utilizes an external cavity containing a nonlinear element such as an optical fiber to produce a pulse shortening mechanism similar to saturable absorber action. A saturable absorber is a nonlinear element that exhibits greater transmittivity or reflectivity for higher intensities. This nonlinearity produces pulse shortening by enhancing the peak of the pulse compared to the wings.

Our research in modelocked $\text{Ti:Al}_2\text{O}_3$ represented the first demonstration of self starting passive Additive Pulse Modelocking. The self-starting APM system represented a significant advancement because it eliminated the need for a high frequency loss modulation element and thus reduced system complexity and cost. We have extended the self-starting APM technique to modelock diode pumped laser systems and have generated 1.7 ps pulses in a Nd:YAG system and 2 ps pulses in a Nd:YLF system.²⁰

¹⁷ P.F. Moulton, "Spectroscopic and Laser Characteristics of $\text{Ti:Al}_2\text{O}_3$," *J. Opt. Soc. Am. B* 3: 125 (1986).

¹⁸ E.P. Ippen, "Additive Pulse Modelocking," *J. Opt. Soc. Am. B* 6: 1736-1745 (1989); J. Goodberlet, J. Wang, J.G. Fujimoto, and P.A. Schulz, "Femtosecond Passive Modelocked $\text{Ti:Al}_2\text{O}_3$ Laser with a Nonlinear External Cavity," *Opt. Lett.* 14: 1125 (1989).

¹⁹ J. Goodberlet, J. Wang, J.G. Fujimoto, and P.A. Schulz, "Femtosecond Passive Modelocked $\text{Ti:Al}_2\text{O}_3$ Laser with a Nonlinear External Cavity," *Opt. Lett.* 14: 1125 (1989).

²⁰ J. Goodberlet, J. Jacobson, J.G. Fujimoto, P.A. Schulz, and T.Y. Fan, "Self-starting Additive-pulse Mode-locked Diode-pumped Nd:YAG Laser," *Opt. Lett.* 15: 504-506 (1990).

1.11.2 Femtosecond Generation Using Nonlinear Intracavity Elements

Studies by other investigators have recently demonstrated that a single cavity $\text{Ti:Al}_2\text{O}_3$ system can be modelocked without an active modulator, saturable absorber, or nonlinear external cavity.²¹ This phenomena was termed self-modelocking. Although these investigations did not elucidate the short pulse generation mechanisms, they demonstrated that a solid state laser could be modelocked solely by intracavity optical nonlinearities.

Solid state femtosecond lasers such as $\text{Ti:Al}_2\text{O}_3$ can achieve peak intracavity intensities of 0.5 MW when they are modelocked. These high peak intensities make possible a wide range of new modelocking techniques which utilize intracavity nonlinearities. Saturable absorber action based on all-optical solid state refractive index nonlinearities is of particular interest because of its extremely fast response and recovery times. Our group has pursued this approach further and demonstrated two different types of passive modelocking schemes in $\text{Ti:Al}_2\text{O}_3$ using all solid state nonlinear intracavity modulators.²² These modelocking techniques permit the generation of femtosecond pulse durations and can be extended to a wide range of solid state lasers at different wavelengths. In addition, they represent a significant reduction in cost and system complexity over previous modelocking techniques.

One approach for modelocking uses a nonlinear intracavity element which functions by nonlinear polarization rotation. This device is called a Kerr Polarization Modulator (KPM)²³ and consists of a quarter-wave plate, a focusing lens, an SF11 glass plate, a second quarter-wave plate, and a curved

end mirror. The KPM works by generating an elliptical polarization state which undergoes a nonlinear rotation due to the intensity dependent refractive index of the SF11 glass plate. The linear and nonlinear transmission functions of the KPM can be controlled by setting the retardations of the quarter-wave plates. Thus the KPM can be made to have an increasing transmission with increasing intensity and function as a saturable absorber. We have demonstrated this technique for modelocking $\text{Ti:Al}_2\text{O}_3$ and achieved pulse durations of 230 fs.

Another approach for modelocking relies on the use of intracavity self focusing. This technique has been termed Kerr Lens Modelocking (KLM),²⁴ and pulse durations in the 100 fs range have been demonstrated in $\text{Ti:Al}_2\text{O}_3$. KLM produces a fast saturable-like action by using self focusing in the laser rod combined with intracavity aperturing. Research in our group has emphasized developing both a fundamental understanding of the underlying nonlinear processes as well as an approach for engineering these systems. We have introduced a significant simplification in the design of KLM lasers by developing a modular nonlinear intracavity element called a micro-dot mirror.²⁵

The end mirror of the laser is substituted with a focusing lens and a mirror with small diameter micro-dots. The mirror is antireflection (AR) coated on the first surface (i.e., the surface that laser beam first encounters) and high reflection (HR) coated on the second surface. The second surface is patterned into an array of HR spots (micro-dots) with varying diameter using micro-electronic techniques. Fast saturable absorber action is produced by nonlinear self focusing which produces a smaller spot size for higher intensities. When a pulse is reflected from the micro-dot mirror, the higher intensity peaks of the pulse are reflected more than the lower intensity

²¹ D.E. Spence, P.N. Kean, and W. Sibbett, "60-fsec Pulse Generation from a Self-mode-locked Ti:sapphire Laser," *Opt. Lett.* 16: 42 (1991).

²² G. Gabetta, D. Huang, J. Jacobson, M. Ramaswamy, H.A. Haus, E.P. Ippen, and J.G. Fujimoto, "Femtosecond Pulse Generation in $\text{Ti:Al}_2\text{O}_3$ Using Nonlinear Intracavity Elements," CLEO 1991, Baltimore, Maryland, 1991; G. Gabetta, D. Huang, J. Jacobson, M. Ramaswamy, H.A. Haus, E.P. Ippen, and J.G. Fujimoto, "Femtosecond Pulse Generation in $\text{Ti:Al}_2\text{O}_3$ Using a Microdot Mirror Modelocker," *Opt. Lett.* 16: 1756 (1991).

²³ G. Gabetta, D. Huang, J. Jacobson, M. Ramaswamy, H.A. Haus, E.P. Ippen, and J.G. Fujimoto, "Femtosecond Pulse Generation in $\text{Ti:Al}_2\text{O}_3$ Using Nonlinear Intracavity Elements," CLEO 1991, Baltimore, Maryland, 1991.

²⁴ D.K. Negus, L. Spinelli, N. Goldblatt, and G. Feugnet, "Sub-100 Femtosecond Pulse Generation by Kerr Lens Modelocking in $\text{Ti:Al}_2\text{O}_3$," OSA Meeting on Advanced Solid State Lasers, Hilton Head, South Carolina, March 18-20, 1991, postdeadline paper.

²⁵ G. Gabetta, D. Huang, J. Jacobson, M. Ramaswamy, H.A. Haus, E.P. Ippen, and J.G. Fujimoto, "Femtosecond Pulse Generation in $\text{Ti:Al}_2\text{O}_3$ Using a Microdot Mirror Modelocker," *Opt. Lett.* 16: 1756 (1991); D. Huang, M. Ullman, L. Acioli, H.A. Haus, and J.G. Fujimoto, "Self-focusing Induced Saturable Absorber Loss for Laser Mode Locking," *Opt. Lett.*, forthcoming.

wings of the pulse. Thus the micro-dot mirror effectively acts as a fast saturable absorber. We have demonstrated the micro-dot mirror for modelocking the $\text{Ti:Al}_2\text{O}_3$ laser and achieved pulse durations of 190 fs.

The modelocking techniques described above have led to a better understanding of passive modelocking mechanisms in solid state laser systems. In the case of self-focusing modelocking, we developed a new theoretical framework which is applicable to the majority of single cavity passively modelocked $\text{Ti:Al}_2\text{O}_3$ systems.²⁶ Theoretical studies are important not only for understanding pulse shortening mechanisms but also for investigating factors which limit pulse duration.

We have developed an analytical description of modelocking which includes fast saturable absorption, self phase modulation, gain bandwidth limiting, and dispersion. A pulse in a modelocked laser can be mathematically described by a single equation similar to the nonlinear Schrodinger equation. We have studied the behavior of pulse characteristics such as pulse duration, chirp, bandwidth, and stability.²⁶ Our primary findings show that there are two basic operating regimes where stable short pulse generation may be achieved. A laser may be constructed either with positive (normal) or negative (anomalous) dispersion. The pulse shaping mechanisms for these two regimes are different and a laser that has anomalous dispersion will in general produce dramatically shorter pulses than one with normal dispersion. These results suggest design criteria for a wide range of modelocked solid state lasers.

1.11.3 Reduction of Pulse Duration by Dispersion Compensation

One of the key topics of investigation in ultrashort pulse generation is the development of approaches for generating the shortest possible pulse durations. The fundamental limit to pulse duration is determined by the energy-time uncertainty principle which implies that the pulse duration is inversely related to the laser gain bandwidth. The gain bandwidth in $\text{Ti:Al}_2\text{O}_3$ is in excess of 100-200 nm²⁷ and thus pulse durations of a few femtoseconds are theoretically possible. Pulse compression techniques using amplified femtosecond pulses have been demonstrated to achieve pulses as short as 6 fs.²⁸ However, pulses in the 10 fs range have not as yet been generated directly from a laser. The broad bandwidths associated with these pulse durations allow the use of frequency synthesis techniques to control pulse shape or generate multiple pulse, multiple wavelength pulse trains.²⁹ Thus, the development of new sources with pulse durations in the 10 fs range would have a major impact on the study of ultrafast phenomena.

One area of investigation in our program is the exploration of the factors which limit the short pulse duration that can be generated. The theoretical considerations discussed above are valid only in systems where the pulses are long enough that dispersive terms higher than those of second order can be neglected. Previous pulse compression studies have demonstrated that higher order dispersion presents an important limitation to pulse duration as pulses become very short and their corresponding frequency bandwidths become broad.³⁰

In order to explore and extend the limits of short pulse generation, we have developed and demonstrated a solid state laser with independently adjustable second and third order dispersion. Compensation of dispersion is achieved using a pair of intracavity prisms which are set to produce a net negative second order dispersion in the

²⁶ H.A. Haus, J.G. Fujimoto, and E.P. Ippen, "Structures for Additive Pulse Modelocking," *J. Opt. Soc. Am. B* 8: 2068 (1991).

²⁷ P.F. Moulton, "Spectroscopic and Laser Characteristics of $\text{Ti:Al}_2\text{O}_3$," *J. Opt. Soc. Am. B* 3: 125 (1986).

²⁸ R.L. Fork, C.H. Brito Cruz, P.C. Becker, and C.V. Shank, "Compression of Optical Pulses to Six Femtoseconds by Using Cubic Phase Compensation," *Opt. Lett.* 12: 483 (1987).

²⁹ A.M. Weiner, J.P. Heritage, and E.M. Kirschner, "High-resolution Femtosecond Pulse Shaping," *J. Opt. Soc. Am. B* 5: 1563 (1988).

³⁰ W.J. Tomlinson and W.H. Knox, "Limits of Fiber-grating Optical Pulse Compression," *J. Opt. Soc. Am. B* 4: 1404 (1987); C.H. Brito Cruz, P.C. Becker, R.L. Fork, and C.V. Shank, "Phase Correction of Femtosecond Optical Pulses Using a Combination of Prisms and Gratings," *Opt. Lett.* 13: 123 (1988).

cavity. Intracavity prisms are a standard technique for dispersion compensation which have been applied to a number of solid state and dye lasers. An undesirable consequence of this prism arrangement, however, is that it also introduces a significant negative third order dispersive term which produces pulse distortion effects.³⁰ In order to explicitly compensate for third order dispersion, we have developed an intracavity thin film element which has positive third order dispersion but zero second order dispersion. Working in collaboration with investigators at CVI Incorporated, we designed and fabricated a thin film Gires-Tourneau Interferometer (GTI) on a mirror substrate. The amount of third order compensation introduced in the laser cavity can be varied by adjustment of the number of times the pulse bounces off each GTI surface during each round trip. This is the first laser that has directly adjustable second and third order dispersion. Using this technique we have generated pulse durations as short as 28 fs directly from a modelocked $\text{Ti:Al}_2\text{O}_3$ laser. These pulses are the shortest pulses which have been directly generated from a $\text{Ti:Al}_2\text{O}_3$ laser without using pulse compression techniques.³¹

1.12 Studies of Ultrafast Phenomena in Optoelectronic Materials

Sponsors

Joint Services Electronics Program
 Contract DAAL03-89-C-0001
 Contract DAAL03-92-C-0001
 National Science Foundation
 Grant ECS 85-52701
 U.S. Air Force - Office of Scientific Research
 Contract F49620-88-C-0089
 U.S. Navy - Office of Naval Research
 Grant N00014-91-J-1956

Project Staff

Dr. Lucio H. Acioli, Morrison Ulman, David Huang,
 Professor Erich P. Ippen, Professor James G. Fujimoto

1.12.1 Four Wave Mixing and Temporal Encoding in Barium Titanate

The idea of optically encoding information in photosensitive materials is relevant to applications in optical signal processing, image processing, and optical logic. Holography is an example of a technique in which three-dimensional spatial information can be recorded in a suitable matrix such as film or photorefractive material. In addition to spatial information, temporal information may also be encoded. The search for systems to record information in the temporal domain have usually been based on the concept of encoding information using inhomogeneously broadening transitions in atomic systems. The techniques most often applied for temporal storage have been variations of photon echo like schemes. Working in collaboration with investigators from Tufts University, we have performed the first studies of femtosecond wave-mixing in BaTiO_3 and demonstrated the possibility of using volume holography for recording temporal information.³²

Photorefractive materials such as BaTiO_3 , or SBN, have been demonstrated for a wide range of optical phase conjugation and signal processing experiments using continuous wave lasers.³³ These materials exhibit extremely large nonlinearities, and studies can be performed without the need for high laser intensities. However, the response and relaxation times of the photorefractive materials are extremely slow, and thus only recently has the use of such materials under pulsed laser excitation been considered. In order to circumvent the slow material response, our technique records temporal information in the spatial domain using four wave mixing and modulated volume photorefractive gratings.

Experiments were performed using a colliding pulse modelocked, CPM, dye laser source which generated 40 fs pulse durations. Temporal information was encoded using a signal and a reference beam. When the signal and reference beams interact in the photorefractive crystal, they form a

³¹ J.M. Jacobson, A.G. Jacobson, K. Naganuma, and J.G. Fujimoto, "Generation of 28 fs Pulses from a TiAl_2O_3 Laser Using Second and Third Order Intracavity Dispersion Compensation," paper to be presented at CLEO 1992, Anaheim, California.

³² L.H. Acioli, M. Ulman, E.P. Ippen, J.G. Fujimoto, H. Kong, B.S. Chen, and M. Cronin-Golomb, "Femtosecond Temporal Encoding in Barium Titanate," *Opt. Lett.* 16: 1984 (1991).

³³ M. Cronin-Golomb, B. Fischer, J.O. White, and A. Yariv, "Theory and Applications of Four-wave Mixing in Photorefractive Media," *IEEE J. Quant. Electron.* QE-20: 12 (1984).

standing wave interference pattern where they geometrically overlap. This in turn induces a photorefractive diffraction grating. If the signal beam contains a femtosecond temporal waveform, and the reference beam consists of a single femtosecond pulse, a spatially varying interference pattern will be formed according to the geometrical overlap of the signal and the reference optical waveforms. The temporal information on the signal beam is recorded as a volume grating in the BaTiO₃ crystal. The photorefractive gratings have a long persistence time and can be used to store the temporal information. The femtosecond waveform can subsequently be reconstructed by diffracting a femtosecond reference pulse from the stored volume grating.³⁴ This process is analogous to image reconstruction in holography.

Different phase conjugation geometries were examined including the ring resonator and the two beam coupling geometry. A surprising discovery was that temporal signals are influenced only by material dispersion effects and that pulse durations of 40 fs could be preserved. We have determined that the factors that influence the temporal resolution of the temporal encoding and reconstruction process and developed a simple geometrical model to predict resolution and information storage capacity. Our experiments are closely related to femtosecond holography which uses holographic recording to store transient femtosecond images,³⁵ except that our results demonstrate an extension of this technique to both the storage and reconstruction of temporal information. Variations of our approach using acousto-optic modulators or other programmable volume diffraction devices could make possible the generation of programmable optical pulses at THz repetition rates.

1.12.2 Self-Focusing and Nonlinear Propagation

Nonlinear optical media with Kerr-like refractive index nonlinearities are relevant to a wide range of applications including all-optical switching, optical modulation, short pulse generation, and short pulse propagation in optical fibers. Self-focusing is a classic nonlinear optical process which has been the subject of investigation for many years. This process has been of interest in previous studies because it poses a limitation to high power laser generation. Recently, however, self-focusing has become technologically important for applications which involve high speed all-optical modulation and short pulse generation. A new technique for modelocking solid state lasers, called Kerr lens modelocking has been developed which uses self focusing to achieve fast saturable absorber action.³⁶ Pulse durations of less than 100 fs have been achieved in the Ti:Al₂O₃ laser. Self-focusing also plays a major role in other short pulse generation techniques such as high power femtosecond pulse compression and continuum generation.³⁷

Self-focusing is produced by the intensity dependent nonlinear index of refraction of the material and the spatial intensity variation of the laser beam. The transverse spatial intensity variation of the beam induces a graded index lens in the nonlinear material which, in turn, produces a geometric focusing of the beam. Several researchers have studied this problem in the past, and, with the advent of high intensity femtosecond lasers, a description of the temporal as well as the spatial behavior of self-focusing has become of interest. There is no theory yet that fully describes the problem of nonlinear femtosecond pulse propagation in bulk nonlinear media.

Our investigations of self-focusing are directed toward applications in laser modelocking and short pulse generation. Self-focusing has recently been used to achieve fast saturable absorber mode-

³⁴ L.H. Acioli, M. Ulman, E.P. Ippen, J.G. Fujimoto, H. Kong, B.S. Chen, and M. Cronin-Golomb, "Femtosecond Temporal Encoding in Barium Titanate," *Opt. Lett.* 16: 1984 (1991).

³⁵ J.A. Valdmanis, H. Chen, E.N. Leith, Y. Chen, and J.L. Lopez, "Three Dimensional Imaging with Femtosecond Optical Pulses," *CLEO Technical Digest paper CTUA1*, 1990, p. 54.

³⁶ D.K. Negus, L. Spinelli, N. Goldblatt, and G. Feugnet, "Sub-100 Femtosecond Pulse Generation by Kerr Lens Modelocking in Ti:Al₂O₃," OSA Meeting on Advanced Solid State Lasers, Hilton Head, South Carolina, March 18-20, 1991, postdeadline paper.

³⁷ C. Rolland and P.B. Corkum, "Compression of High-power Optical Pulses," *J. Opt. Soc. Am. B* 5: 641 (1988); D.H. Reitze, A.M. Weiner, and D.E. Leaird, "High-power Femtosecond Optical Pulse Compression by Using Spatial Solitons," *Opt. Lett.* 16: 1409 (1991); R.L. Fork, C.V. Shank, C. Hirlimann, R. Yen, and W.J. Tomlinson, "Femtosecond White-light Continuum Pulses," *Opt. Lett.* 8: 1 (1983).

locking in $\text{Ti:Al}_2\text{O}_3$. This process has been termed Kerr Lens Modelocking and can form the basis for ultrashort pulse generation in a wide range of solid state lasers.³⁸ As discussed previously, we have developed a modular device called a micro-dot mirror which uses self-focusing to modelock the $\text{Ti:Al}_2\text{O}_3$ laser.³⁹ In addition, self-focusing in bulk materials can also be used for short pulse generation and nonlinear measurement. High power pulse compression has been demonstrated using self phase modulation in bulk nonlinear materials.⁴⁰ It has also been shown that self-focusing plays a fundamental role in the process of continuum generation with femtosecond pulses and can be used to generate spatial optical solitons for pulse compression.⁴¹ An experimental technique, based on the self-focusing effect and referred to as "z-scan,"⁴² has been introduced as a sensitive probe of the magnitude of the nonlinear refractive index.

In order to investigate the use of self-focusing for modelocking and ultrashort pulse propagation, we have developed a new approach to describe the effects of self-focusing in thick (compared to the confocal parameter of the beam) nonlinear media.⁴³ This method is based on a complex scaling operation applied to the q parameter of a gaussian beam. Self-focusing can be described in the perturbative limit using a compact formulation that is compatible with the ABCD matrix description of gaussian beam propagation. Experimental "z-scan" measurements of self-focusing were performed using a femtosecond CPM (col-

liding pulse modelocked) dye laser and high repetition rate copper vapor laser pumped amplifier.⁴⁴ Excellent agreement between the theoretical predictions and the experimental results have been obtained for thick optical glasses (BK7 and fused silica). These theoretical and experimental studies provide a basis for designing and developing Kerr lens modelocking techniques in a wide range of solid state lasers.

We have also studied the effects of self-focusing in continuum generation. Our investigations use variations of the "z-scan" technique⁴⁵ in order to quantify the continuum generation process by varying the nonlinear propagation parameters of the beam. Our current studies focus on describing energy transfer to wavelengths different from that of the input beam, the amplitude stability, and the divergence properties of the output beam. An increased understanding of these processes can form the basis for developing new short pulse generation techniques based on nonlinear propagation.

1.12.3 Femtosecond Carrier Dynamics in Semiconductors

The efficient design of high speed electronic and photonic devices requires a detailed understanding of transient carrier dynamics in semiconductor materials. The dynamics of electrons and holes determine fundamental limitations to device speed. For example, intervalley scattering processes affect

³⁸ D.K. Negus, L. Spinelli, N. Goldblatt, and G. Feugnet, "Sub-100 Femtosecond Pulse Generation by Kerr Lens Modelocking in $\text{Ti:Al}_2\text{O}_3$," OSA Meeting on Advanced Solid State Lasers, Hilton Head, South Carolina, March 18-20, 1991, postdeadline paper.

³⁹ G. Gabetta, D. Huang, J.M. Jacobson, M. Ramaswamy, E.P. Ippen, and J.G. Fujimoto, "Femtosecond Pulse Generation in $\text{Ti:Al}_2\text{O}_3$ Using a Microdot Mirror Mode Locker," *Opt. Lett.* 16: 1756 (1991).

⁴⁰ C. Rolland and P.B. Corkum, "Compression of High-power Optical Pulses," *J. Opt. Soc. Am. B* 5: 641 (1988); D.H. Reitze, A.M. Weiner, and D.E. Leaird, "High-power Femtosecond Optical Pulse Compression by Using Spatial Solitons," *Opt. Lett.* 16: 1409 (1991).

⁴¹ D.H. Reitze, A.M. Weiner, and D.E. Leaird, "High-power Femtosecond Optical Pulse Compression by Using Spatial Solitons," *Opt. Lett.* 16: 1409 (1991); R.L. Fork, C.V. Shank, C. Hirlimann, R. Yen, and W.J. Tomlinson, "Femtosecond White-light Continuum Pulses," *Opt. Lett.* 8: 1 (1983).

⁴² M. Sheik-Bahae, A.A. Said, T. Wei, D.J. Hagan, and E.W. Van Stryland, "Sensitive Measurement of Optical Nonlinearities Using a Single Beam," *IEEE J. Quant. Electron.* 26: 760 (1990).

⁴³ D. Huang, M. Ullman, L. Acioli, H.A. Haus, and J.G. Fujimoto, "Self-focusing Induced Saturable Absorber Loss for Laser Mode Locking," *Opt. Lett.*, forthcoming.

⁴⁴ R.L. Fork, C.V. Shank, C. Hirlimann, R. Yen, and W.J. Tomlinson, "Femtosecond White-light Continuum Pulses," *Opt. Lett.* 8: 1 (1983).

⁴⁵ M. Sheik-Bahae, A.A. Said, T. Wei, D.J. Hagan, and E.W. Van Stryland, "Sensitive Measurement of Optical Nonlinearities Using a Single Beam," *IEEE J. Quant. Electron.* 26: 760 (1990).

the high field transport behavior of GaAs devices.⁴⁶ Carrier dynamics have been studied with a number of techniques including luminescence spectroscopy and femtosecond absorption saturation.⁴⁷ Our research program combines state-of-the-art experimental and theoretical approaches to develop an accurate model for carrier dynamics on an ultrashort timescale. The ultrahigh temporal resolution of femtosecond lasers permits direct measurement of electronic scattering processes that occur in less than 100 femtoseconds. Carrier scattering events may be examined both experimentally and by supercomputer simulation. As a result of these investigations, transient electronic behavior in a variety of important semiconductor materials and quantum structures may be predicted. Recently, we have focused our efforts on intervalley scattering in AlGaAs as a paradigm for investigating femtosecond carrier dynamics.

Our research program is a collaborative effort with Professor C.J. Stanton's solid state theory group at the University of Florida. The objective of the theoretical component of the program is to develop both numerical simulation and analytical methods which establish a correspondence between experimental femtosecond transient absorption saturation results and theoretical models. The problem of investigating transient carrier dynamics in III-V semiconductors is extremely complicated because of the large number of scattering processes. Thus, advanced theoretical techniques such as Ensemble Monte Carlo theory are necessary to accurately interpret experimental results. A full zone, 30 band, empirical $k \cdot p$ procedure is used to determine the relevant electronic bandstructure. A Monte Carlo simulation of 40,000 electrons and holes tracks the time development of the electron and hole distribution functions. Finally, the differential transmission is calculated and compared directly to the results of femtosecond pump-probe experiments.⁴⁸ In this way, fundamental material parameters such as deformation potential constants and carrier-carrier scattering rates may be

determined. An analytic discretization of the Boltzmann equation combined with a rate equation approach has also been developed to provide intuitive insight into the transient carrier relaxation process. This interdisciplinary approach has already shown that collisional broadening and femtosecond hole redistribution must be included in the theory in order to match the experimental results. We are now investigating the role of carrier diffusion and coulomb enhancement on the differential transmission data.

In the past year, work at MIT has been directed toward femtosecond pump-probe absorption saturation studies of the GaAs and AlGaAs semiconductor systems. Femtosecond intervalley scattering in AlGaAs is investigated using a tunable wavelength technique. Systematic variation of the wavelength and spectral content of ultrashort laser pulses permits a selective study of different scattering channels, such as scattering to the L satellite valley. An amplified colliding pulse modelocked (CPM) ring dye laser system provides the source for our experiments. Femtosecond optical pulses from the CPM are amplified by a copper vapor laser pumped dye amplifier to microjoule energies. The amplified pulses are focused on a jet of ethylene glycol to generate a femtosecond white light continuum using nonlinear self phase modulation. A Fourier synthesis scheme selects variable wavelengths and pulse durations for use in pump-probe experiments.⁴⁹ This approach has the advantage that it permits studies using wavelength tunable pulses with durations as short as 30 fs. The samples used in our studies are grown by molecular beam epitaxy at MIT Lincoln Laboratory. The mole fraction of Al in the $\text{Al}_x\text{Ga}_{1-x}\text{As}$ system is chosen to vary the bandstructure and isolate optical transitions of interest. Scattering to the L valley in $\text{Al}_{0.1}\text{Ga}_{0.9}\text{As}$ is only allowed for photoexcited carriers with energy greater than 1.8 eV. The possibility of scattering by this channel affects the behavior of the transient in femtosecond absorption saturation.

⁴⁶ M.A. Littlejohn, J.R. Hauser, T.H. Glisson, D.K. Ferry, and J.W. Harrison, "Alloy Scattering and High Field Transport in Ternary and Quaternary III-V Semiconductors," *Solid State Electron.* 21: 107 (1978).

⁴⁷ S.A. Lyon, "Spectroscopy of Hot Carrier in Semiconductors," *J. Lumines.* 35: 121-154 (1986); J. Shah, B. Deveaud, T.C. Damen, and W.T. Tsang, "Determination of Intervalley Scattering Rates in GaAs by Subpicosecond Luminescence Spectroscopy," *Phys. Rev. Lett.* 59: 2222-2225 (1987); R.G. Ulbrich, J.A. Kash, and J.C. Tsang, "Hot-electron Recombination at Neutral Acceptors in GaAs: A cw Probe of Femtosecond Intervalley Scattering," *Phys. Rev. Lett.* 62: 949-952 (1989); P.C. Becker, H.L. Fragnito, C.H. Brito Cruz, R.L. Fork, J.E. Cunningham, J.E. Henry, and C.V. Shank, "Femtosecond Intervalley Scattering in GaAs," *Appl. Phys. Lett.* 53: 2089-2090 (1988).

⁴⁸ C.J. Stanton and D.W. Bailey, "Evaluating Photoexcitation Experiments Using Monte Carlo Simulations," in *Monte Carlo Simulations of Semiconductors and Semiconductor Devices*, ed. K. Hess (Boston: Klunk Academic, 1991).

⁴⁹ A.M. Weiner, J.P. Heritage, and E.M. Kirschner, "High Resolution Femtosecond Pulse Synthesis," *J. Opt. Soc. Am. B* 5: 1563 (1988).

Thus, a wavelength tunable study discerns salient features of the data in both the time and energy dimensions.

The results already obtained will be extended to new materials systems and to quantum confined structures. Device design in the future will depend on thorough knowledge of the transient electronic properties of semiconductor materials. The combination of advanced femtosecond laser technology with sophisticated theoretical methods provides a potent tool for discovery of fundamental information on ultrafast carrier dynamics.

1.13 Time Domain Diagnostics of Waveguide Devices

Sponsors

Joint Services Electronics Program
Contract DAAL03-89-C-0001
Contract DAAL03-92-C-0001

National Science Foundation
Grant ECS 85-52701

U.S. Air Force - Office of Scientific Research
Contract F49620-88-C-0089

Project Staff

Claudio D.C. Chamon, Chi-Kuang Sun, Professor
Hermann A. Haus, Professor James G. Fujimoto

1.13.1 Time Domain Interferometry

Investigations of nonlinear processes such as measurements of the nonlinear index of refraction in waveguide devices are key to the development of high speed all-optical switching devices. In particular, the magnitude of the nonlinear index is an important parameter for all-optical switching and modulation, since it determines the laser pulse energy which is necessary to achieve switching behavior. Time domain measurements permit both the magnitude as well as the dynamics of the nonlinear index of refraction to be characterized. Previous investigators have used a number of time or frequency domain techniques to measure nonlinear index including four wave mixing,⁵⁰ nonlinear waveguide couplers,⁵¹ nonlinear Fabry-Perots,⁵² fringe shift interferometry,⁵³ and Mach-Zehnder interferometry.⁵⁴ In general, direct measurements of index nonlinearities are complicated because measurement techniques are sensitive to thermal or acoustical parasitic signals, have low sensitivity, or require deconvolution.

Recently, we have developed a new technique, femtosecond time division interferometry (TDI), that permits high sensitivity, direct measurements of the nonlinear index n_2 in waveguide devices with reduced interference from thermal or acoustical parasitic signals.⁵⁵ In this technique, pump and probe pulses are coupled into a waveguide device and the nonlinear phase shift which is induced on the probe by the pump is measured by interfering it with a reference pulse. TDI was previously limited to measurements of $n_{2\perp}$, i.e., index changes induced on a probe pulse by an orthogonally polarized pump. However, new materials such as quantum wells, quantum wires, organic polymers as well as other anisotropic systems are

⁵⁰ W.K. Burns and N. Bloembergen, "Third-harmonic Generation in Absorbing Media of Cubic or Isotropic Symmetry," *Phys. Rev. B* 4: 3437 (1971).

⁵¹ P. Li, K. Wa, J.E. Sitch, N.J. Mason, J.S. Roberts, and P.N. Robson, "All Optical Multiple-quantum-well Waveguide Switch," *Electron. Lett.* 21: 27 (1985).

⁵² Y.H. Lee, A. Chavez-Pirson, S.W. Koch, H.M. Gibbs, S.H. Park, J. Morhange, A. Jeffrey, N. Peyghambarian, L. Banyai, A.C. Gossard, and W. Wiegmann, "Room Temperature Optical Nonlinearities in GaAs," *Phys. Rev. Lett.* 57: 2446 (1986).

⁵³ G.R. Olbright and N. Peyghambarian, "Interferometric Measurement of the Nonlinear Index of Refraction, n_2 , of $\text{CdS}_x\text{Se}_{1-x}$ -doped Glasses," *Appl. Phys. Lett.* 48: 1184 (1986).

⁵⁴ D. Cotter, C.N. Ironside, B.J. Ailsie, and H.P. Girdlestone, "Picosecond Pump Probe Interferometric Measurement of Optical Nonlinearity in Semiconductor Doped Fibers," *Opt. Lett.* 14: 317 (1989).

⁵⁵ M.J. LaGasse, K.K. Anderson, H.A. Haus, and J.G. Fujimoto, "Femtosecond All-optical Switching in AlGaAs Waveguides Using a Single Arm Interferometer," *Appl. Phys. Lett.* 54: 2068 (1989); M.J. LaGasse, K.K. Anderson, C.A. Wang, H.A. Haus, and J.G. Fujimoto, "Femtosecond Measurements of the Nonresonant Nonlinear Index in AlGaAs," *Appl. Phys. Lett.* 56: 417 (1990).

becoming increasingly important candidates for all optical switching devices. A complete characterization of n_2 requires the measurement of n_{21} .

During the past year, we have developed a new variation of our original time division interferometry, TDI, technique which permits the complete characterization of the nonlinear index.⁵⁶ By using a novel phase modulation technique which breaks the degeneracy between the pump and probe and actively stabilizes the interferometer, the magnitude and femtosecond transient response of n_{21} can be measured. Experiments have been performed to measure $n_{2\perp}$ and $n_{2\parallel}$ in an optical fiber to demonstrate this new measurement technique. High sensitivities have also been achieved and phase shifts as small as 5 mrad can easily be detected. Thus, TDI can be applied to studies of nonlinear index and all-optical switching in a wide range of waveguide devices.

1.13.2 Time Domain Diagnostics of Strained Layer Devices

Strained layer quantum well devices represent one of the most active and technologically promising areas of current optoelectronics device research. Strained layer materials greatly extend the available wavelength range of optoelectronic devices by permitting the growth of non-lattice materials. In addition, strained layer materials represent a bandgap engineering approach to achieve superior device performance. By modifying the valence band structure, lower threshold current density, higher efficiency, smaller chirp, wider modulation bandwidth, and improved high temperature performance⁵⁷ can be achieved over conventional devices.⁵⁸ High power, high efficiency, long lifetime, and low threshold current density⁵⁹ semicon-

ductor lasers have been achieved in InGaAs strained layer devices. With their extended wavelength range and high output power, InGaAs/GaAs strained layer lasers are important for applications such as coherent optical communications, pumping erbium doped fiber amplifier and solid state lasers, and high speed optical signal processing.

With the development of new tunable femtosecond laser source of wavelengths between 900 and 1000 nm, time domain diagnostics can become a powerful tool for characterizing dispersion, gain dynamics, nonlinear index change, and transient nonlinearities. We have recently begun a program in collaboration with Groups 67 and 83 at Lincoln Laboratory to develop frequency and time domain diagnostics of strained layer diode lasers. The objective of our program is twofold: To develop and demonstrate new time and frequency domain diagnostics of diode lasers, and to examine fundamental processes and device design issues which limit high power single frequency performance in strained layer diodes.

Studies will involve InGaAs/GaAs graded-index separate-confinement heterostructure strained layer single quantum well laser diodes.⁶⁰ Femtosecond pump probe measurements of gain dynamics, nonlinear index, and dispersion are being performed. Continuous wave measurements such as linewidth, spectral character, self heterodyne four wave mixing, and injection locking are being performed at Lincoln Laboratory. These two approaches represent complementary techniques which, taken together, can permit a more comprehensive characterization of device and materials properties. When completed, this study should establish new approaches for performing time domain diagnostics on a wide range of devices as well as provide

⁵⁶ C. de C. Chamon, C. K. Sun, H.A. Haus, and J.G. Fujimoto, "Femtosecond Time Division Interferometry Technique for Measuring the Tensor Components of $\chi^{(3)}$," *Appl. Phys. Lett.*, forthcoming.

⁵⁷ N.K. Dutta, J. Lopata, D.L. Sivco, and A.Y. Cho, "Temperature Dependence of Threshold of Strained Quantum Well Lasers," *Appl. Phys. Lett.* 58: 1125 (1991).

⁵⁸ E. Yablonovitch and E.O. Kane, "Reduction of Lasing Threshold Current Density by the Lowering of Valence Band Effective Mass," *J. Lightwave Technol.* LT-4: 504 (1986); A.R. Adams, "Band-structure Engineering for Low-threshold High-efficiency Semiconductor Lasers," *Electron. Lett.* 22: 249 (1986); I. Suemune, L.A. Coldren, M. Yamanishi, and Y. Kan, "Extremely Wide Modulation Bandwidth in a Low Threshold Current Strained Quantum Well Laser," *Appl. Phys. Lett.* 53: 1378 (1988).

⁵⁹ H.K. Choi and C.A. Wang, "InGaAs/AlGaAs Strained Single-quantum-well Diode Lasers with Extremely Low Threshold Current Density and High Efficiency," *Appl. Phys. Lett.* 57: 321 (1990); R.L. Williams, M. Dion, F. Chatenoud, and K. Dzurko, "Extremely Low Threshold Current Strained InGaAs/AlGaAs Lasers by Molecular Beam Epitaxy," *Appl. Phys. Lett.* 58: 1816 (1991).

⁶⁰ H.K. Choi and C.A. Wang, "InGaAs/AlGaAs Strained Single-quantum-well Diode Lasers with Extremely Low Threshold Current Density and High Efficiency," *Appl. Phys. Lett.* 57: 321 (1990).

information relevant to optimizing high power device performance in the InGaAs/GaAs system.

1.14 Laser Medicine and Surgery

Sponsors

Johnson and Johnson Research Grant
National Institutes of Health
Contract 2-R01-GM35459
U.S. Navy - Office of Naval Research
Contract N00014-91-C-0084

Project Staff

Dr. Joseph A. Izatt, Dr. Charles P. Lin, David Huang, Michael R. Hee, Professor James G. Fujimoto

1.14.1 The Ultrashort Pulse Laser Scalpel

In recent years, the use of short optical pulses has enhanced the degree of control and localizability of intraocular laser surgery.⁶¹ Laser induced optical breakdown is a nonlinear laser tissue interaction which permits the photodisruption or cutting of transparent structures within the eye without the need for intervening surgical incision. The objective of our program is to develop an optimized ultrashort pulse laser scalpel which can be used to perform surgical incisions of intraocular structures even in close proximity to sensitive ocular structures such as the retina and cornea. These studies are part of an ongoing collaboration between investigators at MIT, the New England Eye Center of New England Medical Center Hospitals, and the Wellman Laboratories of Photomedicine at Massachusetts General Hospital.

The physical processes which occur in laser induced breakdown include plasma formation,

acoustic wave generation, and cavitation. These processes produce the laser tissue surgical effects as well as collateral damage. To date, the majority of clinical applications of laser induced optical breakdown have utilized nanosecond duration pulses in the millijoule energy range and single pulse exposures. We have studied and compared the mechanisms, scaling behavior, and tissue effects of single pulses in the nanosecond and picosecond ranges.⁶² In general, nanosecond and picosecond optical breakdown results in comparable damage zones if the same amount of energy is deposited; however, since the threshold energy for breakdown is much lower for picosecond pulses, near-threshold picosecond pulses produce greatly reduced collateral damage zones. For example, we have demonstrated collateral damage ranges in a corneal endothelial cell model of only 100 μm with 40 picosecond duration pulses at 8 microjoules pulse energy. We have also studied tissue effects (corneal excisions) into the femtosecond domain.⁶³ Ultrashort pulses with high peak intensities can produce a plasma mediated ablation of transparent tissues such as the cornea. Picosecond and femtosecond pulse durations have been demonstrated to produce much smoother excision edges and less damage to the adjacent tissue than nanosecond pulses.

We have demonstrated that clinically viable surgical incisions can be made using multiple pulse, high repetition rate picosecond pulses. Each pulse produces minimal collateral damage while multiple exposures produce a cumulative incision effect. In order to study the effect of repetition rate, we have developed a new Nd:YAG laser system which produces 100 picosecond duration pulses with a maximum energy of 140 μJ and a repetition rate variable from 3 to 1000 Hz. This laser has been used to demonstrate in vitro cutting of a monolayer of cultured fibroblast cells suspended over corneal endothelium in saline as a model for vitreous membrane surgery. Membrane cutting in the deep vitreous in close proximity to the retina remains one of the most challenging problems for

⁶¹ F. Fankhauser, P. Roussel, J. Steffen, E. Van der Zypen, and A. Cherenkova, "Clinical Studies on the Efficiency of High Power Laser Radiation Upon Some Structures of the Anterior Segment of the Eye," *Int. Ophthalmol.* 3: 129 (1981).

⁶² J.G. Fujimoto, W.Z. Lin, E.P. Ippen, C.A. Puliafito, and R.F. Steinert, "Time Resolved Studies of Nd:YAG Laser Induced Breakdown," *Invest. Ophthalm. Vis. Sci.* 26: 1771 (1985); B. Zysset, J.G. Fujimoto, and T.F. Deutsch, "Time Resolved Measurements of Picosecond Optical Breakdown," *Appl. Phys. B* 48: 139 (1989); B. Zysset, J.G. Fujimoto, C.A. Puliafito, R. Birngruber, and T.F. Deutsch, "Picosecond Optical Breakdown: Tissue Effects and Reduction of Collateral Damage," *Lasers Surg. Med.* 9: 193 (1989); D. Stern, R. Schoenlein, C.A. Puliafito, E.T. Dobi, R. Birngruber, and J.G. Fujimoto, "Corneal Ablations by Nanosecond, Picosecond, and Femtosecond Lasers at 532 and 625 nm," *Arch. Ophthalmol.* 107: 587 (1989).

⁶³ D. Stern, R. Schoenlein, C.A. Puliafito, E.T. Dobi, R. Birngruber, and J.G. Fujimoto, "Corneal Ablations by Nanosecond, Picosecond, and Femtosecond Lasers at 532 and 625 nm," *Arch. Ophthalmol.* 107: 587 (1989).

Chapter 1. Statistical Mechanics of Surface Systems and Quantum-Correlated Systems

Academic and Research Staff

Professor A. Nihat Berker

Graduate Students

Daniel P. Aalberts, Alexis Falicov, William C. Hoston, Jr., Roland R. Netz

1.1 Introduction

Sponsor

Joint Services Electronics Program
Contract DAAL03-89-C-0001
Contract DAAL03-92-C-0001

Our objectives are to develop, using renormalization-group theory and other methods of statistical mechanics, microscopic theories of quantum spin and electronic systems. Our approach is particularly suited to systems with fluctuations due to finite temperatures, impurities, surfaces or other geometric constraints.

1.2 Renormalization-Group Approach to Electronic Systems

Project Staff

Alexis Falicov, Professor A. Nihat Berker

High- T_c superconductivity, metallic magnetism, the metal-insulator transition, and heavy fermion behavior are all phenomena produced by the strong correlations of electrons in narrow energy bands. It is therefore important to study theoretical models that incorporate the strong correlation effects of electrons. The tJ model is such a system. It is defined on a lattice with one spherically symmetric orbital per site by the Hamiltonian

$$H_{tJ} = P \left[-t \sum_{\langle ij \rangle, \sigma} (c_{i\sigma}^\dagger c_{j\sigma} + \text{h.c.}) + J \sum_{\langle ij \rangle} (\vec{s}_i \cdot \vec{s}_j - n_i n_j / 4) \right] P,$$

where P is an operator that projects out all doubly occupied sites, $c_{i\sigma}^\dagger$ and $c_{i\sigma}$ are creation and annihilation operators for an electron in a Wannier state at site i with z -component of spin σ , n_i is the electron number operator that counts the total number of electrons at site i , and \vec{s}_i is the spin operator.

This Hamiltonian can be interpreted in two ways: (1) In the case of small J , the system can be thought of as the large U limit of the single-band Hubbard model of electronic systems. The antiferromagnetic exchange comes as a result of a virtual process where one electron hops onto a singly occupied nearest-neighbor site and then hops back. The energy gain for such a process is of the order of t^2/U since a doubly occupied site has energy U . (2) The system can also be thought of as an electronic system with a "super" exclusion principle where no two electrons (like or unlike spins) are allowed on the same site. The second interpretation does not put any restriction on the size of J .

There are few rigorous results available on this system: (1) At half filling, the system reduces to a Heisenberg antiferromagnet. (2) At $2t = \pm J$, the model has been solved by the Bethe-ansatz technique. (3) In one dimension and $J = 0$, the model has been solved also by the Bethe-ansatz technique. Other attempts to study this model have focused on the ground state and first few excited states. We have decided, instead, to focus on the thermodynamic properties of this system. Our method, the renormalization-group approach, involves solving a statistical mechanics problem by a recursive elimination of the degrees of freedom. Since the Hamiltonian involves a regular lattice, this problem is well suited for the position-space renormalization-group method. The solution is obtained in an expanded space with Hamiltonian

$$H = P \left[-t \sum_{\langle ij \rangle, \sigma} (c_{i\sigma}^\dagger c_{j\sigma} + \text{h.c.}) + \sum_{\langle ij \rangle} (J \vec{s}_i \cdot \vec{s}_j + V n_i n_j) + \mu \sum_i n_i \right] P.$$

Because of the non-commutativity of quantum operators, new techniques of renormalization-group theory had to be developed.

We have obtained the renormalization-group flows for the effective coupling constants for one-, two-, and three-dimensional systems. The flows determine the phase diagrams and all thermodynamic

properties. In one dimension, we find, as expected, no finite-temperature phase transition. In two dimensions, we find a single finite-temperature critical point, as previous workers conjectured but were unable to derive. In three dimensions, our preliminary results indicate a rich finite-temperature phase diagram with novel phases, phases transition behaviors, and conductivity phenomena. Our results are also confirmed by our exact small-cluster calculations.

1.3 Phase Diagrams of Semiconductor Alloys

Project Staff

William C. Hoston, Jr., Roland R. Netz, Professor A. Nihat Berker

A study of ternary compounds on face-centered-cubic lattices has been started. The aim of the work is to elucidate the phase behavior of ternary and quaternary semiconductor alloys. These alloys have received recent attention for both fundamental and technological reasons. It has been found that these alloys can exist in the zincblende, chalcopyrite, or possibly stannite structures, involving two interpenetrating fcc lattices on which up to four atomic species exist. One atomic species occupies one of the fcc lattices while three other atomic species may (chalcopyrite, stannite) or may not (zincblende) order on the other fcc lattice. At present, not much is known about the chalcopyrite structure seen in the experimentally obtained III-V compounds. There is great interest in learning how stable this chalcopyrite phase is against other possible structures.

In recent work by K.E. Newman and collaborators, the Blume-Emery-Griffiths model has been adopted for the study of the zincblende to chalcopyrite or stannite transitions. This model is a spin-1 Ising model with Hamiltonian

$$H = J \sum_{\langle ij \rangle} s_i s_j + K \sum_{\langle ij \rangle} s_i^2 s_j^2 - \Delta \sum_i s_i^2, \quad s_i = 0, \pm 1.$$

The three spin values are each associated with a different species of atom, A, B, or C, which exist on one of the fcc lattices. The other fcc lattice is considered occupied by atomic species D. The systems under consideration have the composition $[(AB)_{1-x}C_x]D_2$.

The model includes interactions between the A, B, and C atoms. The parameters J and K in the Hamiltonian above are fixed as combinations of these interaction energies. They are chosen so as to give the chalcopyrite structure at low temperature ($J < 0$) and to control the phase transition

between the chalcopyrite and the zincblende. Δ controls the relative densities of the species (AB) and C.

As a preliminary study, we have completed the global phase diagram study of the Blume-Emery-Griffiths model. We found six new phase diagrams, including novel multicritical topology and two new ordered phases. Thus, we determined that the phase diagram of this simple spin system includes nine distinct topologies and three ordered phases. These results were obtained by a global mean-field theory with four independent order parameters.

It is important to note, however, that the choice of $J < 0$ makes the model on the fcc lattice frustrated, which requires analysis beyond mean-field theory. We have developed a new method, which we have called "hard-spin mean-field theory," that incorporates the hard-spin condition of local degrees of freedom and thereby conserves frustration. We have tested this method on frustrated triangular and stacked triangular lattices with the spin-1/2 Ising model, obtaining excellent results. We are now applying the method to the Blume-Emery-Griffiths model. Our future studies of semiconductor alloys will also include renormalization-group theory.

1.4 Quantum Spin Systems

Project Staff

Daniel P. Aalberts, Professor A. Nihat Berker

We are interested in calculating the thermodynamic properties of quantum mechanical systems at low temperatures, where the distinctive quantum phenomena are important. The first model we consider is the $s = 1/2$ XXZ model, with Hamiltonian

$$H = \sum_{\langle ij \rangle} [J (s_i^x s_j^x + s_i^y s_j^y) + J_z s_i^z s_j^z].$$

This model in two dimensions is of interest in high- T_c superconductors; it is also of general interest to develop our ability to do the statistical mechanics of quantum systems and to extract, thereby, the quantitative properties of their elementary excitations.

We map this d-dimensional quantum system quantitatively onto a (d+1)-dimensional classical system with complicated interactions. For the ferromagnetic quantum system, we have been able to obtain magnon dispersion relations and magnon-magnon interactions. Eventually, we expect to apply our method to antiferromagnetic

quantum systems, where even the ground state presents a many-body problem.

1.5 Publications

Alerhand, O.L., A.N. Berker, J.D. Joannopoulos, D. Vanderbilt, R.J. Hamers, and J.E. Demuth. "Finite-Temperature Phase Diagram of Vicinal Si(100) Surfaces: Alerhand et al. Reply." *Phys. Rev. Lett.* 66(7): 962 (1991).

Berker, A.N. "Absence of Temperature-Driven First-Order Phase Transitions in Systems with Random Bonds." *J. Appl. Phys.* 70(10): 5941-5945 (1991).

Berker, A.N., and K. Hui. "Absence of Temperature-Driven First-Order Phase Transitions in Systems with Random Bonds." In *Science and Technology of Nanostructured Magnetic Materials*. Eds. G.C. Hadjipanayis and G.A. Prinz. New York: Plenum, 1991.

Berker, A.N., R.G. Caflisch, and M. Kardar. "Statistical Mechanics of Phase Transitions with a Hierarchy of Structures." In *Hierarchically Structured Materials*. Ed. I.A. Aksay. Pittsburgh: Materials Research Society, 1992.

Hoston, W., and A.N. Berker. "Multicritical Phase Diagrams of the Blume-Emery-Griffiths Model with Repulsive Biquadratic Coupling." *Phys. Rev. Lett.* 67(8): 1027-1030 (1991).

Hoston, W., and A.N. Berker. "Dimensionality Effects on the Multicritical Phase Diagrams of the Blume-Emery-Griffiths Model with Repulsive Biquadratic Coupling: Mean-Field and Renormalization-Group Studies." *J. Appl. Phys.* 70(10): 6101-6103 (1991).

Hoston, W. *Multicritical Phase Diagrams of the Blume-Emery-Griffiths Model with Repulsive Biquadratic Coupling: Mean-Field and Renormalization-Group Studies*. S.M. thesis, Dept. of Physics, MIT, 1991.

Netz, R.R. "New Phases and Multiple Reentrance of the Blume-Emery-Griffiths Model with Repulsive Biquadratic Coupling: Monte Carlo Renormalization-Group Theory." *Europhys. Lett.* 17(4): 373-377 (1992).

Netz, R.R., and A.N. Berker. "Monte Carlo Mean-Field Theory and Frustrated Systems in Two and Three Dimensions." *Phys. Rev. Lett.* 66(3): 377-380 (1991).

Netz, R.R., and A.N. Berker. "Hard-Spin Mean-Field Theory: Formulation for Ising, XY, and Other Models." *J. Appl. Phys.* 70(10): 6074-6076 (1991).

Netz, R.R., and A.N. Berker. "Monte Carlo Mean-Field Theory and Frustrated Systems in Two and Three Dimensions: Netz and Berker Reply." *Phys. Rev. Lett.* 67(13): 1808 (1991).

Netz, R.R., and A.N. Berker. "Smectic C Order, In-Plane Domains, and Nematic Reentrance in a Microscopic Model of Liquid Crystals." *Phys. Rev. Lett.* 68(3): 333-336 (1992).

Netz, R.R., and A.N. Berker. "Microscopic Liquid Crystal Theory of Nematic Reentrance, Smectic C Ordering, and In-Plane Domain Formation." In *Phase Transitions in Liquid Crystals*. Ed. S. Martellucci. New York: Plenum, 1992.

Netz, R.R. "Microscopic Theory of the Ripple Phase." In *Structure and Conformation of Amphiphilic Membranes*. Ed. R. Lipowsky. Berlin: Springer-Verlag, 1992.

Netz, R.R. *Frustration in Magnetic, Liquid Crystal, and Surface Systems: Monte Carlo Mean-Field Theory*. S.M. thesis, Dept. of Physics, MIT, 1991.

Meeting Papers

American Physical Society Meeting, Cincinnati, Ohio, March 18-22, 1991.

Berker, A.N. "Quenched Fluctuation Induced Second-Order Phase Transitions."

Hoston, W., and A.N. Berker. "New Multicritical Phase Diagrams from the Blume-Emery-Griffiths Model with Repulsive Biquadratic Interactions."

Netz, R.R., and A.N. Berker. "Monte Carlo Mean-Field Theory and Frustrated Systems in Two and Three Dimensions."

American Physical Society Meeting, Indianapolis, Indiana, March 16-20, 1992.

Aalberts, D.P., and A.N. Berker. "Hard-Spin Mean-Field Theory: Variational Free Energy and First-Order Phase Transitions."

Berker, A.N., and R.R. Netz. "Smectic C Order, In-Plane Domains, and Nematic Reentrance in a Frustrated Microscopic Model of Liquid Crystals."

Netz, R.R. "Symmetry-Breaking Fields in Frustrated Ising Systems on Square and Cubic Lattices."

Netz, R.R. "Multiple Reentrance and New Phases from the Blume-Emery-Griffiths Model in Three Dimensions: Monte Carlo Renormalization-Group Theory."

International Conference on Thermodynamics and Statistical Mechanics, Berlin, Germany, August 2-8, 1992.

Berker, A.N. "Critical Behavior Induced by Quenched Disorder."

Netz, R.R., and A.N. Berker. "Smectic C/A₂ Order, Domains, Reentrance in a Microscopic Model of Liquid Crystals."

International Liquid Crystal Conference, 14th, Pisa, Italy, June 21-26, 1992.

Netz, R.R. and A.N. Berker. "Smectic C Order, Nematic Reentrance, Domains, and Smectic A₁-Smectic A₂ Transitions in a Frustrated Microscopic Model of Liquid Crystals."

Magnetism and Magnetic Materials-Intermag Conference, Pittsburgh, Pennsylvania, June 18-21, 1991.

Berker, A.N. "Absence of Temperature-Driven First-Order Phase Transitions in Systems with Random Bonds."

Hoston, W., and A.N. Berker. "New Multicritical Phase Diagrams from the Blume-Emery-Griffiths Model with Repulsive Biquadratic Interactions."

Netz, R.R., and A.N. Berker. "Monte Carlo Mean-Field Theory and Frustrated Systems in Two and Three Dimensions."

NATO Advanced Study Institute on Liquid Crystals, Erice, Italy, May 2-12, 1991.

Berker, A.N. "Microscopic Theory of Polar Liquid Crystals and Multiply Reentrant Phase Diagrams."

Netz, R.R., and A.N. Berker. "The Mean-Field Theory for Frustration, Layered Magnets, and Reentrant Liquid Crystals."

Statistical Mechanics Meeting, 65th, New Brunswick, New Jersey, May 15-17, 1991.

Hoston, W., and A.N. Berker. "Bicritical and Tetracritical Phase Diagrams of the BEG Model: Dimensionality Effects."

Netz, R.R., and A.N. Berker. "Microscopic Theory of Smectic A and C Phases of Frustrated Liquid Crystals."

Chapter 2. Synchrotron X-Ray Studies of Surface Disordering

Academic and Research Staff

Professor Robert J. Birgeneau, Dr. Kenneth I. Blum, Dr. Do-Young Noh

Graduate Students

William J. Nuttall, Monte J. Ramstad

Technical and Support Staff

Elizabeth M. Salvucci

2.1 Introduction

Sponsor

Joint Services Electronics Program
Contract DAAL03-89-C-0001
Contract DAAL03-92-C-0001

In this research program we use modern x-ray scattering techniques to study structures and phase transitions in thin films and on surfaces. We have two principal experimental facilities, one at MIT and the other at the National Synchrotron Light Source at Brookhaven National Laboratory. At MIT, we have four high-resolution computer-controlled x-ray spectrometers using high-intensity, rotating anode x-ray generators. The angular resolution can be made as fine as 1.8 seconds of arc, which enables us to probe the development of order from distances of the order of the x-ray wavelength $\sim 1\text{\AA}$ up to $30,000\text{\AA}$. The sample temperature can be varied between 2 K and 500 K with a relative accuracy of 2×10^{-3} K. At the National Synchrotron Light Source, in collaboration with IBM, we have three fully instrumented beam lines. Two of these beam lines allow us to make studies with photons varying in energy between 3 and 12 keV; the third has a fixed energy of 17 keV. These facilities make possible high-resolution scattering experiments with a flux of more than three orders of magnitude larger than that of a rotating anode x-ray generator, opening up a new generation of experiments.

Several years ago, as part of this JSEP program, we built an x-ray-compatible, high vacuum single crystal apparatus. This enabled us to use synchrotron radiation to study the structures and transitions occurring at a single surface, and such experiments are now becoming routine. As a result of our recent research, we determined that a new chamber allowing access to a wider range of reciprocal space was required. In collaboration with Professor Simon G.J. Mochrie, we have

designed, built and are now commissioning this second-generation x-ray surface facility.

Our basic scientific objective is to understand the morphologies and microscopic structures of simple semiconductor and metal surfaces at high temperatures. Possible phase changes include surface roughening, surface reconstruction, melting, amorphization and dilution. These phenomena are particularly interesting on stepped surfaces, where there may be an interplay between step structures, faceting, reconstruction, and roughening.

2.2 Metal Surface Studies

In 1987 we reported a detailed study of a possible roughening transition of the Ag(110) surface. Specifically, we discussed the detailed line shape of the Ag(110) surface peak for temperatures between 100°C and 525°C . At $\sim 450^\circ\text{C}$ we observed a crossover to a pure power law lineshape, indicative of a rough surface, for the near-surface diffraction. Above 450°C the profiles could be described by the power law singularity form $(Q - Q_{110})^{-2+\eta}$ with η changing rapidly with temperature. Accordingly, we identified 450°C as the roughening temperature.

Our more recent experiments and those by others on crystals with very small miscuts ($\sim 0.5^\circ$) suggest that the story may be more complicated. Specifically, the experiments suggest that below $\sim 450^\circ\text{C}$ to 500°C , the Ag(110) surface may be faceted. In order to explore this further, we have begun a systematic set of experiments on vicinal Ag(110) crystals with miscuts in the (110) direction of up to 4° . Our initial experiments on a crystal miscut by $\sim 2.3^\circ$ indeed show faceted behavior below $\sim 500^\circ\text{C}$. Further experiments should elucidate the full nature of the roughening-faceting transition on this prototypical noble metal surface.

2.3 Semiconductor Surface Studies

2.3.1 Stepped Si(111) Surfaces

The behavior of vicinal surfaces (surfaces cut a few degrees away from low index facets) involves essential aspects of surface structures including equilibrium crystal shapes, roughening, faceting, and surface reconstruction. The stability of vicinal surfaces is determined by the shape of the equilibrium crystal surface. By studying a series of vicinal surfaces with various surface normals, one can map out the equilibrium crystal shape. A vicinal surface, when it is stable, forms a structure consistent with low-index terraces separated by steps whose spacing is usually incommensurate with the bulk substrate lattice. As in the case of incommensurate domain wall problems, there can not be true long range order in the structure of the incommensurate steps. This is due to the overwhelming amplitude of the long wavelength thermal fluctuations in two-dimensional systems with continuous symmetry. As a result, an incommensurate stepped surface is rough in an exact sense. A vicinal surface becomes unstable when the free energy of a nearby low index facet is lowered drastically by some mechanisms such as reconstruction. One might expect that the lowering of free energy of a low-index facet would break a vicinal surface into a low-index facet and rough faces with a higher misorientation angle.

We have carried out a detailed synchrotron x-ray scattering study of a vicinal Si(111) surface misoriented by 3.5° toward the (112) direction. At temperatures higher than the "7 x 7-to-1 x 1" transition, we find that the surface is composed of steps with a mean separation of $\sim 60\text{\AA}$ which are correlated beyond 3000\AA . Below the transition, the surface is split into the large ($> 3000\text{\AA}$) perfectly flat (111) facets together with stepped regions whose misorientation angle increases as temperature is decreased. The transition is first order, indicating that it is induced by the 7 x 7 reconstruction of the (111) facets. In the faceted phase, the facet angle α follows the law $\tan \alpha \sim |T_c - T|^{(\lambda-1)/\lambda}$ with $\lambda = 2.3 \pm 0.3$. This disagrees somewhat with the theoretical predication $\lambda = 3/2$ for models in which the interaction between steps is entropic in character.

At temperatures above 1110 K, we observed two step superlattice peaks bracketing the (10) position of the (111) surface. Figure 1 shows high resolution longitudinal and transverse scans through the first-order step peak at 1120 K. The simplest model leads us to believe that this peak results from the ordering of steps by the entropic

repulsion. To test this idea quantitatively, we fit the high temperature peak profile to a 2D power law singularity of the form

$$S(\vec{q}) = (q_H^2 + Bq_K^2)^{(-2+\eta_1)/2}$$

convolved with the instrumental resolution function. Figure 1 shows the optimal simultaneous fits to the longitudinal and transverse scans with $h = 0.6 \pm 0.1$ and $B = 15 \pm 7$. It is evident that the power law form fits the data very well. The large value of η_1 is fully consistent with scattering from a rough surface whose height variance diverges logarithmically with distance. We note that as in the stripe domain commensurate-incommensurate problem the Pokrovsky-Talapov model leads to the prediction $\eta_1 = 2/9$, independent of temperature. This is in clear disagreement with our results. More elaborate models of the interaction between the steps are needed to explain the large value of η_1 .

More recently, we have been studying the behavior of vicinal Si(111) at very high temperatures. Remarkably, we find that at ~ 1300 K there is a second phase transition in the step structure which mimics a surface melting transition. We are currently exploring this new-found phenomenon.

2.4 Publications

Blum, K.I., D.Y. Noh, A. Mak, K.W. Evans-Lutterodt, J.D. Broch, G.A. Held, and R.J. Birgeneau. "Structure and Phase Transitions of Ge(111) and Si(111) Surfaces at High Temperatures." In *Surface X-Ray and Neutron Scattering*. Vol. 61, pp. 27-31. Springer Proceedings in Physics. Ed. H. Zabel and I.K. Robinson. Berlin/Heidelberg: Springer-Verlag, 1992.

Keane, D.T., P.A. Bancel, G.L. Jordan-Sweet, G.A. Held, A. Mak, and R.J. Birgeneau. "Evidence for Two-Step Disordering of the Au(110) 1 x 2 Reconstructed Surface." *Surf. Sci.* 250: 8 (1991).

Mak, A., K. Evans-Lutterodt, K.I. Blum, D.Y. Noh, J.D. Brock, G.A. Held, and R.J. Birgeneau. "Synchrotron X-ray Diffraction Study of the Disordering of the Ge(111) Surface at High Temperatures." *Phys. Rev. Lett.* 66: 2002 (1991).

Noh, D.Y., K. Blum, M.J. Ramstad, and R.J. Birgeneau. "Long Range Separation of Steps on Vicinal Si(111)." *Phys. Rev. B* 44: 10969 (1991).

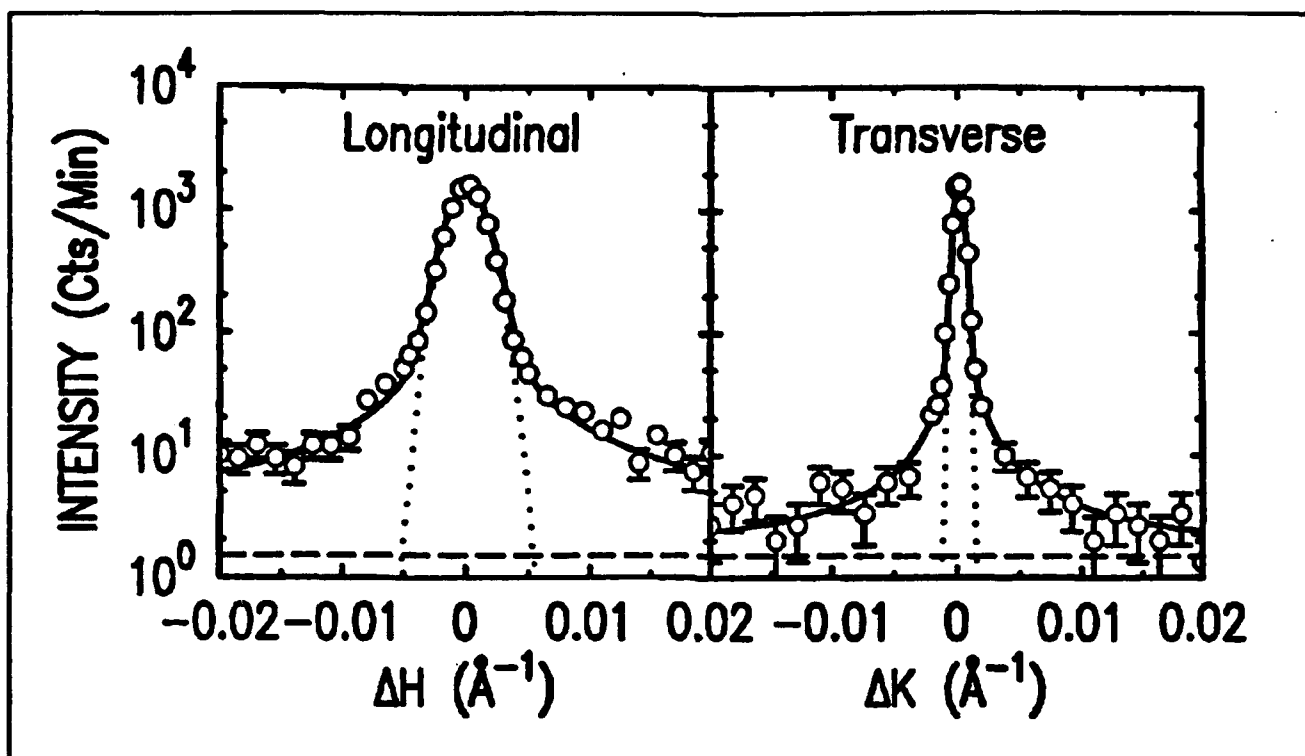


Figure 1. Longitudinal and transverse scans through the first order Si(111) step surface peak. The dotted curves are the resolution. The solid curves are the result of fits to the power-law lineshape with $\eta = 0.6$ and $B = 15$.



Professor Sylvia T. Ceyer

Chapter 3. Chemical Reaction Dynamics at Surfaces

Academic and Research Staff

Professor Sylvia T. Ceyer, Dr. Yulin Li, Dr. David P. Pullman, Dr. Arthur L. Utz

Graduate Students

Sean P. Daley, Theodore R. Trautman, Julius J. Yang

Undergraduate Students

Gerald R. Cain

Technical and Support Staff

Anne Stollerman

3.1 Dynamics of the Reaction of F₂ with Si(100)

Sponsor

Joint Services Electronics Program
Contract DAAL03-89-C-0001
Contract DAAL03-92-C-0001

Project Staff

Professor Sylvia T. Ceyer, Dr. Yulin Li, Dr. David P. Pullman, Julius J. Yang, Gerald R. Cain

As we have shown previously, F₂ reacts with Si(100) with very close to unity probability (~ 0.95) up to one monolayer of coverage, contrary to popular belief. We have now also shown that the sites for fluorine adsorption under these conditions are the dangling bonds and that the adsorbed fluorine does not lift the reconstruction. This was accomplished using a new technique of He atom diffraction that we have recently implemented in our molecular beam-ultrahigh vacuum surface scattering apparatus. The experiment is carried out by directing a well-characterized, monoenergetic beam of He atoms at the surface and monitoring the angular distribution of the diffracted atoms. This arrangement adds a powerful new structural probe to our experimental capabilities. While the binding of fluorine to the dangling bonds along with the maintenance of the surface dimer bond is not surprising, our results show the first experimental evidence for it. No experimental information about this system had been available previously because the common structural probes, electron diffraction techniques, are not sensitive to halogens.

Publications

Ceyer, S.T., D.J. Gladstone, M. McGonigal, and M.T. Schulberg. "Molecular Beams: Probes of the Dynamics of Reactions on Surfaces." In *Physical Methods of Chemistry*. 2nd ed. Eds. B.W. Rossiter, J.F. Hamilton, and R.C. Baetzold. New York: Wiley, 1991. Forthcoming.

3.2 Dynamics of the Reaction of F₂ with Fluorinated Si(100)

Sponsor

Joint Services Electronics Program
Contract DAAL03-89-C-0001
Contract DAAL03-92-C-0001

Project Staff

Professor Sylvia T. Ceyer, Dr. Yulin Li, Dr. David P. Pullman, Julius J. Yang, Gerald R. Cain

We have previously shown that the reaction probability of F₂ with a clean Si(100) surface decays from near unity to zero as the fluorine coverage increases to one monolayer. This lack of reactivity with the fluorinated Si surface is the source of the misconception that F₂ does not react with Si. The lack of reactivity with the fluorinated surface precludes the build up of a sufficient layer of fluorine to produce the volatile etch product, SiF₄. However, we have also previously shown that if the kinetic energy of the incident F₂ molecule is increased above a threshold value of 6 kcal/mol (~ 0.25 eV), the dissociation probability of F₂ with a fluorinated Si surface increases linearly with the normal component of kinetic energy. This is a result of a barrier to dissociation that is overcome by translational energy of the incident molecule.

The enhancement in the dissociation probability allows enough fluorine to be deposited to form the etch product, SiF_4 . This result establishes that Si can be etched with low energies using molecular beam techniques and without the use of plasmas. The low energies afforded by molecular beam techniques prevent the introduction of radiation damage or defects into the Si lattice, which are typical results of plasma etching.

We have begun a new project aimed at determining the origin of the barrier to dissociation of F_2 on the fluorinated surface. The hypothesis is that the barrier to F_2 dissociation is largely associated with breaking the Si surface dimer bond. To test this hypothesis, we are using He atom diffraction as a probe of the surface structure after exposure to the energetic F_2 . Preliminary measurements indicate that the disappearance of the dimer bond, as measured by the half order diffraction feature, correlates well with the increase in the dissociation probability as a function of the F_2 incident translational energy in the normal direction. This result may be the first determination of the physical origin of a reaction barrier in any semiconductor system.

3.3 New Mechanisms for Surface Processes

Sponsor

National Science Foundation
Grant CHE 90-20623

Project Staff

Professor Sylvia T. Ceyer, Dr. Arthur L. Utz, Andrew D. Johnson, Sean P. Daley, Theodore R. Trautman

We report the first detection and identification of vibrational modes of buried species by high resolution electron energy loss spectroscopy (HREELS) and the observation of a new mechanism for absorption of adsorbates, collision-induced absorption, as applied to the interaction of hydrogen with Ni(111).

Subsurface or bulk sites of a Ni single crystal are populated with atomic hydrogen by exposure of the (111) face of the Ni crystal at 130 K to atomic hydrogen. Atomic hydrogen is generated by thermal dissociation of H_2 over a hot tungsten filament positioned 0.25 inches from the crystal surface. This results in a flux of both atomic and molecular hydrogen to the front surface of the crystal. The H^+ ions and electrons generated by the

filament are shown to play no role in the following observations. Both atomic H and H_2 result in population of the threefold hollow surface sites up to a surface saturation coverage of 1 ML. The HREEL spectrum at 1 ML is characterized by the Ni-H asymmetric stretch at 955 cm^{-1} and the Ni-H symmetric stretch at 1170 cm^{-1} , and the thermal desorption spectrum exhibits two maxima at 340 and 380 K. Further exposure to atomic H results in the appearance of a new feature in the HREEL spectrum at 800 cm^{-1} and in the thermal desorption spectrum at 180-220 K. The loss feature at 800 cm^{-1} , for which an impact scattering mechanism is operable, is identified as a Ni-H vibration of bulk H by the similarity of the dependence of its intensity on electron impact energy to the dependence of the electron inelastic mean free path on electron energy. At 3 eV impact energy, the intensity of the 800 cm^{-1} loss feature is large but decreases monotonically to almost zero as the impact energy is increased beyond 15 eV. This kind of dependence of the intensity of a loss feature associated with a bulk vibrational mode is expected because the inelastic mean free path of an electron, which is 80 Å at 3 eV, rapidly drops to 1 Å as the energy is increased above the plasmon frequency of the metal (15 eV), where plasmon creation is the predominant energy loss mechanism which shortens the mean free path. In contrast, the intensity of the two loss features associated with surface chemisorbed H exhibits almost no dependence on electron energy with the exception of a resonance at 7 eV. As much as an equivalent of 8 monolayers of hydrogen have been absorbed into the bulk.

Subsurface or bulk sites of Ni can also be populated via a newly observed mechanism, collision-induced absorption. A beam of monoenergetic Kr or Xe atoms, produced by the supersonic expansion of Kr or Xe seeded in He, is directed at a monolayer of atomic hydrogen chemisorbed on Ni(111). The impacts of the incident inert gas atoms are observed to induce the absorption of the chemisorbed hydrogen. The hydrogen thus absorbed is identified by the appearance of (1) a loss feature at 800 cm^{-1} and (2) a feature at 180-220 K in the thermal desorption spectrum, consistent with the study of atomic hydrogen absorption. The absorption probability scales linearly with the energy of the incident Xe atom above a threshold energy of 2.5 eV. Collision-induced absorption may play a significant role in the mechanism for hydrogen absorption in the high pressure environments of a hydrogen storage cell where the hydrogen saturated surface is continually subject to bombardment by a large flux of energetic particles.

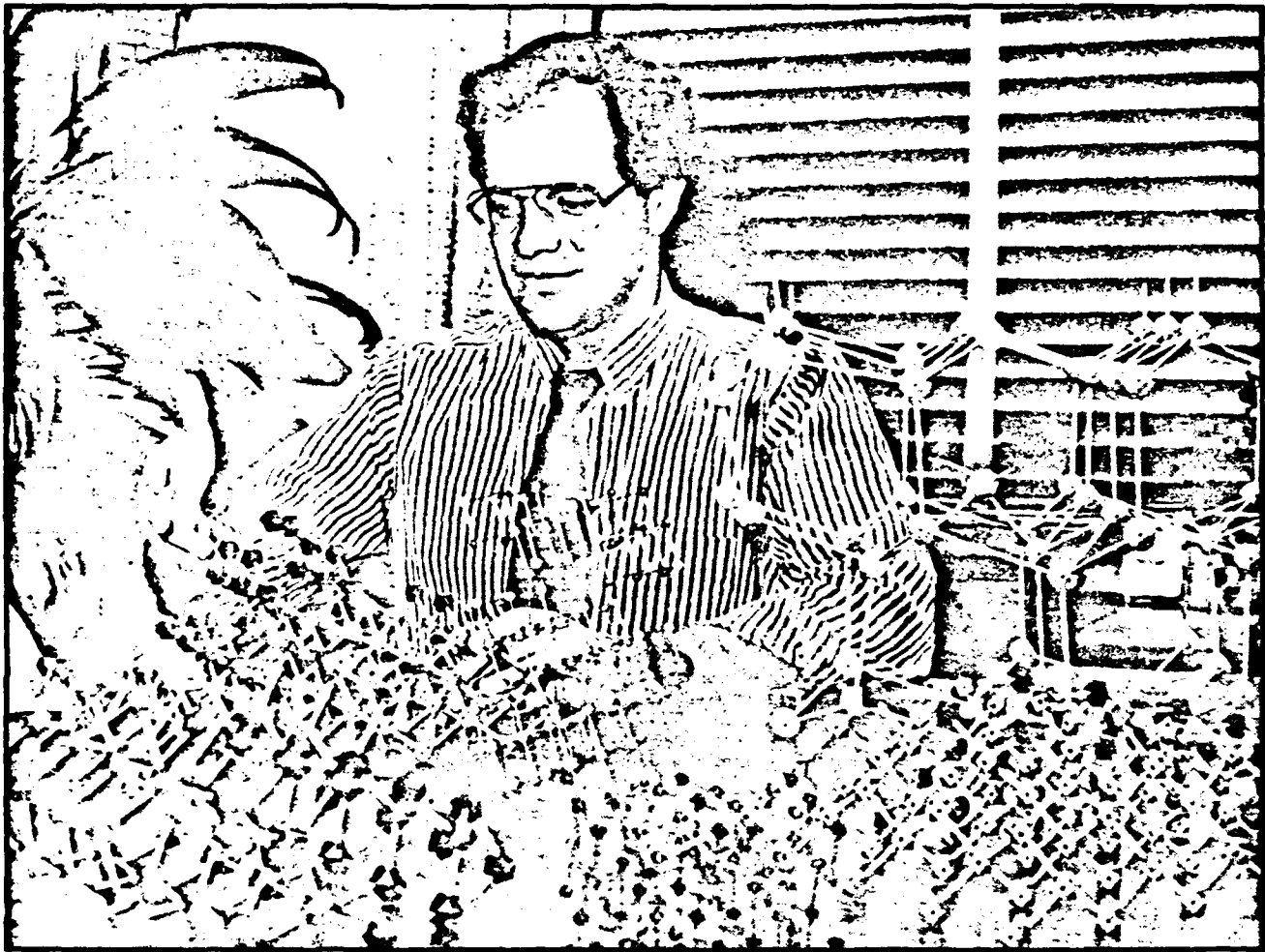
Publications

Johnson, A.D. *Dynamics of Hydrogen Absorption into the Ni(111) Bulk: Spectroscopic Identification and Chemistry of Subsurface Hydrogen*. Ph.D. diss., Dept. of Chem., MIT, 1991.

Johnson, A.D., K.J. Maynard, S.P. Daley, Q.Y. Yang and S.T. Ceyer. "Hydrogen Embedded in

Ni: Production by Incident Atomic Hydrogen and Detection by High Resolution Electron Energy Loss." *Phys. Rev. Lett.* 67: 927 (1991).

Maynard, K.J., A.D. Johnson, S.P. Daley and S.T. Ceyer. "A New Mechanism for Absorption: Collision Induced Absorption." *J. Chem. Soc., Faraday Discussion* (1991). Forthcoming.



Professor John D. Joannopoulos

Chapter 4. Semiconductor Surface Studies

Academic and Research Staff

Professor John D. Joannopoulos, Dr. Arnaldo Dal Pino, Dr. Robert D. Meade

Graduate Students

Tomas A. Arias, Kyeongjae Cho, Andrew M. Rappe, Jing Wang

4.1 Introduction

Sponsor

Joint Services Electronics Program

Contract DAAL03-89-C-0001

Contract DAAL03-92-C-0001

Understanding the properties of surfaces of solids and the interactions of atoms and molecules with surfaces has been of extreme importance both from technological and academic points of view. The recent advent of ultrahigh vacuum technology has made microscopic studies of well-characterized surface systems possible. The way atoms move to reduce the energy of the surface, the number of layers of atoms involved in this reduction, the electronic and vibrational states that result from this movement, and the final symmetry of the surface layer are all of utmost importance in arriving at a fundamental and microscopic understanding of the nature of clean surfaces, chemisorption processes, and the initial stages of interface formation.

The theoretical problems associated with these systems are quite complex. However, we are currently at the forefront of solving for the properties of real surface systems. In particular, we are continuing toward our goal of calculating the total ground-state energy of a surface system from "first principles," so that we can provide accurate theoretical predictions of surface geometries. Our efforts in this program have concentrated in the areas of surface growth, surface reconstruction geometries, structural phase transitions, and chemisorption.

4.2 Heteroepitaxial Growth

Epitaxial growth of dissimilar semiconductor materials holds significant potential for technological applications and has been the subject of major international efforts in recent years. Nevertheless, relatively little theoretical work has been performed to understand the fundamental interactions governing the initial stages of growth and the struc-

ture of the first few monolayers in these systems. Of particular interest is the prototypical system involving growth of GaAs on Si(100) substrates. Since growth typically begins with an As overlayer, one first needs to understand this seemingly simple system. Experimentally, it is observed that the adsorption of As on a stepped Si(100) surface can drastically rearrange the distribution of steps of the original surface. These changes in surface morphology are controlled by different factors, including temperature, coverage of As, and the type and density of steps on the original surface. The structure of the the As-covered Si(100) surface [henceforth Si(100):As] determines many of the properties of the final epitaxial film.

In particular, it has been observed that GaAs grown epitaxially on Si(100) can have two orientations, related by a 90 degree rotation, with respect to the Si(100). This puzzling observation, the so-called sublattice-orientation (or allocation) dilemma, has not been understood. Naively, this could be explained if the first epilayer above the Si substrate could be selected to be a Ga or As layer. However, bond strength and other theoretical arguments, as well as experimental evidence, show this selective wetting of the Si(100) surface by As or Ga does not occur.

In this work we have performed theoretical calculations which show that As adsorbed on a vicinal Si(100) surface with double-layer steps either *can grow directly on top of the Si surface, or can rearrange the surface so that it replaces the original top Si layer*. The former structure is metastable and results from growth at low temperatures. The latter has lower energy and occurs for growth at substrate temperatures where surface diffusion is activated. Replacing adsorption by substitution changes the sublattice of the diamond structure exposed at the surface and corresponds to a 90 degree rotation of the crystal orientation about the surface normal. The resulting two configurations of the stepped Si(100):As surface are related by a 90 degree rotation, but otherwise differ only in the type of steps present at the surface. Their difference in energy, which we calculate from first principles, is related to the relaxation of stress at surface steps. This result shows that the rear-

rangement of steps upon As adsorption controls the orientation of an epitaxial GaAs film.

Both Si(100) and Si(100):As surfaces have 2×1 reconstructions where surface atoms (Si in the first case and As in the second) form dimers arranged in parallel rows. A simple picture for the adsorption of As on Si(100) is that the Si dimers break and As dimers are formed on top, perpendicular to the original Si dimers. This rotates the orientation of the surface dimers by 90° . A single-domain Si(100) 2×1 surface would result in a single-domain Si(100):As 1×2 surface. STM images show that the orientation of the As dimers depends on the substrate temperature T_s during deposition. For low initial temperatures ($T_s \leq 400^\circ\text{C}$) the surface reconstruction rotates from 2×1 to 1×2 , as the simple picture describes.

We begin by considering a single-domain Si(100) 2×1 surface, as typically used in growth experiments. These are obtained by using double-layer-stepped vicinal surfaces misoriented towards the [011] direction. Here we will restrict ourselves to the case where both the starting Si(100) and the final Si(100):As surfaces are double-layer stepped and the As coverage is one complete monolayer. These are the conditions relevant to typical growth conditions. On the clean Si(100) surface the Si dimers are parallel to the step edges. Double-layer steps with dimers perpendicular to the edge have much higher energy and are not observed. In principle, there are two types of double-layer steps on the Si(100):As surface. Type A, where the As dimers are perpendicular to the step edge [Figure 1(a)], and type B, where the As dimers are parallel to the edges [Figure 1(b)]. The reconstruction of the surface is 1×2 with type-A steps, and 2×1 with type-B steps. Figure 1 shows steps with a simple edge termination, where Si atoms are fourfold coordinated and As atoms are threefold coordinated with a doubly occupied lone-pair orbital. This is the same bonding configuration that passivates the flat Si(100):As surface. Other step reconstruction we considered, which are discussed later in this chapter, were found to have higher energies.

To determine the relative stability of the 1×2 and 2×1 stepped Si(100):As surfaces, we compare the energies of surfaces with type-A and type-B steps, respectively. We calculate total energies from first principles within the framework of density-functional theory in the local-density approximation, using norm-conserving pseudo-potentials.

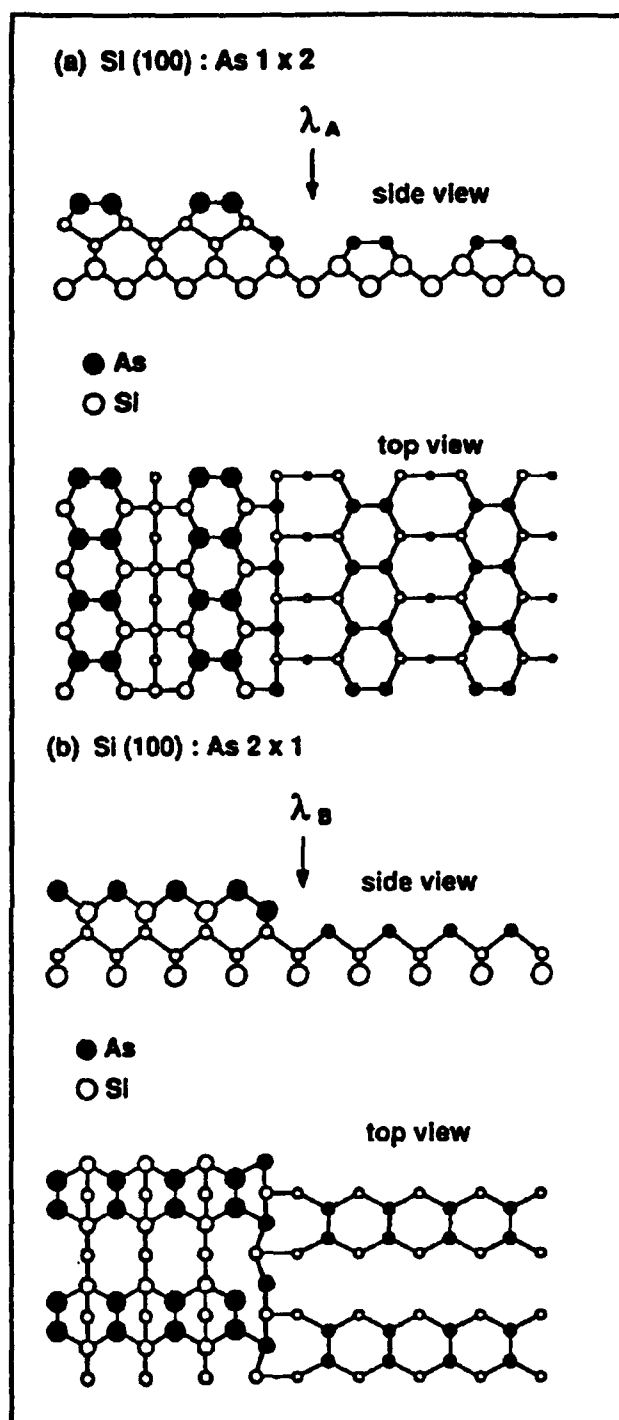


Figure 1. Top and side views of double-layer steps on Si(100):As surfaces. (a) Type-A steps: As dimers perpendicular to the step edge. (b) Type-B steps: As dimers parallel to the step edge (edge relaxation is illustrated in the top view, see text). Larger circles on top views represent atoms closer to the surface. The two circle sizes on side views represent front and back [011] planes.

The calculated energy difference between type-A and type-B steps of Si(100):As is

$$\lambda_A - \lambda_B = (200 \pm 20) \text{ meV/a}, \quad (1)$$

where λ_A and λ_B are the energies of type-A and type-B steps, respectively, and $a = 3.80\text{\AA}$ is the unit length along the step. This energy difference is large enough to change the surface from one step configuration to the other. Indeed, an energy difference of $\sim 110 \text{ meV/a}$ between single- and double-layer steps on vicinal Si(100) surfaces (for a surface misorientation larger than $\sim 3\text{--}4^\circ$) drives the surface to have a majority of double-layer steps. It should be noted that the calculated step energies represent step-formation plus step-step-interaction energies, and the large size of these systems makes it prohibitive to increase the separation between steps and systematically separate these two contributions. However, it is assumed that the latter is approximately eliminated from the problem by taking energy differences between stepped surfaces and that this difference does not change significantly with larger step separations.

An inspection of figure 1 shows no obvious electronic origin for the large energy difference between type-A and type-B steps. In both cases the Si and As atoms have ideal bonding configurations, and there is no particular atom or bond whose relaxation or rehybridization might explain this result. We find that the energy difference is related to the relaxation of surface stress. The Si(100):As surface is under a large tensile stress, both parallel and perpendicular to the As dimers, that results from the tendency of the As atoms to form 90 degree bond angles and pull themselves up from the surface. This stress introduces a torque on surface steps, which allows a lateral contraction of the surface in the region near the steps, at the expense of introducing bulk strain.

Figure 2 shows the response of type-A and type-B steps to the tensile surface stress. Type-A steps lead to a large lateral contraction. This contraction is $\sim 3.5\%$ for the first layer of Si atoms, most of it within two lattice constants from the step edge (see inset in figure 2), and decays to zero deeper into the bulk. The surface As dimers, perpendicular to the step edge, are $\sim 2\%$ shorter than their calculated value on a flat Si(100):As surface. The relaxation type-B steps is different, even though the strength the tensile stress is calculated to be approximately equal both parallel and perpendicular to the surface dimers [the large energy difference in equation (1) is consistent with this]. Figure 2 shows that type-B steps undergo almost no contraction. Still, the relaxed coordinates suggest that the surface stress has been significantly reduced. Although we have not directly calculated the stress remaining on the stepped

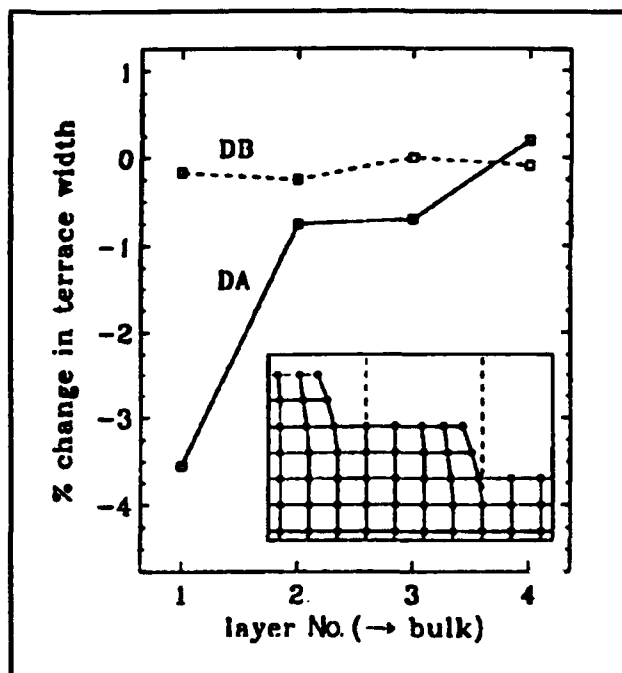


Figure 2. Layer-by-layer lateral contraction for a surface with type-A (solid line) and type-B (dashed line) steps as a function of penetrate into the bulk. Layer No. 1 denotes the first layer of Si atoms below the surface As dimers. Inset: Schematic representation of lateral contraction for a surface under tensile stress, defined with respect to the ideal terrace width shown by the vertical dashed lines.

surface (such calculations are beyond current capabilities), the lack of strain in the subsurface of type-B steps provides evidence of reduced surface stress. On flat Si(100):As subsurface strain forces a displacement of atoms from their ideal bulk positions. Atoms in third and fourth layers that are underneath surface dimers shift up, and subsurface atoms that are between dimer rows shift down. For type-A steps this distortion is further enhanced. On the other hand, for type-B steps the relaxed positions of the subsurface atoms are close to their ideal bulk value. This lack of strain in the subsurface for type-B steps is consistent with the reduction of surface stress.

We now address the implications of these results to growth experiments. Our calculations show that the Si(100):As 1×2 surface with type-A steps is a metastable structure. This surface results from the growth of As directly on top of the initial Si surface. Experimentally, it is obtained by depositing As at low substrate temperatures, where the As overlayer caps the surface and freezes any surface mobility. However, if the temperature is high enough during As deposition to activate surface diffusion, the surface can then reach the lower-energy configuration with type-B steps. This explains the surprising experimental observations. We note that this change in step type

requires a large rearrangement of the surface, but similar step redistributions requiring mass transport across the surface have been observed when the initial Si surface has single-layer steps. The transformation from type-A to type-B step may occur through other intermediate step configurations, including single-layer steps, and a complete conversion may not occur because of the large amount of mass transport required. This may further depend on the flux of As, and on whether As₂ or As₄ gas sources are used. Also, if surface diffusion is completely frozen or defects pin the edges of steps, type-A steps with a rebonded edge may occur on terraces that originally had an odd number of lattice sites, and both types of type-A steps may appear on the low-temperature surface. In principle, the surface with type-B steps ought to be reached from the surface with type-A steps upon annealing. However, As begins to leave the surface before this change occurs, and mixtures of steps with different heights are then observed.

It should be noted that since the driving force for the rotation of the As surface dimers is the difference in energy between type-A and type-B steps, as the surface misorientation becomes smaller and the density of steps decreases, the energy gain by step rearrangement diminishes. On nearly flat surfaces only the $2 \times 1 \rightarrow 1 \times 2$ change in orientation of Si to As surface dimers should be observed.

For the heteroepitaxial growth of GaAs on Si(100), our results predict the sequence of orientations of the Si and then As surface dimers in the growth process of Si(100) \rightarrow Si(100):As \rightarrow GaAs/Si(100). For low initial substrate temperatures, the predicted sequence is $2 \times 1 \rightarrow 1 \times 2 \rightarrow 4 \times 2$, and for high initial temperatures the sequence is $2 \times 1 \rightarrow 2 \times 1 \rightarrow 2 \times 4$. The final orientation of the GaAs epilayer depends on whether the equilibrium Si(100):As surface is attained, illustrating the interplay between kinetics and energetics in epitaxial crystal growth. This result explains the sublattice orientation dilemma and brings into a coherent picture experiments that seemed to be in contradiction. Also, type-A and type-B steps on Si(100):As may promote different nucleation channels for growth, leading to epitaxial films with different characteristics.

4.3 Molecules

In order to begin to address problems associated with molecules interacting with solid surfaces, it is important to test the applicability of the theoretical tools (developed for condensed matter systems) for isolated molecules. Moreover, if successful, these tools could be used to study large heterogeneous nonperiodic systems such as biological mol-

ecules that may consist of extended organic fragments, metal ions, and solvent water molecules. As a first step in this direction, *ab initio* theoretical calculations were performed on a large number of molecules with a variety of sizes and functional groups consisting of the first-row elements. These include the simple molecules H₂, H₂O, CH₄ and NH₃ that are constituents of the "biotic-soup" of the primordial atmosphere, neutral glycine which is the simplest amino acid, and formamide, which models the peptide-bond between amino acids in a protein.

Table I lists the results of our theoretical calculations (LDAP-PW) and compares them with both experimental values and quantum chemistry (MP2/6-31G*) Hartree Fock calculations.

Overall agreement of LDAP-PW with experiment and MP2 calculations is excellent. Average deviations from experiment and MP2 are 0.030Å and 0.034Å for bond lengths and 0.5 degrees and 1.0 degrees for bond angles. If the hydrogen-bonded system 3-hydroxy-acrylaldehyde is not included in the averages, the bond-length deviations become 0.017Å and 0.024Å respectively.

Upon closer examination, certain trends become apparent within the data contained in Table I. The most striking pattern is that a LDAP-PW calculation of a bond distance between two heavy (non-hydrogen) atoms is almost always closer to experiment than the corresponding MP2 result. Conversely, bonds involving at least one hydrogen are almost always calculated more accurately using MP2. In addition, bond angles which include zero or one hydrogen atom are almost always more accurate using LDAP-PW, while those including two hydrogens are usually better reproduced by MP2. We believe that these effects are due to the use of the LDA rather than a more accurate exchange-correlation functional. The small size of hydrogen makes its charge density change over a short length scale. It appears likely that gradient corrections to LDA will improve these results. Another trend which we have observed is that long bonds are reproduced more poorly than short bonds by the LDAP-PW. This effect is also probably due to the use of the LDA. As the atoms in a bond separate, they act more like free atoms, and the LDA does a poorer job on free atoms than on covalent materials. This effect is particularly striking in the O-O bond of H₂O₂ and the hydrogen bond in 3-hydroxyacrylaldehyde.

These results show that the LDAP-PW method can produce accurate structural parameters for molecules. The data suggest that the method which uses plane waves, pseudopotentials, and supercells may be a useful alternative to standard *ab initio* quantum mechanical methods for calcula-

Molecule	Parameter	Exp	MP2	Δ^1_e	LDAP-PW	Δ^2_e	Δ_G
H ₂	r(HH)	0.742	0.738	0.004	0.776	0.034	0.038
O ₂	r(OO)	1.208	1.242	0.034	1.183	0.025	0.059
N ₂	r(NN)	1.098	1.131	0.033	1.099	0.001	0.032
P ₂	r(PP)	1.893	1.936	0.043	1.875	0.018	0.061
CO	r(CO)	1.128	1.151	0.023	1.138	0.010	0.013
CO ₂	r(CO)	1.162	-	-	1.170	0.008	-
H ₂ O	r(OH)	0.958	0.969	0.011	0.976	0.018	0.007
	<(HOH)	104.5	104.0	0.5	104.0	0.5	0.0
CH ₄	r(CH)	1.092	1.090	0.002	1.102	0.010	0.012
NH ₃	r(NH)	1.012	1.017	0.005	1.028	0.016	0.011
	<(HNN)	106.7	106.3	0.4	105.7	1.0	0.6
PH ₃	r(PH)	1.420	1.415	0.005	1.440	0.020	0.025
	<(HPH)	93.3	94.6	1.3	91.6	1.7	3.0
H ₂ O ₂	r(OO)	1.452	1.467	0.015	1.414	0.038	0.053
	r(OH)	0.965	0.976	0.011	0.982	0.017	0.006
	<(OOH)	100.0	98.7	1.3	100.2	0.2	1.5
	ω (HOOH)	119.1	121.3	2.2	118.7	0.4	2.6
N ₂ H ₂	r(NN)	1.252	1.267	0.015	1.233	0.019	0.034
	r(NH)	1.028	1.036	0.008	1.052	0.024	0.016
	<(NNH)	106.9	105.4	1.5	107.2	0.3	1.8
H ₂ CO	r(CO)	1.208	1.221	0.013	1.205	0.003	0.016
	r(CH)	1.116	1.104	0.012	1.135	0.019	0.031
	<(HCH)	116.5	115.6	0.9	116.4	0.1	0.8
C ₂ H ₂	r(CC)	1.203	1.218	0.015	1.196	0.007	0.022
	r(CH)	1.061	1.066	0.005	1.058	0.003	0.008
HNC	r(NC)	1.169	1.187	0.018	1.178	0.009	0.009
	r(HN)	0.994	1.002	0.008	1.018	0.024	0.016
HNO	r(NO)	1.212	1.237	0.025	1.188	0.024	0.049
	r(HN)	1.063	1.058	0.005	1.093	0.030	0.035
	<(HNO)	108.6	107.3	1.3	109.2	0.6	1.9
Formamide (HCONH ₂)	r(CO)	1.193	1.224	0.031	1.217	0.024	0.007
	r(CN)	1.376	1.361	0.015	1.365	0.011	0.004
	<(OCN)	124.7	124.8	0.1	124.9	0.2	0.1
Glycine (NH ₂ CH ₂ CO ¹ O ² H)	r(C=O ¹)	-	1.218	-	1.204	-	0.014
	r(CO ²)	-	1.358	-	1.345	-	0.013
	r(CC)	-	1.515	-	1.535	-	0.020
	r(NC)	-	1.451	-	1.460	-	0.009
	<(O ¹ CO ²)	-	123.2	-	123.7	-	0.5
	<(O ² CC)	-	111.4	-	111.9	-	0.5
	<(O ¹ CC)	-	125.4	-	124.4	-	1.0
	<(CCN)	-	114.9	-	114.8	-	0.1
H ₂ PO ₄ ⁻¹	r(PO)	-	1.510	-	1.482	-	0.028
	r(P-OH)	-	1.680	-	1.640	-	0.040
	<(HO-P-OH)	-	101.1	-	101.2	-	0.1
	<(O-P-OH)	-	106.9	-	107.1	-	0.2
	<(O-P-O)	-	126.2	-	125.2	-	1.0
3-hydroxy- acrylaldehyde (HOCHCHCHO)	r(O-H)	0.969	0.964	0.025	1.079	0.110	0.085
	r(O...H)	1.680	1.664	0.014	1.418	0.262	0.276

Table I. A comparison of LDAP-PW geometry optimizations with experiment and with MP2. Δ^1_e and Δ^2_e are the deviations of the MP2 and LDAP-PW calculations from experiment, and Δ_G is the deviation of LDAP-PW from the MP2 values.

tions on chemical systems. Future work will include more realistic density functionals and tests of energetics of chemical transformations. In addition, research is continuing to develop more efficient energy minimization algorithms and superior pseudopotentials. These changes will improve the efficiency and accuracy of the method for the study of periodic and aperiodic chemical and biochemical systems.

4.4 Publications

- Alerhand, O., J. Wang, J.D. Joannopoulos, E. Kaxiras, and R. Becker. "Adsorption of As on Stepped Si(100): Resolution of the Sublattice Dilemma." *Phys. Rev. Rapid Comm.* B44: 6534 (1991).
- Alerhand, O., J. Wang, J.D. Joannopoulos, and E. Kaxiras. "Growth of As Overlayers on Vicinal Si(100)." *J. Vac. Sci. Tech.* B9: 2423 (1991).
- Arias, T., M. Payne, and J.D. Joannopoulos. "Precise and Efficient Ab-Initio Molecular Dynamics." *Phys. Rev. B.* Forthcoming.
- Joannopoulos, J.D., P. Bash and A. Rappe. "Modern Iterative Minimization Techniques in Quantum Chemistry." *Chem. Des. Automat. News* 6(8): pages (1991).
- Rappe, A., and J.D. Joannopoulos. "The Design of Convergent and Transferable Ab-Initio Pseudopotentials." *Proceedings of the Nato Advanced Study Institute*, Aussois, France, 1991.
- Rappe, A., J.D. Joannopoulos and P. Bash. "A Test of the Planewaves for the Study of Molecules from First Principles." *J. Amer. Chem. Soc.* Forthcoming.
- Wang, J., M. Needels, and J.D. Joannopoulos. "Surface and Fracture Energies in GaAs." In *Surface Physics and Related Topics*. Teaneck, New Jersey: World Scientific Publ., 1991. pp. 314.

Chapter 5. Epitaxy and Step Structures on Semiconductor Surfaces

Academic and Research Staff

Professor Simon G.J. Mochrie, Dr. Kenneth I. Blum

Graduate Students

Douglas L. Abernathy

5.1 Structure and Phase Behavior of the Si(113) Surface

Sponsor

Joint Services Electronics Program
Contract DAAL03-89-C-0001
Contract DAAL03-92-C-0001

Recently, our efforts under JSEP have been directed towards implementation of a design for an ultra-high-vacuum (UHV) chamber for surface x-ray scattering. The design and assembly of the UHV chamber and its associated diffractometer are now complete, and a first set of experiments using the new chamber at the MIT-IBM Beamline (X20) at the National Synchrotron Light Source has been carried out.

Our initial program (in collaboration with R.J. Birgeneau) is to study the Si(113) surface.¹ Si(113) is interesting for a number of reasons, which involve both possible technological applications and interest in the basic physics of surfaces. Firstly, we note that Si(113) is a stable facet with a surface energy comparable to that of the (111) or (001) orientation.² Reports of superior epitaxial growth on Si(113)³ make the structure of this surface and its temperature dependence especially worthy of study.

An unreconstructed (113) surface may be envisaged as a sequence of (001) terraces separated by (111) steps. (The terraces are a single atomic row wide.) The corresponding surface unit cell contains two different types of surface atom: two-fold coordinated atoms deriving from the (001) terrace with two dangling bonds and three-fold coordinated atoms from the (111) step with a single dangling bond (see figure 1, which is taken from the article by Myles and Jacobi⁴). As noted by others before,⁵ this aspect of the (113) surface leads to the possibility of two different adsorption sites. This feature may alleviate the problem of twinning that occurs in the growth of III-V semiconductors on flat Si(001).⁶ Furthermore, in a III-V material, the (113) surface is non-polar, in contrast to the (001) and (111) surfaces, which makes it especially interesting for heteroepitaxy.

The clean Si(113) surface reconstructs to form either a (1x3) or a (2x3) surface mesh. The (1x3) structure appears to be the equilibrium configuration,⁷ but the precise atomic geometry of the Si(113) (1x3) reconstruction has yet to be established experimentally. Moreover, convincing calculations of the structure of Si(113) do not currently exist. At elevated temperatures ($\geq 840\text{K}$), the surface reverts from its (1x3) structure to a structure with true (1x1) symmetry of bulk (113)

¹ B.F. Olshanetsky and V.I. Mashanov, *Surf. Sci.* 111: 414 (1981); D.J. Chadi, *Phys. Rev. B* 29: 785 (1984).

² J.M. Gibson, M.L. McDonald, and F.C. Unterwald, *Phys. Rev. Lett.* 55: 1765 (1985).

³ G.H. Olsen, T.J. Zamerowski, and F.Z. Hawrylo, *J. Cryst. Growth* 59: 654 (1982); S.L. Wright, M. Inada, and H. Kroemer, *J. Vac. Sci. Technol.* 21: 534 (1982).

⁴ U. Myles and K. Jacobi, *Surf. Sci.* 220: 353 (1989).

⁵ D.J. Chadi, *Phys. Rev. B* 29: 785 (1984); U. Myles and K. Jacobi, *Surf. Sci.* 220: 353 (1989); J. Knall, J.B. Pethica, J.D. Todd, and J.H. Wilson, *Phys. Rev. Lett.* 66: 1733 (1991).

⁶ K. Fujikawa, *J. Cryst. Growth* 77: 509 (1986).

⁷ Y.N. Yang, E.D. Williams, R.L. Park, N.C. Barlett, and T.L. Einstein, *Phys. Rev. Lett.* 64: 2910 (1991).

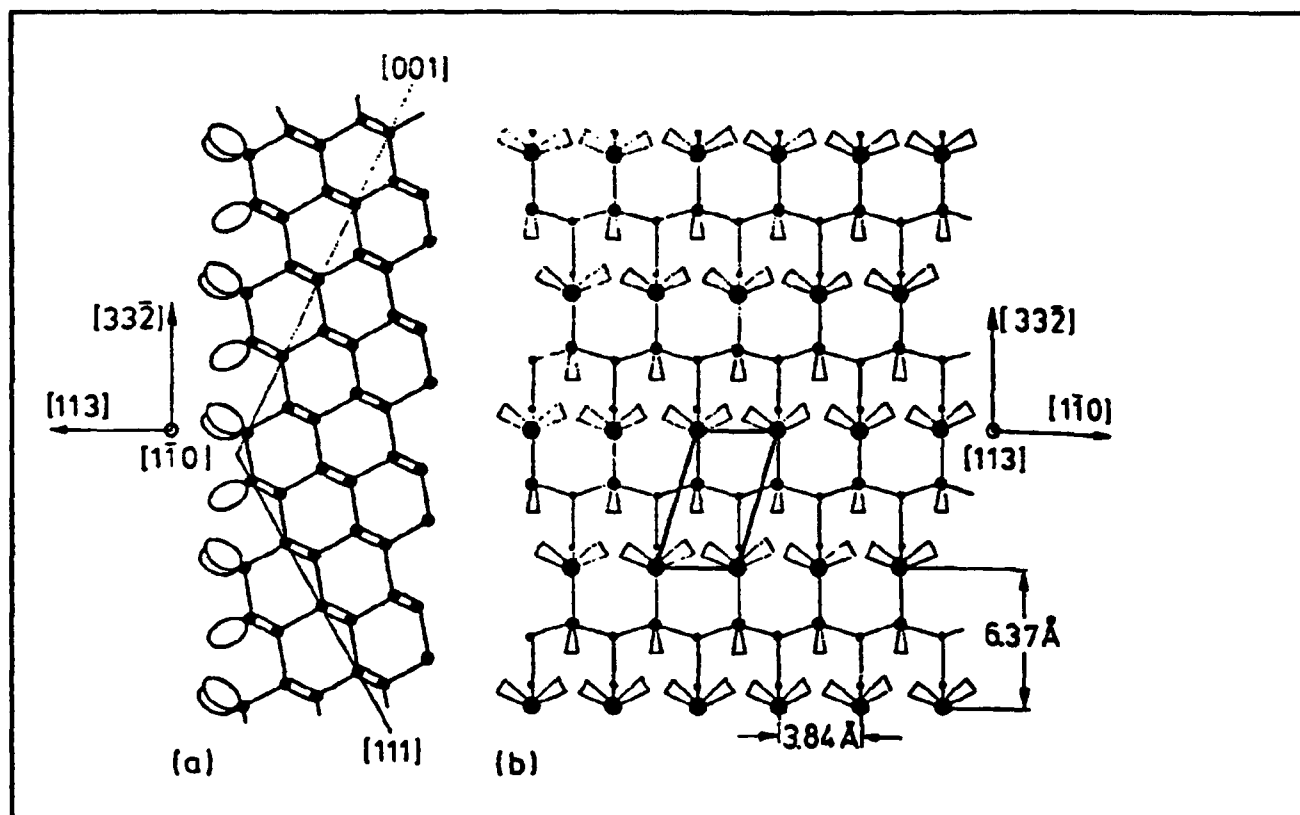


Figure 1.

planes.⁷ It has been suggested that the phase transformation between these two surface configurations falls into a particular "universality class," that of the chiral, three state Potts model.⁸ Our initial experiments, aimed at studying this aspect, were carried out on a (1x3) reconstructed surface, produced by annealing at 1500 K and subsequently cooling to below the (1x3)-to-(1x1) transformation temperature (≥ 840 K). The presence of commensurate "1/3-order" rods, located between the rods of scattering associated with bulk periodicities, indicates a (1x3) reconstruction of the crystal surface. A scan across one such rod—the (4,2/3) rod (we employ the units of the unreconstructed surface unit cell)—is shown for several temperatures in figure 2 on a logarithmic intensity scale. The lowest profile shown corresponds to a temperature of 750 K. Evidently, the reconstruction is readily observable. In addition, the width of this profile determines that the reconstruction is translationally well-ordered on length

scales of ≈ 4000 Å. (Other measurements establish that the existence of peaks associated with a (2x3) structure is excluded at the 10^{-4} level.) The additional profiles in figure 2 illustrate the behavior observed on warming through the phase transformation. The commensurate 1/3-order rod becomes weaker, and at the same time a broad, incommensurate peak may be seen emerging towards smaller wave vector (smaller K). Least-mean-squares fits (solid lines) reveal that the width of the incommensurate peak is proportional to its displacement from the commensurate position, suggesting that the disordering indeed falls within the universality class proposed.

Experiments to investigate the detailed atomic structure in the commensurate phase are planned for the near future. Another interesting possibility is that of surface roughening, which may occur at very high temperatures. Experiments to investigate this aspect are also forthcoming.

⁸ Y.N. Yang, E.D. Williams, R.L. Park, N.C. Barlett, and T.L. Einstein, *Phys. Rev. Lett.* 64: 2910 (1991); D.A. Huse and M.E. Fisher, *Phys. Rev. B* 29: 239 (1984).

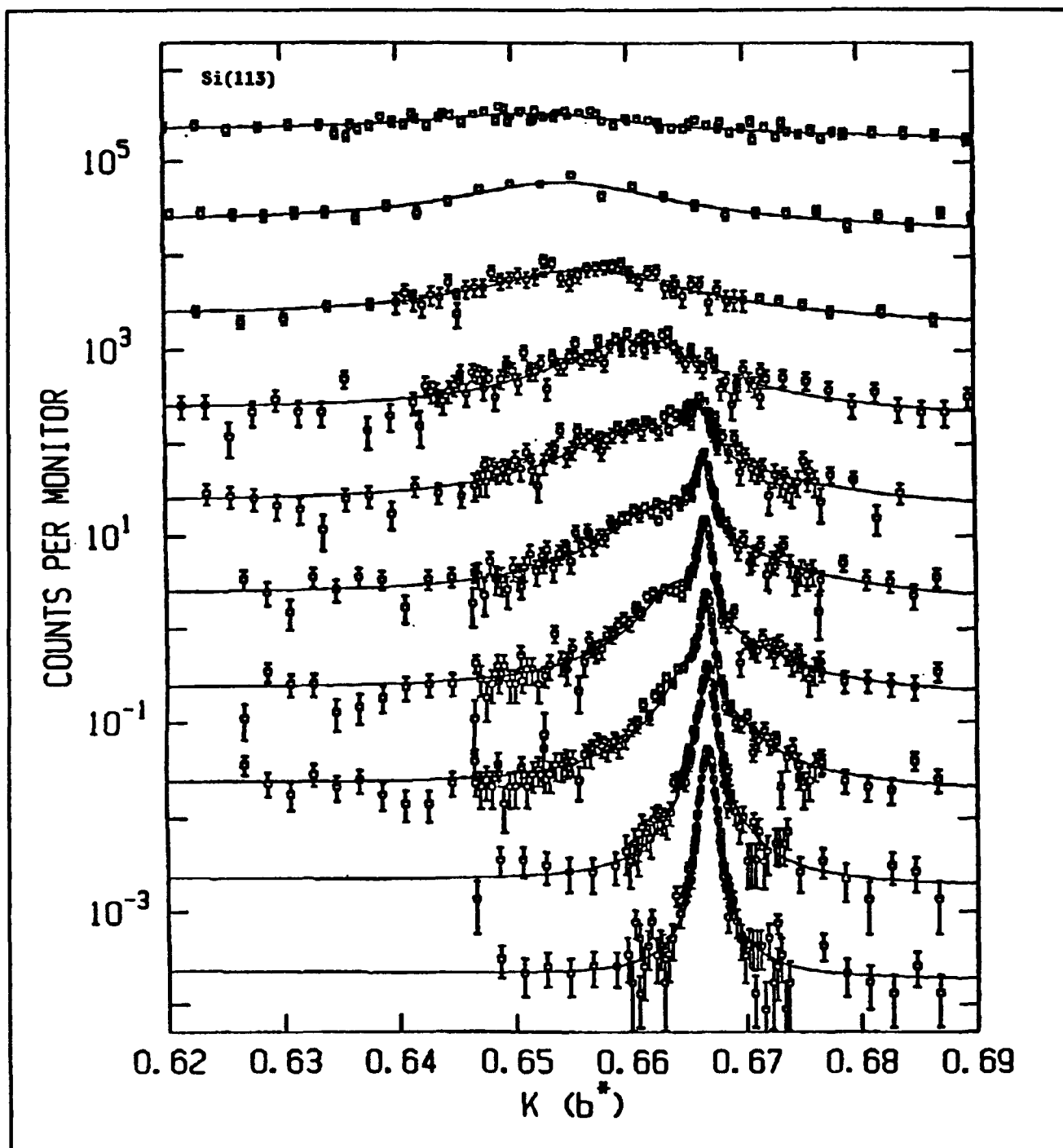


Figure 2.

Publications

Abernathy, D.L., S.G.J. Mochrie, D.M. Zehner, G. Grübel, and D. Gibbs. "Orientational Epitaxy and Lateral Structure of the Hexagonally Reconstructed Pt(001) and Au(001) Surfaces." *Phys. Rev. B* 45 (1992). Forthcoming.

Gibbs, D., G. Grübel, D.M. Zehner, D.L. Abernathy, and S.G.J. Mochrie. "Orientational Epitaxy of the Hexagonally Reconstructed Pt(001) Surface." *Phys. Rev. Lett.* 67: 3117 (1991).

2.2 Millimeter-Wave Frequency Measurement of the Rydberg Constant

Sponsors

Joint Services Electronics Program
Contract DAAL03-89-C-0001
Contract DAAL03-92-C-0001
National Science Foundation
Grant PHY 89-19381

Project Staff

Pin P. Chang, Jeffrey R. Holley, Robert P. Lutwak,
Scott N. Paine, Dr. Theodore W. Ducas, Professor
Daniel Kleppner

The Rydberg constant, R_∞ , relates the wavelengths of the spectrum of atomic hydrogen to practical laboratory units. As such, R_∞ is the natural unit for measurements of numerous atomic properties. Experiments using laser spectroscopy have determined R_∞ to nearly 1 part in 10^{10} .⁴ Although R_∞ is the most accurately measured fundamental constant, high-precision experiments which depend on R_∞ as an auxiliary constant demand a more accurate determination. For example, new experiments to determine the Lamb shift in the ground state of atomic hydrogen will be limited by uncertainties in R_∞ . The accuracy of optical measurements has reached the limit of precision of wavelength metrology. Further progress in measuring R_∞ requires a frequency measurement, making use of the modern definition of length in terms of time intervals and the defined speed of light.

We are attempting to advance the accuracy of R_∞ by directly measuring cR_∞ , the "Rydberg frequency." By initially preparing highly excited "Rydberg" states of atomic hydrogen, we are able to measure millimeter-wave transitions to nearby states with the full precision of frequency metrology.

The goal of our experiment is three-fold. First is the evaluation of cR_∞ . Second is the measurement of the ground state Lamb shift. Because our measurements involve high angular momentum states for which the Lamb shift is extremely small, a comparison of our results with optical measurements of transitions between low-lying states will yield an improved measurement of the Lamb shift.

Third is the precise frequency calibration of the spectrum of hydrogen to provide an independent check on forthcoming optical frequency measurements based on laser spectroscopy.

Our experiment is performed in an atomic beam configuration to provide a long interaction time and reduce Doppler and collisional perturbations. Atomic hydrogen is excited to the state ($n=29, m=0$) by two-photon stepwise absorption. The atoms are then transferred to the longer lived "circular" state ($n=29, m=28$) by the method of crossed electric and magnetic fields.⁵ The atoms then enter a region of uniform fields in which the frequency of the transition ($n=29, m=28$) \rightarrow ($n=30, m=29$) is measured. The atoms interact with the millimeter-wave radiation at two locations in a Ramsey separated oscillatory fields geometry. The final state distribution of the atoms is measured by a state-selective electric field ionization detector. The resonance signal is observed as a transfer of atoms from the $n=29$ state to the $n=30$ state as the millimeter wave frequency is tuned across the transition.

Figure 4 illustrates the main features of the apparatus. Atomic hydrogen or deuterium is produced by dissociation of H_2 or D_2 in a radio frequency discharge. The beam is cooled by collisions with the walls of a cryogenically cooled thermalizing channel in order to slow the beam and thereby increase the interaction time. The atoms are excited to the state ($n=29, m=28$) by two-photon stepwise excitation in the circular state production region. The development of the hydrogen beam and optical systems was described in the 1990 *RLE Progress Report Number 133*. The magnetic field necessary to transfer the atoms to the circular state is provided by permanent magnets. The electric field is produced by an arrangement of strip electrodes that causes the direction of the field to rotate. A detector in the circular state production region monitors the efficiency of the laser excitation and momentum transfer processes.

After the atoms are prepared in the circular state, the beam enters the interaction region. Because Rydberg atoms interact strongly with external fields, accurate measurement of the energy level structure requires careful control of the interaction environment. Thermal radiation is reduced by cooling the interaction region to ~ 10 K by a liquid helium flow system. The ambient magnetic field is shielded by a double-wall high permeability

⁴ M.G. Boshier et al., *Phys. Rev. A* 40: 6169 (1989); P. Zhao et al., *Phys. Rev. A* 39: 2888 (1989); F. Biraben et al., *Phys. Rev. Lett.* 62: 621 (1989).

⁵ D. Delande and J.C. Gay, *Europhys. Lett.* 5: 303 (1988).

shield. The small electric field, necessary to define the quantization axis of the atoms, is applied with high uniformity by field plates with corrective strip electrodes along the sides. The millimeter waves intersect the atomic beam at two locations separated by 50 cm. The millimeter-wave optics were described in the 1990 *RLE Progress Report Number 133*.

The state distribution of the atoms emerging from the interaction region is analyzed by an electric field ionization detector. The atoms enter a region of increasing electric field produced by a ramped plate held at constant potential. The atoms in the state ($n=30$), which ionize at lower field, are collected in the first detector, while atoms in the state ($n=29$), which ionize at higher field, are collected at the second detector. An important feature of the detector is that it provides time resolution. The atomic beam is pulsed, and the time-resolved

signal from the detector allows different velocity classes to be observed independently.

During this past year we have observed millimeter wave transitions in each of the two millimeter wave beams. In this fashion, we have observed the ($n=29 \rightarrow n=30$) transition in both hydrogen and deuterium, as well as the ($n=27 \rightarrow n=28$) transition in hydrogen. A typical resonance signal is shown in figure 5. In addition, we have observed "Rabi oscillations" in each of the millimeter wave beams. Recently, we have begun experiments to study signals from interactions with both millimeter-wave beams in the Ramsey separated oscillatory fields geometry. Sample interference data is shown in figure 6.

Improvements to increase the signal-to-noise ratio are underway, and we anticipate starting on high accuracy measurements in the coming year.

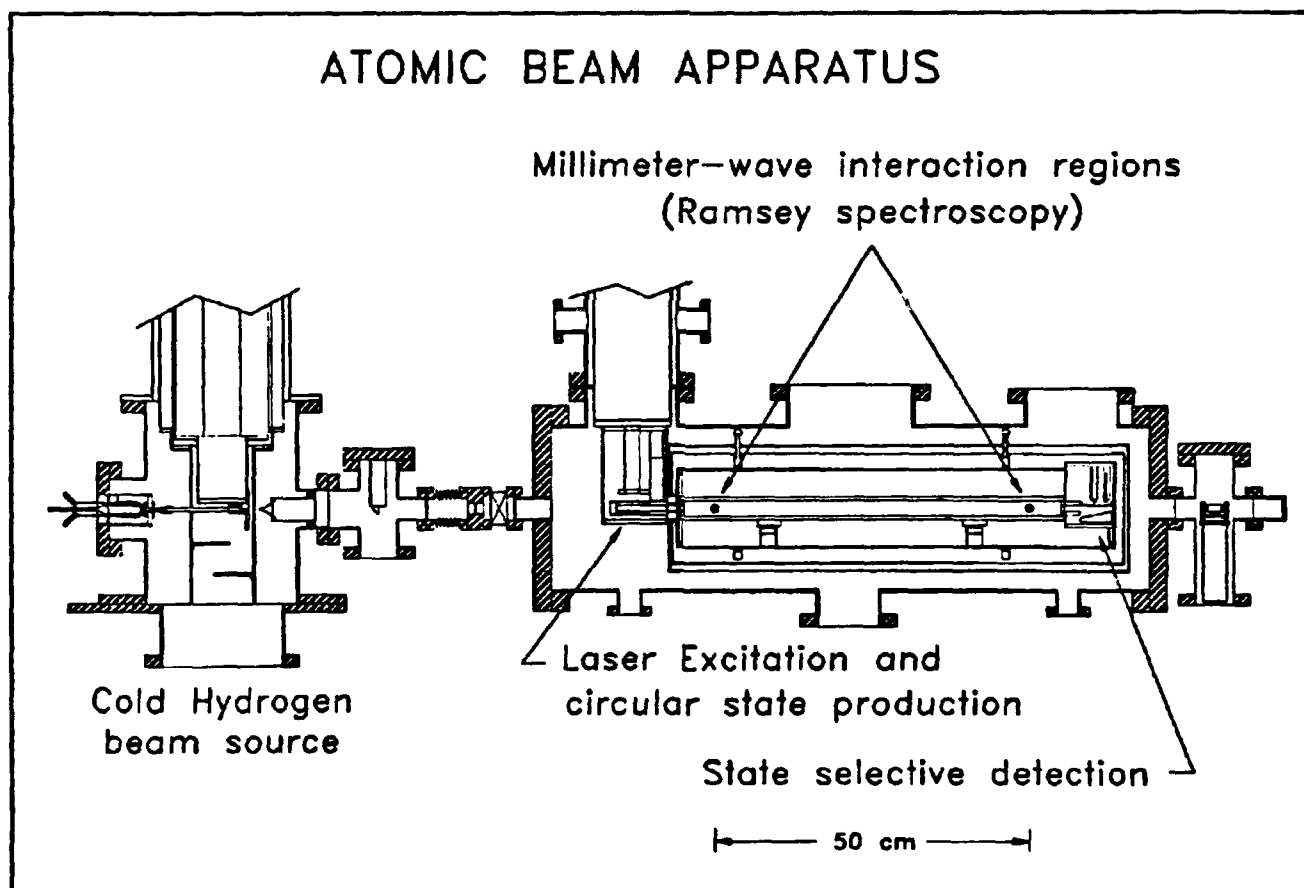


Figure 4. Schematic diagram of the atomic beam apparatus.

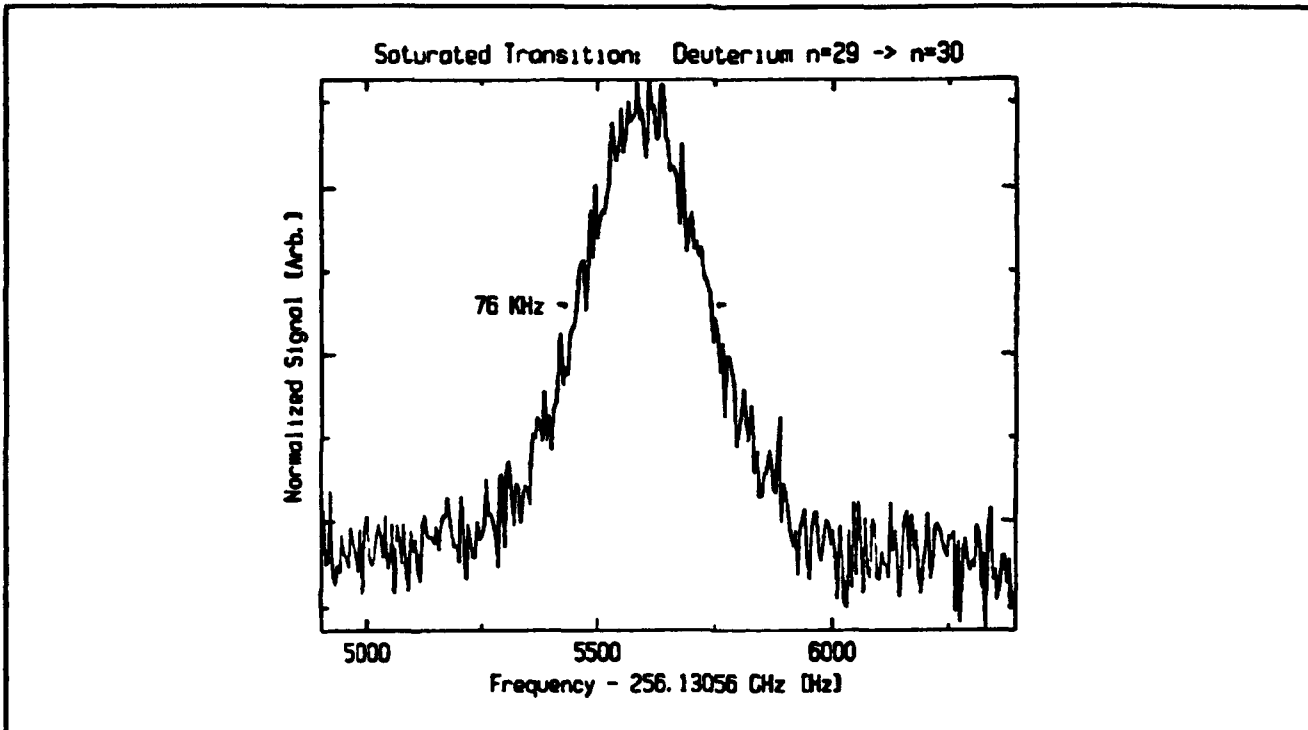


Figure 5. Typical signal for the $(n=29, m=28) \rightarrow (n=30, m=29)$ transition in atomic deuterium. The width of the resonance line is close to the time-of-flight limit as the atoms cross the millimeter wave beam.

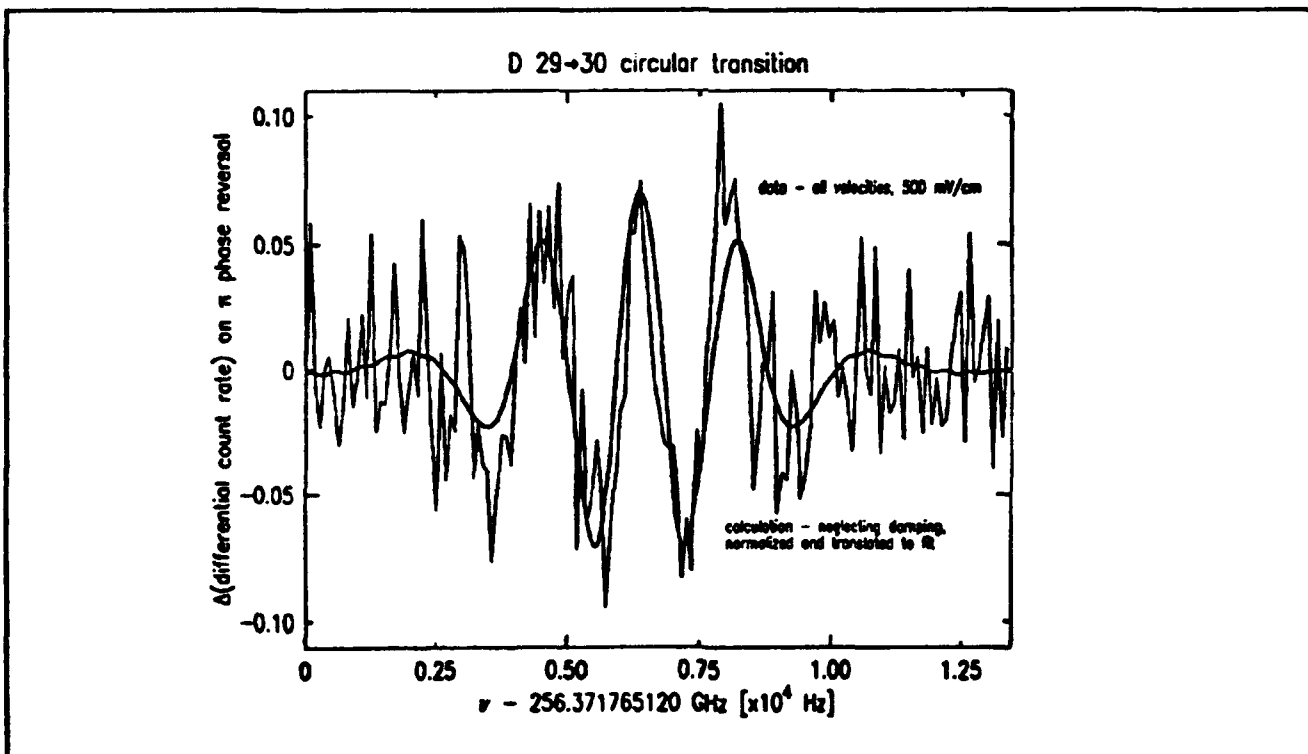


Figure 6. First results for the a narrow linewidth "Ramsey" fringe for the transition $n=29, m=28 \rightarrow n=30, m=29$ in deuterium.

2.3 Atom Interferometry

Sponsors

Joint Services Electronics Program
Contract DAAL03-89-C-0001
Contract DAAL03-92-C-0001
U.S. Army Research Office
Contract DAAL03-89-K-0082
U.S. Navy - Office of Naval Research
Grant N00014-89-J-1207

Project Staff

John E. Berberian, Christopher R. Ekstrom, Troy D. Hammond, David W. Keith, Marc-Oliver Mewes, Dr. H. Joerg Schiedmeyer, Quentin A. Turchette, Professor David E. Pritchard

During 1991, we demonstrated the first atom interferometer.⁶ Using transmission gratings, which we fabricated,⁷ as optical elements for atom deBroglie waves, we constructed a three grating atom interferometer which physically separates atom waves before recombining them. Our demonstration was closely followed by two demonstrations of atom interferometers which used laser light as the beam splitters.⁸

Atom interferometers will make possible qualitatively new types of experiments involving inertial effects, studies of atomic and molecular properties, and tests of fundamental physics, and may ultimately open the way to making ultra-small structures using atom holograms.

- The relatively large mass and low velocity of atoms makes atom interferometers especially sensitive to inertial effects such as rotation, acceleration, and gravity. Sagnac rotation has been observed in agreement with theoretical predictions,⁹ and sensitivity to gravitational acceleration at the 3×10^{-6} level has been demonstrated.¹⁰ Atom interferometers may become the best absolute accelerometers and gravimeters in the next few years.
- Atom interferometers can be applied to a number of experiments in fundamental physics: tests of quantum mechanics such as the Aharonov-Casher effect,¹¹ measurement of the equality of proton and electron charges, and a precise measurement of the momentum of a photon. This latter measurement should produce a new high precision value for the fundamental constants $N_A \hbar$.
- Interferometers for atoms and molecules will offer more accurate ways to measure intrinsic properties of these particles, like their polarizability. They will also open up new areas of study, such as measurements of the "index of refraction" of a gas for a particle beam which passes through it.

Our interferometer consists of three 400 nm period transmission gratings, mounted 0.66 m apart on separate translation stages inside the vacuum envelope. During operation, the 0th and 1st order beams from the first grating strike the middle grating (which is 140 μm wide) where they are diffracted in the 1st and -1st orders so that they converge at the third grating. At the second (middle) grating the beams have widths of 30 μm (FWHM) and are separated by 27 μm . The first two gratings form an interference pattern in the plane of the third grating, which acts as a mask to sample this pattern. The detector, located 0.30 m beyond the third grating, records the flux transmitted by the third grating. Figure 7 shows the design of the interferometer.

The data necessary to determine the interferometer phase contrast are acquired by modulating the position of one grating relative to the other two and simultaneously recording the signal from the atom counting electronics as well as the signal from an optical interferometer used to measure the relative position of the gratings. After removing data obscured by noise spikes from the hot wire, the atom count rate data are averaged into bins according to relative grating position, resulting in the fringe pattern shown in figure 8.

⁶ D.W. Keith, C.R. Ekstrom, Q.A. Turchette, and D.E. Pritchard, *Phys. Rev. Lett.* 66: 2693 (1991).

⁷ D.W. Keith and M.J. Rooks, *J. Vac. Sci. Technol. B* 9: 2846 (1991).

⁸ F. Riehle, T. Kisters, A. Witte, J. Helmcke, and J. Borde, *Phys. Rev. Lett.* 67: 177 (1991); M. Kasevich and S. Chu, *Phys. Rev. Lett.* 67: 181 (1991).

⁹ F. Riehle, T. Kisters, A. Witte, J. Helmcke, and J. Borde, *Phys. Rev. Lett.* 67: 177 (1991).

¹⁰ M. Kasevich, S. Chu, *Phys. Rev. Lett.* 67: 181 (1991).

¹¹ Y. Aharonov and A. Casher, *Phys. Rev. Lett.* 53: 319 (1984).

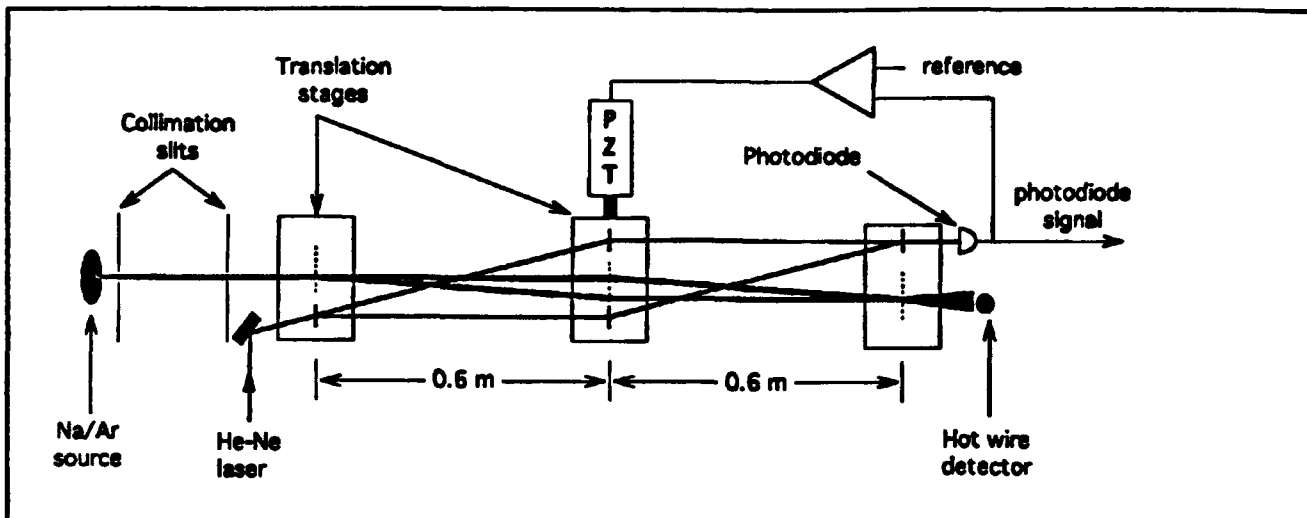


Figure 7. Our current atom interferometer with laser interferometer stabilization system (Not to scale).

The peak-to-peak amplitude of our interference signal is 70 Hz, which enables us to determine the interferometer phase to a precision of 0.1 rad in 1 min. The excellent long-term stability of our position stabilization system provides measured atom-interferometer phase drift of less than 0.1 rad over 10 minutes.

The key component of our interferometer is the set of three matched transmission diffraction gratings which we constructed during two visits at the National Nanofabrication Facility (NNF) at Cornell University. The first trip resulted in the development of a new process for fabricating atom optics. The process allows fabrication of precisely positioned openings in thin silicon nitride membranes mounted in silicon frames. The pattern created in the membrane is determined by an electron beam writer, making the process quite versatile. This process was used to create the diffraction gratings used in the interferometer. In addition, several zone plates (atom lenses) were also built and successfully demonstrated later. During our second trip, we devised ways to reduce the electron beam writing time. This decreased thermal drift during the writing period assured higher overall accuracy and also increased our overall productivity. We made a wide variety of diffraction gratings with various heights and periods between 100 and 300 nm as well as an assortment of single and double slits.

We have recently started construction of an interaction region that will allow us to perform several experiments including measurement of the Aharonov-Casher phase shift, the electric polarizability of the ground state of sodium, and the index

of refraction for sodium passing through noble gas atoms.

The scientific future of atoms interferometers looks bright: (1) Atom beam sources are inexpensive and intense relative to other particle beams/sources (e.g., neutrons, electrons), (2) several techniques have now been demonstrated to make interferometers for them, and (3) the atoms which may be used in them come with a wide range of parameters such as polarizability, mass, and magnetic moment. This assures the applicability of these instruments to a wide range of measurements of both fundamental and practical interest.

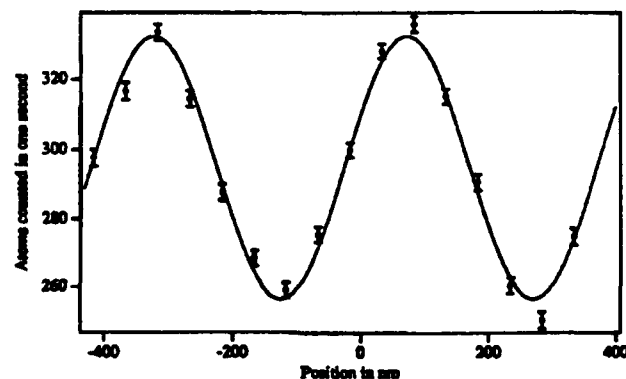


Figure 8. Interference signal from 400 seconds of data. Hot wire detector background of 40 Hz is subtracted. The solid line is a least squares fit to the data with a 400 nm period. The error bars are purely statistical and slightly underestimate the super-Poissonian character of the hot wire background.

Publications

Keith, D.W., C.R. Ekstrom, Q.A. Turchette, and D.E. Pritchard. "An Interferometer for Atoms." *Phys. Rev. Lett.* 66: 2693 (1991).

Keith, D.W., and M.J. Rooks. "Free-standing Gratings and Lenses for Atom Optics." *J. Vac. Sci. Technol. B* 9: 2846 (1991).

Pritchard, D.E. "Atom Interferometers." *Opt. Photonics News*, p. 19 (November 1991).

Pritchard, D.E. "Atom Optics." In *Atomic Physics* 12. Ed. J.C. Zorn, R.R. Lewis, and M. Weiss. New York: American Journal of Physics, 1991, pp. 165-170.

Turchette, Q.A., D.E. Pritchard, and D.W. Keith. "Numerical Model of a Multiple Grating Interferometer." Submitted to *J. Opt. Soc. Am. B* (1991).

Theses

Keith, D.W. *An Interferometer for Atoms*. Ph.D. diss. Dept. of Physics, MIT, 1991.

Turchette, Q.A. *Numerical Model of a Three Grating Interferometer for Atoms*. S.B. thesis. Dept. of Physics, MIT, 1991.

2.4 Cooling and Trapping Neutral Atoms

Sponsors

Joint Services Electronics Program
Contract DAAL03-89-C-0001
Contract DAAL03-92-C-0001
U.S. Navy - Office of Naval Research
Grant N00014-90-J-1642

Project Staff

Dr. Kristian Helmerson, Dr. Alexander Martin, Dr. Wolfgang Ketterle, Kendall Davis, Charles G. Freeman, Michael A. Joffe, Wan Morshidi, Peter S. Yesley, Professor David E. Pritchard

Our current objective is to develop an intense source of slow atoms which will be used in studies of cold collisions, atom optics and atom interferometry. Slow atoms sources typically have fluxes of a few times 10^9 atoms/sec. Improvements by two to three orders of magnitude seem feasible and are crucial for many experiments.

Experiments with dense samples of cold neutral atoms promise new exciting discoveries in basic and applied physics. Due to the considerably reduced thermal motion of atoms they are ideal for high resolution spectroscopy and for more accurate atomic frequency standards.

- Collisions of ultra-cold atoms in such samples are characterized by a long deBroglie wavelength and dominated by weak long-range interactions. Since the collision duration for slow atoms greatly exceeds the radiative decay time, stimulated and spontaneous radiative transitions can take place during the collision. Slow collisions are therefore radically different from fast collisions studied so far and will become an exciting new field of atomic physics.¹²
- High density samples of atoms open possibilities for observing quantum collective effects such as Bose-Einstein condensation and collectively enhanced or suppressed radiative decay.

In 1991, we designed and built two sources of cold atoms based on two different principles: a "Diffuse Light Slower" and an "Inverted Zeeman Slower." We also completed the data analysis and modeling of the laser spectroscopy and laser cooling experiments performed in a magnetic trap.¹³ In addition, one of us (K. Helmerson) completed his doctoral dissertation.¹⁴

The following discusses in more detail the progress made in the three areas mentioned above.

¹² P.S. Julienne and J. Vigu, "Cold Collisions of Ground- and Excited-state Alkali-metal Atoms," *Phys. Rev. A* 44: 4464 (1991).

¹³ K. Helmerson, A. Martin, and D.E. Pritchard, "Laser and rf Spectroscopy of Magnetically Trapped Neutral Atoms," submitted to *J. Opt. Soc. Am. B*; K. Helmerson, A. Martin and D.E. Pritchard, "Laser Cooling of Magnetically Trapped Neutral Atoms," submitted to *J. Opt. Soc. Am. B*.

¹⁴ K. Helmerson, *Laser Cooling and Spectroscopy of Magnetically Trapped Atoms*, Ph.D. diss., Dept. of Physics, MIT, 1991.

2.4.1 Slowing Atoms with Diffuse Light

We have demonstrated a new technique for slowing and brightening atomic beams which uses isotropic monochromatic laser light detuned to the red of the atomic resonance. The atoms compensate for the changing Doppler shift as they decelerate by absorbing photons at a variable angle in accordance with the Doppler resonance condition. The use of isotropic light and the automatic angle selection method of compensating for the changing Doppler shift distinguish diffuse light slowing from other light slowing schemes realized so far, and is technically simpler to implement.

In our experiments isotropic light was generated by shining laser light into a tube of diffusely reflecting material around the atomic beam (figure 9). Sodium atoms were slowed from approximately 300 m/s to below 100 m/s resulting in a continuous slow beam with a flux of greater than 10^9 atoms/s.¹⁵ This performance is comparable with other slowing schemes and is limited by the light losses in the diffuse reflector. We are currently working on ways to reduce the loss in the diffuse reflector well below its current 1 per cent.

Since isotropic light cools all components of the velocity, a diffuse light slower produces a slow beam with a smaller divergence. Other advantages of diffuse light slowing are the simple experimental realization, tolerance to laser jitter, and absence of an intense slowing laser beam collinear with the slowed atoms which can interfere with subsequent experiments.

2.4.2 Inverted Zeeman Slower

In a Zeeman slower the changing Doppler shift as an atom slows is compensated by the Zeeman shift in an inhomogeneous magnetic field. This method has the advantage of producing a continuous beam of slow atoms and featuring practically unlimited velocity capture range. The original implementation of Zeeman slowing, however, encountered difficulties in producing beams of atoms with velocities lower than 200 m/s. The major problems were off-resonant slowing of atoms after they left the slower and substantial

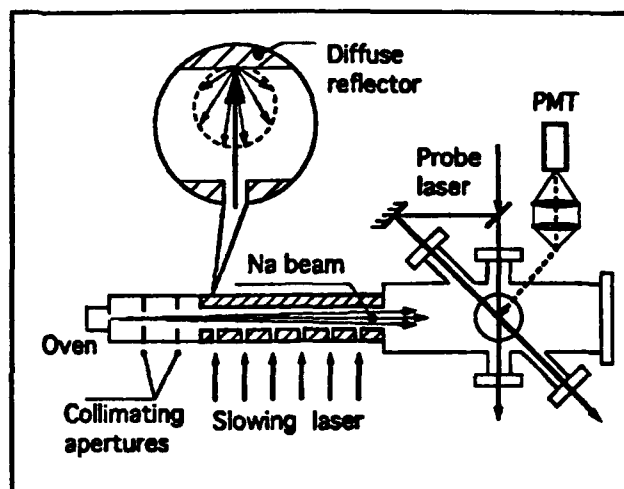


Figure 9. Schematic diagram of the experimental setup. A thermal sodium beam passes through the bore of a tube of diffusely reflecting material which is filled with laser light via six equally spaced small apertures. Fluorescence-excitation spectra produced by laser beams perpendicular and at 45° to the atomic beam are used to observe the velocity distribution of the atoms as they emerge from the diffuse light cavity.

spreading of the slow atomic beam due to transverse heating.

To solve the first problem we chose the $|F=2, m=2\rangle \rightarrow |F=3, m=3\rangle$ cycling transition to slow sodium atoms. The transition requires a magnetic field increasing along the atoms trajectory (Inverted Zeeman slower). The magnetic field drops off rapidly after reaching its maximum thus quickly shifting atoms out of resonance and reducing off-resonant slowing. It seems therefore possible to perform subsequent atomic optics experiments without undue interference from the intense slowing laser beam.

We have built and tested an inverse Zeeman slower which allows for optical access to the slow atoms inside. Transverse laser cooling will increase the brightness of the resulting slow atom beam. Experiments are still in progress but preliminary results indicate that the performance is better than any other slower demonstrated so far. We have slowed about 50 per cent of the thermal beam down to velocities between 40 m/s and 100 m/s. After optimization we intend to use the slower for efficient loading of an atom trap.

¹⁵ W. Ketterle, A.G. Martin, M. Joffe and D.E. Pritchard, "Slowing Atoms with Diffuse Laser Light," postdeadline paper, Seventh Interdisciplinary Laser Conference (ILS), Monterey, California, September 22-26, 1991.

2.4.3 Laser Cooling and Spectroscopy of Magnetically Trapped Neutral Atoms

During 1991, we concluded the data analysis and modeling of the experimental results obtained previously in a superconducting magnetic trap. This work can be divided into two parts:

1. Laser and rf spectroscopy of the trapped atoms:

Laser absorption, fluorescence and rf spectra of the trapped atoms were modeled and interpreted to extract the energy distribution of the trapped atoms. The results of our model show that the atoms, when loaded into the trap, had an effective temperature of ~ 50 mK, comparable to the actual trap depth. We have shown how the rf spectra can give the energy distribution of the trapped atoms without prior knowledge of the shape of the trapping field potential. For our experiments, the energy distribution of the trapped atoms was well described by a Boltzman distribution, truncated at the energy corresponding to the highest energy trapped atom.¹⁶

2. Laser Doppler cooling of the trapped atoms:

Our experiments have shown also how simple one-dimensional optical molasses can reduce the temperature of the trapped atoms to ~ 1 mK. The motion transverse to the cooling laser is cooled by the coupling between the different translational degrees of freedom provided by the trap. The cooling process was modeled, and the theoretical results show good qualitative agreement with the experimental data. The measurements indicated, and the model confirms, that for cooling rates that are low compared to the trap coupling time, ultimate temperatures a few times the Doppler limit can be achieved.¹⁷

Publications

Gould, P.L., P.J. Martin, G.A. Ruff, R.E. Stoner, J-L. Picque, and D.E. Pritchard. "Momentum Transfer to Atoms by a Standing Light Wave; Transition from Diffraction to Diffusion." *Phys. Rev. A* 43: 585 (1991).

Helmerson, K., A. Martin, and D.E. Pritchard. "Laser and rf Spectroscopy of Magnetically Trapped Neutral Atoms." Submitted to *J. Opt. Soc. Am. B*.

Ketterle, W., and D.E. Pritchard. "Trapping Ground State Atoms in Static Fields." Submitted to *App. Phys. B*.

Ketterle, W., A. Martin, M. Joffe, and D.E. Pritchard. "Slowing Atoms with Diffuse Laser Light." Submitted to *Phys. Rev. Lett.*

Theses

Freeman, C.G. *Diffuse Slowing of a Beam of Neutral Sodium Atoms*. S.B. thesis. Dept. of Physics, MIT, 1991.

Helmerson, K. *Laser Cooling and Spectroscopy of Magnetically Trapped Atoms*. Ph.D. diss. Dept. of Physics, MIT, 1991.

2.5 Precision Mass Spectroscopy of Ions

Sponsors

Joint Services Electronics Program
Contract DAAL03-89-C-0001
Contract DAAL03-92-C-0001
National Science Foundation
Grant PHY 86-05893
Grant PHY 89-21769

Project Staff

Kevin R. Boyce, Frank DiFilippo, James A. Grimm, Matthew J. Marjanovic, Vasant Natarajan, Professor David E. Pritchard

In 1991, we continued our program to substantially improve our precision mass measurement experiment. These improvements should allow us to reach a precision of about 10^{-11} in our mass measurements of individual atomic and molecular ions, the next step toward our ultimate goal of a few parts in 10^{12} . This capability will allow us to do a variety of experiments which address issues in both fundamental and applied physics, including:

¹⁶ K. Helmerson, A. Martin, and D.E. Pritchard, "Laser and rf Spectroscopy of Magnetically Trapped Neutral Atoms," submitted to *J. Opt. Soc. Am. B*.

¹⁷ K. Helmerson, A. Martin and D.E. Pritchard, "Laser Cooling of Magnetically Trapped Neutral Atoms," submitted to *J. Opt. Soc. Am. B*.

- The ${}^3\text{H}^+ - {}^3\text{He}^+$ mass difference, important in ongoing experiments to determine the electron neutrino rest mass;
- Determination of excitation and binding energies of atomic and molecular ions by weighing the small decrease in energy, $\Delta m = E_{\text{bind}}/c^2$;
- Determination of Avogadro's number N_A by weighing γ -rays—its accurate determination would permit the replacement of the "artifact" mass standard by an atomic mass standard; and
- Improvement of many traditional applications of mass spectroscopy by orders of magnitude improvement in both accuracy and sensitivity.

Our experimental approach is to measure ion cyclotron resonance on a single molecular or atomic ion in a Penning trap, a highly uniform magnetic field with axial confinement provided by weaker electric fields. We monitor the ion's oscillation along the magnetic field lines by detecting the currents induced in the trap electrodes. Working with only a single ion is essential because space charge from other ions leads to undesired frequency shifts. This work in trapping and precision resonance draws on techniques developed by Hans Dehmelt at the University of Washington and Norman Ramsey at Harvard, for which they shared the 1989 Nobel Prize.

We have developed techniques for driving, cooling, and measuring the frequencies of all three normal modes of Penning trap motion. Thus we can manipulate the ion position reproducibly to within 30 microns of the center of the trap, correcting for electrostatic shifts in the cyclotron frequency to great accuracy. We use a π -pulse method to coherently swap the phase and action of the cyclotron with the axial modes.¹⁸ Therefore, although we detect only the axial motion directly,

we can determine cyclotron frequency by measuring the phase accumulated in the cyclotron motion in a known time interval (figure 10).

In the past two years, we have built an entirely new Penning trap and detector, including a higher-Q resonant circuit and quieter RF SQUID, these have improved our signal-to-noise ratio by a factor of two. We have also constructed a new highly stable DC electric field supply, and added a pressure regulator to the liquid helium bath of our superconducting magnet to help stabilize the field. In addition, we have begun construction of ion optics and an external ion source that will allow us to make the ions in a discharge at room temperature and then load them into the trap. This will eliminate the problem of residual neutral gas in the trap when using volatile species such as hydrogen and helium, and should permit rapid cycling between two different ions which will dramatically increase measurement precision.

With all the improvements to the system, we foresee being able to resolve the existing 10 eV discrepancy between measurements of $m({}^3\text{H}) - m({}^3\text{He})$ in the next year. In addition, we plan to demonstrate a classical squeezing technique which should reduce the thermal fluctuations of our measurement by a factor of three to five. After that, we plan to continue development of techniques to measure two ions of different mass simultaneously. The two-ion technique in combination with the various improvements made over the last two years should lead to precision in the range of 10^{-11} .¹⁹

Publications

Cornell, E.A., K.R. Boyce, D.L.K. Fyngenson, and D.E. Pritchard. "Two Ions in a Penning Trap: Implications for Precision Mass Spectroscopy." *Phys. Rev. A*. Submitted for publication.

¹⁸ E.A. Cornell, R.M. Weisskoff, et al., *Phys. Rev. A* 41: 312 (1990).

¹⁹ E.A. Cornell, *Mass Spectroscopy Using Single Ion Cyclotron Resonance*, Ph.D diss., Dept. of Physics, MIT, 1990.

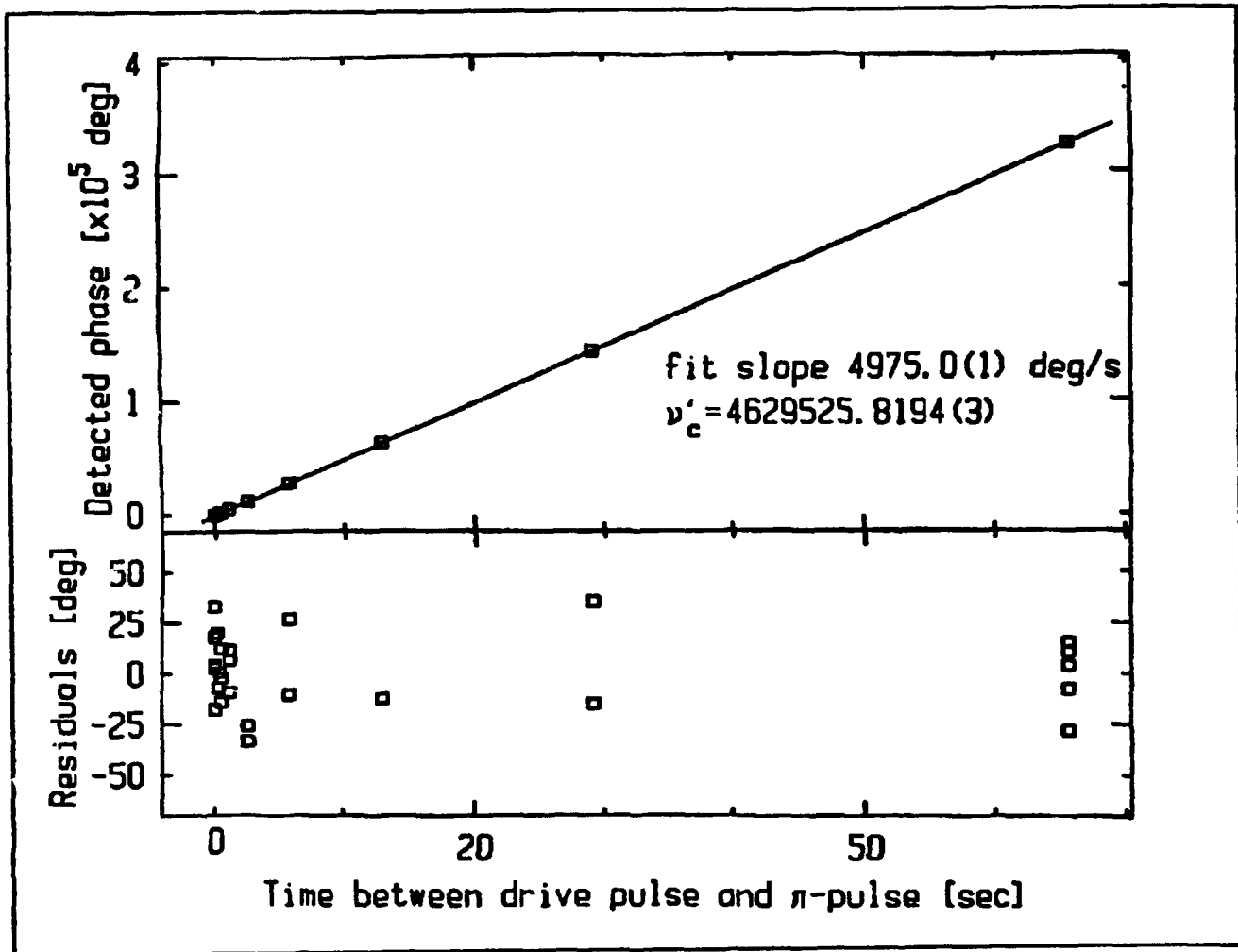


Figure 10. For each plotted point, we perform the following experiment: The initially cold ion is pulsed into a cyclotron orbit of known initial phase and then allowed to evolve "in the dark" for an indicated amount of time, t . Then a pulse is applied which exchanges cyclotron and axial motions, bringing the ion's cyclotron action and phase into the axial mode. As the ion's axial motion rings down, its phase is detected. The appropriate multiple of 360° is added, and a line is fitted to the points. The slope of the line is the frequency difference between the frequency generator and the trap cyclotron frequency.

Active MMW images are also generated using models and software from related projects. Preliminary simulation of 35 GHz sensor scene reveals the lack of depth information and resolution, but shows good weather penetration. Future work is required in the area of postprocessing in order to achieve better images.

1.3 Multilayer Media and Superconducting Electronics

Sponsors

Defense Advanced Research Projects Agency
Contract MDA972-90-C-0021
Digital Equipment Corporation
IBM Corporation
Joint Services Electronics Program
Contract DAAL03-89-C-0001
Contract DAAL03-92-C-0001
Schlumberger-Doll Research
U.S. Navy - Office of Naval Research
Grant N00014-90-J-1002
Grant N00014-89-J-1019

Project Staff

Professor Jin Au Kong, Dr. Robert T. Shin, Dr. Tarek M. Habashy, Dr. Sami M. Ali, Dr. Ying-Ching E. Yang, Dr. Soon Y. Poh, Dr. Herng A. Yueh, Dr. Son V. Nghiem, David M. Sheen, Robert G. Atkins, Hsiu C. Han, Jiqing Xia, Cheung-Wei Lam, Michael C. Moldoveanu, Hongsing Lee, Ilya Lyubomirsky

A method for the calculation of current distribution, resistance, and inductance matrices for a system of coupled superconducting transmission lines having finite rectangular cross-section is presented. These calculations allow accurate characterization of both high- T_c and low- T_c superconducting strip transmission lines. For a single stripline geometry with finite ground planes, the current distribution, resistance, inductance, and kinetic inductance are calculated as a function of the penetration depth for various film thicknesses. These calculations are then used to determine the penetration depth for Nb, NbN, and $YBa_2Cu_3O_{7-x}$ superconducting thin films from the measured temperature dependence of the resonant frequency of a stripline resonator. The calculations are also used to convert measured temperature dependence of the quality factor to the intrinsic surface resistance as a function of temperature for an Nb stripline resonator.

The frequency-dependent resistance and inductance of uniform transmission lines are calculated with a hybrid technique that combines a cross-section coupled circuit method with a surface inte-

gral equation approach. The coupled circuit approach is most applicable for low-frequency calculations, while the integral equation approach is best for high frequencies. The low-frequency method consists in subdividing the cross section of each conductor into triangular filaments, each with an assumed uniform current distribution. The resistance and mutual inductance between the filaments are calculated, and a matrix is inverted to give the overall resistance and inductance of the conductors. The high-frequency method expresses the resistance and inductance of each conductor in terms of the current at the surface of that conductor and the derivative of that current normal to the surface. A coupled integral equation is then derived to relate these quantities through the diffusion equation inside the conductors and Laplace's equation outside. The method of moments with pulse basis functions is used to solve the integral equations. An interpolation between the results of these two methods gives very good results over the entire frequency range, even when few basis functions are used. Results for a variety of configurations are obtained and are compared with experimental data and other numerical techniques.

A spectral domain dyadic Green's function formulation defining the fields inside a multilayer chiral medium due to arbitrary distribution of sources is developed. The constitutive parameters and the chirality of each layer are assumed to be different. The fields are obtained in terms of electric and magnetic type dyadic Green's functions. The singular behavior of these dyadic Green's functions in the source region is taken into account by extracting the delta function singularities. The fields in any layer are obtained in terms of appropriately defined global reflection and transmission matrices.

In order to understand the physical meaning of rational reflection coefficients in one-dimensional inverse scattering theory for optical waveguide design, we have studied the relation between the poles of the transverse reflection coefficient and the modes in inhomogeneous dielectrics. By using a stratified medium model, it is shown that these poles of the reflection coefficient have a one-to-one correspondence to the discrete modes, which are the guided and leaky modes. The radiation modes have continuous real values of transverse wave numbers and are not represented by the poles of the reflection coefficient. Based on these results, applications of the Gel'fand-Levitan-Marchenko theory to optical waveguide synthesis with the rational function representation of the transverse reflection coefficient are discussed.

We developed an inversion algorithm referred to as the Renormalized Source-Type Integral Equation

approach. The objective of this method is to overcome some of the limitations and difficulties of the iterative Born technique. It recasts the inversion, which is nonlinear in nature, in terms of the solution of a set of linear equations; however, the final inversion equation is still nonlinear. The derived inversion equation is an exact equation which sums up the iterative Neuman (or Born) series in a closed form and; thus, is a valid representation even in the case when the Born series diverges; hence, the name *Renormalized Source-Type Integral Equation (STIE) Approach*. This renormalized STIE approach has been applied to underground soil moisture inversion and formation inversion in the borehole geometry.

Several recent papers discuss techniques for reducing the parasitic circuit capacitance of millimeter-wave planar air bridge type GaAs Schottky barrier diodes by completely etching away the semi-insulating material under the active region and transferring the device to a second carrier that is better suited, both electrically and mechanically, to the intended high frequency application. This technique and a similar procedure are being explored as a means of producing a semi-integrated subharmonically pumped two-diode mixer for use in 640 GHz. For this application, a planar antiparallel diode pair is incorporated into the center of a pair of low pass microstrip filters formed on an insulating GaAs substrate. An appealing substitute for millimeter and submillimeter wavelength applications is fused quartz which has an order of magnitude lower loss tangent, one-third the dielectric constant, and is much more mechanically rigid than GaAs. Using known techniques, it is possible to thin an entire GaAs wafer to a thickness on the order of 1-3 microns and then transfer the remaining active layer onto quartz. An interesting question that arises as a result of this procedure is the effect of the ultrathin GaAs layer on the filter characteristics. A three-dimensional finite difference time domain (FD-TD) method is used to calculate the response of the filter both with and without the GaAs layer.⁸ It is shown that even a very thin layer of high dielectric constant material can have a noticeable effect on the filter response. The FD-TD analysis

agreed fairly well with measured response and could be used for subsequent design.

In the last few years there has been an increasing interest in the interaction of electromagnetic fields with chiral media. A chiral medium is a subset of the wider class referred to as bianisotropic. Such media are characterized by linear constitutive relations that couple the electric and magnetic field vectors by three independent scalars. A rigorous formulation deals with the problem of radiation of electric and magnetic sources embedded in a layered lossless chiral medium. The fields are obtained in terms of dyadic Green's functions of electric or magnetic type represented in two-dimensional spectral-domain form. First, the spectral domain dyadic Green's functions of electric and magnetic types for an unbounded chiral medium are derived. The singular behavior of the various dyadic Green's functions in the source region is investigated and taken into account by extracting the delta function singularities. Finally, introducing global upward and downward reflection and transmission matrices, the dyadic Green's functions in any layer of the stratified chiral medium are derived.

The growth of epitaxial Fe film on GaAs was first demonstrated using molecular beam epitaxy. Deposition of such films by ion-beam sputtering was reported and their application to microwave filters has previously been discussed. A theoretical analysis is performed to the analysis of a tunable band-stop filter using epitaxial Fe films on [011] GaAs, in which the Fe layer is part of a microstrip line that runs along either a [100] or a [110] direction, the easy and hard directions of magnetization of the Fe film, respectively.⁹ The analysis indicates that peak attenuation should occur at the ferromagnetic resonance (FMR) frequency and be proportional to the length of the microstrip line, and inversely proportional to the substrate thickness.

A rigorous approach to the problem of radiation of electric or magnetic sources in a stratified arbitrarily magnetized linear plasma.¹⁰ The fields are obtained in terms of dyadic Green's functions of electric or magnetic type represented in the spec-

⁸ P.H. Siegel, J.E. Oswald, R.G. Dengler, D.M. Sheen, and S.M. Ali, "Measured and Computed Performance of a Microstrip Filter Composed of Semi-Insulating GaAs on a Fused Quartz Substrate," *IEEE Microwave Guided Wave Lett.* 1(4): April (1991).

⁹ V.S. Liao, T.W. Stacey, S. Ali, and E. Schloemann, "Tunable Band-Stop Filter Based on Epitaxial Fe Film on GaAs," *Proceedings of the 1991 IEEE MTT-S International Microwave Symposium*, Boston, Massachusetts, June 11-14, 1991, pp. 957-960.

¹⁰ T.M. Habashy, S.M. Ali, J.A. Kong, and M.D. Grossi, "Dyadic Green's Functions in a Planar Stratified, Arbitrarily Magnetized Linear Plasma," *Radio Sci.* 26(3): 701-716 (1991).

tral domain. First, the dyadic Green's functions for an unbounded arbitrarily magnetized plasma is derived. The formulation is considerably simplified by using the KDB system of coordinates in conjunction with the Fourier transform. This leads to compact and explicit expressions for the dyadic Green's functions. The distributional singular behavior of the various dyadic Green's functions in the source region is investigated and taken into account by extracting the delta function singularities. Finally, the dyadic Green's function in any arbitrary layer is obtained in terms of appropriately defined global upward and downward reflection and transmission matrices. The field expressions for any arbitrary distribution of sources or linear antennas can be obtained by performing a convolution integral over the volume of the antenna weighted by the current density on the antenna.

The input impedance of a microstrip antenna consisting of two circular microstrip disks in a stacked configuration driven by a coaxial probe is investigated.¹¹ A rigorous analysis is performed using a dyadic Green's function formulation where the mixed boundary value problem is reduced to a set of coupled vector integral equations using the vector Hankel transform. Galerkin's method is employed in the spectral domain where two sets of disk current expansions are used. One set is based on the complete set of orthogonal modes of the magnetic cavity, and the other employs Chebyshev polynomials with the proper edge condition for disk currents. An additional term is added to the disk current expansion to properly model the current in the vicinity of the probe/disk junction. The input impedance of the stacked microstrip antenna including the probe self-impedance is calculated as a function of the layered parameters and the ratio of the two disk radii. Disk current distribution and radiation patterns are also presented. The calculated results are compared with experimental data and shown to be in good agreement.

A method for the analysis of complex frequency-dependent signal interconnections and planar circuits terminated with nonlinear load is investigated. The frequency-dependent portion of the system is first analyzed to get the scattering parameters and hence the impulse responses. Two different methods, depending on the complexity of

the system, are used to get the scattering parameters: the three-dimensional finite-difference time-domain method and an analytical procedure. The nonlinear convolution equations governing the overall system are then derived and solved numerically. The transient responses of a pair of coupled dispersive microstrip lines, a corner discontinuity, and a microstrip switching circuit are presented.

We analysed three-dimensional (3-D) multichip module (MCM) interconnects. In this technology, the vertical interconnects consist of small conductor plated via holes etched by a photo lithography system. The via dimensions are in the same order as the microstrip and stripline widths to reduce the transmission line discontinuities. Two 3-D transitions are investigated: microstrip-via-stripline and microstrip-via-90 degree stripline. The finite-difference time-domain with nonuniform grid is applied to the analysis of these transitions. Electric field distribution and pulse propagation under the strip and the strip line are presented. The scattering parameters for various cases are calculated and compared. Geometrical effects such as different conductor extensions on top of the vias and different hole sizes in the reference plane are also investigated.

A method for calculation of the current distribution, resistance, inductance matrices for a system of coupled superconducting transmission lines having finite rectangular cross section is developed.¹² These calculations allow accurate characterization of both high- T_c and low- T_c superconducting transmission lines. For a single stripline geometry with finite ground planes, the current distribution, resistance, and kinetic inductance are calculated as a function of the penetration depth for various film thicknesses. These calculations are then used to determine the penetration depth for Nb, NbN, and $\text{YBa}_2\text{Cu}_3\text{O}_{7-x}$ superconducting thin films from the measured temperature dependence of the resonant frequency of a stripline resonator. The calculations are also used to convert measured temperature dependence of the quality factor to the intrinsic surface resistance as a function of temperature for an Nb strip-line resonator.

The calculations of resistance and inductance are used for the determination of surface impedance of

¹¹ A.N. Tulintseff, S.M. Ali, and J.A. Kong, "Input Impedance of a Probe-Fed Stacked Circular Microstrip Antenna," *IEEE Trans. Antennas Propag.* 39(3): 381-390 (1991).

¹² D.M. Sheen, S.M. Ali, D.E. Oates, R.S. Withers, and J.A. Kong, "Current Distribution, Resistance, and Inductance for Superconducting Strip Transmission Lines," *IEEE Trans. Appl. Superconduct.* 1(2): 108-115 (1991); D.M. Sheen, S.M. Ali, D.E. Oates, R.S. Withers, and J.A. Kong, "Current Distribution in Superconducting Strip Transmission Lines," Proceedings of the 1991 IEEE MTT-S International Microwave Symposium, pp. 161-164, Boston, Massachusetts, June 11-14, 1991.

$\text{YBa}_2\text{Cu}_3\text{O}_{7-x}$ thin films using a stripline resonator.¹³ The surface impedance as a function of frequency from 1.5 to 20 GHz, as function of temperature from 4 K to the transition temperature (90 K), and as a function of the RF magnetic field from zero to 300 Oe, is obtained. At low temperatures the surface resistance of the films shows a very weak dependence on the magnetic field up to 225 to 250 Oe. At 77 K, the surface resistance is proportional to the square of the field. The penetration depth shows a much weaker dependence on the field than does the surface resistance.

The Ginzburg-Landau (GL) theory is used to predict the nonlinear behavior in a superconducting stripline resonator as a function of input. A method for calculating the nonlinear inductance and the fractional change in the resonant frequency of a stripline resonator is presented. By solving the GL equations inside the superconducting strip, the spatial variation of the number density of superconducting electrons, and hence the spatial variation of the magnetic penetration depth are obtained for different values of input current. First, an infinite parallel plate transmission line is considered where the one-dimensional GL equations are solved. The two-dimensional case of stripline is then considered. Nonlinear inductances are calculated as functions of input current for different superconducting strip lines. Comparisons of the calculated resonance frequency shift with measurements for $\text{YBa}_2\text{Cu}_3\text{O}_{7-x}$ stripline resonators show excellent agreement.

A full-wave numerical analysis is applied to accurately characterize superconducting transmission lines embedded in a layered media. An integral equation formulation is developed by using a spectral domain Green's function for stratified media. Galerkin's method with roof top basis functions for the electric field distribution inside the superconductor is then employed to solve for the complex propagation constant. The thickness of the superconducting film is arbitrary in this analysis, and the formulation rigorously accounts for the anisotropy of the superconducting film. The propagation characteristics of a superconducting microstrip transmission line with a thin dielectric buffer layer are investigated. A superconducting stripline configuration with an air gap is also studied.

A full-wave analysis is applied to accurately characterize normal and superconducting coplanar strip lines (CPS) and coplanar waveguides (CPW). A

volume integral equation formulation which rigorously considers the finite thickness, conductivity, and anisotropy of the strips, is developed. The phase and attenuation constants for copper CPS and CPW at 77 K and room temperatures are calculated and compared to experimental results obtained by short-pulse propagation measurements.

1.4 Remote Sensing of Earth Terrain

Sponsor

National Aeronautics and Space Administration
Grant NAGW-1617
Grant 958461

Project Staff

Professor Jin A. Kong, Dr. Robert T. Shin, Dr. Heng A. Yueh, Dr. Son V. Nghiem, Harold H. Lim, Robert G. Atkins, Hsiu C. Han, David V. Arnold, Murat E. Veysoglu, Chih-Chien Hsu, William W. Au, Joel T. Johnson, Pierre Couffu

A branching model is proposed for the remote sensing of vegetation. The frequency and angular response of a two-scale cylinder cluster are calculated to demonstrate the significance of vegetation architecture. The results indicate that it is necessary for theoretical remote sensing models to take into account the architecture of vegetation which plays an important role in determining the observed coherent effects. A two-scale branching model is implemented for soybeans with its internal structure and the resulting clustering effects considered. Furthermore, at the scale of soybean fields, the relative locations of soybean plants is described by a pair distribution function. The polarimetric backscattering coefficients are obtained in terms of the scattering properties of soybean plants and their pair distribution. Theoretical backscattering coefficients are evaluated using a hole-corrected pair distribution function. Backscattering coefficients calculated are in good agreement with extensive data collected from soybean fields. It is found that the hole-correction approximation, which prevents two soybean plants from overlaying each other, greatly improves the agreement between the model and these three data sets near normal incidence, by introducing destructive interference at small angles of incidence.

¹³ D.E. Oates, C. Anderson, D.M. Sheen, and S.M. Ali, "Stripline Resonator Measurements of $Z_0\text{VSH}_n$ in $\text{YBa}_2\text{Cu}_3\text{O}_{7-x}$ Thin Films," *IEEE Trans. Microwave Theory Tech.* 39: 1522-1529 (1991).